

Accurate solutions of elastic and acoustic waves propagation problems by the linear elements with reduced dispersion

Presented by

Duc H. Pham

A Dissertation
in Mechanical Engineering

Submitted to the Graduate Faculty of Texas Tech University
in Partial Fulfillment of the Requirements for the Degree of
Doctor of Philosophy

Dr. Alexander Idesman
(Chairperson of the Committee)

Dr. Sukalyan Bhattacharya

Dr. Siva Parameswaran

Dr. James Yang

Dr. Eugenio Aulisa

Peggy Gorden Miller
Dean of the Graduate School

December 2013

Copyright 2013
Duc H. Pham

ACKNOWLEDGMENTS

First and foremost I want to thank my advisor Dr. Alexander Idesman. It has been a pleasure to work with him. I appreciate all his contributions of time, ideas, and fundings to make my Ph.D. experience productive and possible. I am also grateful for the supports in part by the Air Force Office of Scientific Research (contract FA9550-12-1-0324) and by Texas Tech University.

Contents

ACKNOWLEDGMENTS	ii
ABSTRACT	v
LIST OF FIGURES	xvi
1 INTRODUCTION	1
2 ANALYSIS OF NUMERICAL DISPERSION	10
2.1 Analysis of numerical dispersion of elastodynamics problems in the 1-D case	16
2.2 Analysis of numerical dispersion of elastodynamics problems in the 2-D case	18
2.2.1 The modified integration rule	19
2.2.2 The averaged mass matrix	24
2.2.3 Existing approaches	24
2.3 Analysis of numerical dispersion of elastodynamics problems in the 3-D case	26
2.3.1 The modified integration rule	27
2.3.2 The averaged mass matrix	28
2.4 Analysis of numerical dispersion of acoustic wave propagation problems in the 2-D case	29
2.4.1 The modified integration rule	29
2.4.2 The averaged mass matrix	30
2.4.3 The standard approach with the lumped mass matrix	34
3 The two-stage time-integration technique with filtering spu- rious oscillations	36

3.1	Quantification of spurious oscillations and selection of amount of numerical dissipation (in terms of time increments) for their filtering	37
3.2	The implicit TCG method for the filtering stage	39
4	Numerical modeling	41
4.1	1D impact of an elastic bar against a rigid wall	41
4.2	2D impact of an elastic bar against a rigid wall	48
4.3	3D impact of an elastic bar against a rigid wall	56
4.4	2D transient acoustic problems: impact of a plate	60
5	Comparison of accuracy of different orders of high-order standard, spectral, and isogeometric elements	71
5.1	High-order standard, spectral and isogeometric elements	73
5.2	Space-discretization techniques with the non-diagonal mass matrix	76
5.3	Space-discretization techniques with the diagonal mass matrix	83
5.4	The effect of time increments in basic computations on the accuracy of different space-discretization techniques	90
6	CONCLUSIONS	98

ABSTRACT

Finite element techniques with reduced dispersion (RD) are suggested for linear acoustic and elastodynamics wave propagation problems using explicit time-integration methods. The linear elements with RD are based on the modified integration rule approach for the mass and stiffness matrices and on averaged mass matrix approach. First, the analytical study of numerical dispersion of the new techniques is applied to 1-D, 2-D and 3-D cases for elastodynamics and 2-D case acoustic wave propagation problems. The 1-D case of elastodynamics coincides to the 1-D case of acoustic wave propagation problems. In contrast to standard linear elements with explicit time-integration methods, the analytical study of the numerical dispersion shows that linear elements with RD yield more accurate results at small time increments; i.e., smaller than the stability limit, in the 2-D and 3-D cases for elastodynamics problems. For the 2-D acoustic wave propagation problems, the most accurate results can be obtained with time increments close to the stability limit.

Numerical solutions of wave propagation problems with high frequency and impact loading may lead to divergent numerical results at mesh refinement. These are explained by the appearance of large, spurious high-frequency oscillations. In order to quantify and suppress these oscillations, a two-stage time-integration technique (see [45, 47, 50]), including a stage of basic computations and a filtering stage, is applied to obtain accurate convergent results as well as significantly reduces the numerical anisotropy of solutions. Numerical results show that for elastodynamics and acoustic problems, compared with standard linear elements at the same accuracy, linear elements with RD significantly reduce the number of degrees of freedom (dof) by factors of 2 – 3 or more, 4 – 9 or more, and 8 – 27 or more in the 1-D, 2-D, and 3-D cases, respectively.

Second, we compare the accuracy of numerical solutions obtained with high-order, standard finite elements, isogeometric elements, spectral elements, and linear

elements with RD based on implicit and explicit time-integration methods. We use the 1-D impact problem with simple analytical solutions as a benchmark. The two-stage time-integration technique is applied to obtain accurate solutions for elastodynamics problems using different space-discretization methods. The comparison shows that, at the same number of dof, high-order isogeometric and spectral elements yield more accurate results than the high-order standard elements and linear elements with RD. However, linear elements with RD require less computation time for the same accuracy than other high-order elements.

We also analyze the effect of the size of time increments in the stage of basic computations on the accuracy of numerical results. With the exception of linear elements with lumped mass matrices, accurate solutions with other low- and high-orders elements require small time increments. Increments smaller than the stability limit should be used for long observation times. The time increments should also be inversely proportional to the square root of the observation times for the 2nd-order time-integration methods.

List of Figures

2.1	Adjacent quadrilateral finite elements used for the derivation of the dispersion equation for the common node in the 1-D (a), 2-D (b) and 3-D (c) cases.	16
2.2	Coefficient a_6 in Eq. (2.42) as a function of Θ and τ	31
2.3	Coefficients a_6 in Eq. (2.44) at $\tau = \tau^{st} = 0.805$ (curve 1) and in Eq. (2.42) at $\tau = \tau^{st} = 0.7587$ (curve 2) as a function of Θ	32
2.4	Coefficient a_6 in Eq. (2.44) as a function of Θ and τ	33
2.5	Coefficient a_4 in Eq. (2.45) as a function of Θ	33
2.6	Coefficient a_4 in Eq. (2.46) as a function of Θ and τ	35
4.1	Impact of an elastic bar of length $L = 4$ against a rigid wall (a). The velocity distribution along the bar at observation time $T = 18$ after basic computations with small time increments $\Delta t = \Delta t^{st}/20 = 0.002$ (b, c) and after post-processing (d, e). Curves 1 correspond to the analytical solution. Curves 2 and 3 correspond to the numerical solutions with the averaged ($\gamma = \frac{3-\tau^2}{2}$) and lumped mass matrices on a uniform mesh with 100 linear 2-node finite elements. Curves 4 correspond to the numerical solutions from the paper [47]) for the averaged mass matrix ($\gamma = 0.5$) and the implicit time-integration method on a uniform mesh with 100 linear 2-node finite elements. (c) and (e) show the zoomed graphs (b) and (d) in the range $1.6 < x < 2.4$	42
4.2	The velocity distribution along the bar at observation time $T = 18$ after basic computations with small time increments $\Delta t = \Delta t^{st}/20$ (a, b) and after post-processing (c, d). Curves 1 correspond to the analytical solution. Curves 2 correspond to the numerical solutions with the averaged ($\gamma = \frac{3-\tau^2}{2}$) mass matrix on a uniform mesh with 100 linear 2-node finite elements. Curves 3 correspond to the numerical solutions with the lumped mass matrix on a uniform mesh with 300 linear 2-node finite elements. (b) and (d) show the zoomed graphs (a) and (c) in the range $1.6 < x < 2.4$	45

- 4.3 The velocity distribution along the bar at observation time $T = 18$ after basic computations (a, b) and after post-processing (c, d). A uniform mesh with 100 linear 2-node finite elements is used. Curves 1 correspond to the analytical solution. Curves 2 and 3 correspond to the numerical solutions with the averaged ($\gamma = \frac{3-\tau^2}{2}$) and lumped mass matrices (with small time increments $\Delta t = \Delta t^{st}/20$ in basic computations). Curves 4 correspond to the numerical solutions for the averaged ($\gamma = 1.5$) mass matrix and the time increments in basic computations close to the stability limit. b) and d) show the zoomed graphs a) and c) in the range $1.6 < x < 2.4$. Curves 4 and 5 in c) and d) differ by the amount of numerical dissipation used at the filtering stage; see the text. 46
- 4.4 A 2-D plane strain impact problem (a). The axial velocity distribution along the axis of symmetry AD at observation time $T = 13$ for the Poisson's ratio $\nu = 0.3$. The results are shown after basic computations obtained by the explicit central difference method with the lumped mass matrix (b), with the modified integration rule (c), and with the averaged mass matrix (d). Curves 1 and 2 correspond to the numerical solutions obtained with the time increments Δt^{st} and $\Delta t^{st}/20$, respectively. Curves 3 correspond to the numerical solutions (from the paper [47]) obtained by the implicit time-integration method with the modified integration rule (c) and the averaged mass matrix (d). A uniform mesh with $40 \times 160 = 6400$ linear 4-node finite elements is used. 48
- 4.5 The axial velocity distribution v_x along the axis of symmetry AD (a, b) and the transverse velocity distribution v_y along the external surface BC (c, d) at observation time $T = 13$ for the Poisson's ratio $\nu = 0.3$. The results are shown after the filtering of the solutions at basic computations obtained by the explicit central difference method with the lumped mass matrix (curves 1 and 2), with the modified integration rule (curve 3), and with the averaged mass matrix (curve 4). Small time increments $\Delta t^{st}/20$ are used at basic computations (see Fig. 4.4). Uniform meshes with $40 \times 160 = 6400$ (curves 1, 3 and 4) and $120 \times 480 = 57600$ (curve 2) linear elements are used. b) and d) show the zoomed graphs a) and c) in the range $0.4 < x < 1.4$ 51

- 4.6 The axial velocity distribution v_x along the axis of symmetry AD (a, c) and the transverse velocity distribution v_y along the external surface BC (b, d) at observation time $T = 13$ for the Poisson's ratio $\nu = 0.3$. The results are shown after the filtering of the solutions at basic computations obtained by the explicit central difference method with the modified integration rule (a, b) and with the standard approach (curves 1-3 in (c, d)). Small time increments $\Delta t^{st}/20$ are used at basic computations. Curves 1, 2, 3, 4 correspond to uniform meshes with $20 \times 80 = 1600$, $40 \times 160 = 6400$, $80 \times 320 = 25600$, and $320 \times 1280 = 409600$ linear elements. Curves 4 in (a, b, c, d) correspond to the modified integration rule and are considered as a reference solution. 52
- 4.7 The error in velocity e versus the number of dof for standard approach (curve 1), for the modified integration rule technique (curve 2) and for the averaged mass matrix technique (curve 3). The logarithmic scale is used. Curve 2 and 3 practically coincide. 54
- 4.8 The axial velocity distribution along the axis of symmetry AD at observation time $T = 13$ for the Poisson's ratios $\nu = 0.1$ (a, b), $\nu = 0.3$ (c, d) and $\nu = 0.49$ (e, f). The results are shown after the filtering of the solutions at basic computations obtained by the explicit central difference method with the averaged mass matrix and the following time increments: Δt^{st} (curves 2), $0.5\Delta t^{st}$ (curves 3) and $\Delta t^{st}/20$ (curves 4). A uniform mesh with $40 \times 160 = 6400$ linear 4-node finite elements is used. Curves 1 are the reference solutions (from the paper [47]) obtained by the implicit time-integration method with the averaged mass matrix on a fine mesh with $300 \times 1200 = 360000$ linear finite element. b), d) and f) show the zoomed graph a), c) and e), respectively. 55
- 4.9 The axial velocity distribution along the axis of symmetry AD at observation time $T = 13$ for the Poisson's ratios $\nu = 0.1$ (a, b), $\nu = 0.3$ (c, d) and $\nu = 0.49$ (e, f). The results are shown after the filtering of the solutions at basic computations obtained by the explicit central difference method with the modified integration rule and the following time increments: Δt^{st} (curves 2), $0.5\Delta t^{st}$ (curves 3) and $\Delta t^{st}/20$ (curves 4). A uniform mesh with $40 \times 160 = 6400$ linear 4-node finite elements is used. Curves 1 are the reference solutions (from the paper [47]) obtained by the implicit time-integration method with the modified integration rule on a fine mesh with $300 \times 1200 = 360000$ linear finite element. b), d), and f) show the zoomed graph a), c), and e), respectively. 56
- 4.10 Impact of an elastic 3-D square bar of length $L = 2$ and width $a = 2$ against a rigid wall (a). A uniform mesh with $20 \times 20 \times 40 = 16000$ linear $Q8$ finite elements (b). 57

4.16 The velocity distribution along AD (curves 1) and along AC (curves 2) at the observation time $T = 0.8$ after basic computations (a) and after the filtering stage (b); see Fig. 4.15a for AD and AC . A uniform mesh with $100 \times 100 = 10000$ linear four-node quadrilateral finite elements and the reduced-dispersion technique with $\gamma = \frac{3-\tau^2}{2}$ and $\alpha_K = \sqrt{\frac{2}{3}}$ are used.	64
4.17 The velocity distribution along AD at the observation time $T = 0.8$ after basic computations (a,b,c) and after the filtering stage (d). Curves 1, 2 and 3 correspond to the uniform meshes with $100 \times 100 = 10000$, $300 \times 300 = 90000$, and $800 \times 800 = 640000$ linear four-node quadrilateral finite elements and the use of the reduced-dispersion technique with $\gamma = \frac{3-\tau^2}{2}$ and $\alpha_K = \sqrt{\frac{2}{3}}$	65
4.18 The velocity distribution along AD (curves 1) and along AC (curves 2) at the observation time $T = 0.8$ after basic computations (a) and after the filtering stage (b,c); see the text for explanations. A uniform mesh with $100 \times 100 = 10000$ linear four-node quadrilateral finite elements, the standard approach with the lumped mass matrix and the time increments equal to the stability limit in basic computations are used. The range of frequencies filtered in (b) is the same as that in Fig. 4.16b for the reduced dispersion technique. Curve 3 in (c) corresponds to curve 1 in Fig. 4.16b.	66
4.19 The 2-D impact of a plate (a). The distribution of the velocity $v(x, y, 1.5)$ in the plate at the observation time $T = 0.1.5$ after basic computations (b) and after the filtering stage (c). A uniform mesh with $100 \times 100 = 10000$ linear Q4 finite elements with reduced-dispersion is used.	68
4.20 The velocity distribution along AB at the observation time $T = 1.5$ after basic computations (a-c) and after the filtering stage (d). Curves 1,2,3,4,5 and 6 correspond to the numerical results obtained on uniform meshes with $100 \times 100 = 10000$ Q4 (reduced dispersion), $100 \times 100 = 10000$ Q4 (standard), $50 \times 50 = 2500$ Q9 (standard), $300 \times 300 = 90000$ Q4 (standard), $66 \times 66 = 4356$ Q9 (standard), and $300 \times 300 = 90000$ Q4 (reduced dispersion) finite elements, respectively.	69
5.1 The velocity distribution along the bar after (a, b) basic computations (the consistent mass matrix and small time increments) and after (c, d) post-processing. A uniform mesh with the standard linear elements and 101 dof is used. Curves 1 correspond to the analytical solutions. Curves 2, 3, 4 and 5 correspond to the observation times $T = 2, 18, 98$ and 194 , respectively. b) and d) show the zoomed graphs a) and c) in the range $1.6 < x < 2.4$	79

5.2 The velocity distribution along the bar after (a, b) basic computations (the consistent mass matrix and small time increments) and after (c, d) post-processing. A uniform mesh with the standard quadratic elements and 101 dof is used. Curves 1 correspond to the analytical solutions. Curves 2, 3, 4 and 5 correspond to the observation times $T = 2, 18, 98$ and 194, respectively. b) and d) show the zoomed graphs a) and c) in the range $1.6 < x < 2.4$	79
5.3 The velocity distribution along the bar after (a, b) basic computations (the consistent mass matrix and small time increments) and after (c, d) post-processing. A uniform mesh with the standard 3rd-order elements and 100 dof is used. Curves 1 correspond to the analytical solutions. Curves 2, 3, 4 and 5 correspond to the observation times $T = 2, 18, 98$ and 194, respectively. b) and d) show the zoomed graphs a) and c) in the range $1.6 < x < 2.4$	80
5.4 The velocity distribution along the bar after (a, b) basic computations (the consistent mass matrix and small time increments) and after (c, d) post-processing. A uniform mesh with the standard 5th-order elements and 101 dof is used. Curves 1 correspond to the analytical solutions. Curves 2, 3, 4 and 5 correspond to the observation times $T = 2, 18, 98$ and 194, respectively. b) and d) show the zoomed graphs a) and c) in the range $1.6 < x < 2.4$	80
5.5 The velocity distribution along the bar after (a, b) basic computations (the consistent mass matrix and small time increments) and after (c, d) post-processing. A uniform mesh with the isogeometric quadratic elements and 101 dof is used. Curves 1 correspond to the analytical solutions. Curves 2, 3, 4 and 5 correspond to the observation times $T = 2, 18, 98$ and 194, respectively. b) and d) show the zoomed graphs a) and c) in the range $1.6 < x < 2.4$	81
5.6 The velocity distribution along the bar after (a, b) basic computations (the consistent mass matrix and small time increments) and after (c, d) post-processing. A uniform mesh with the isogeometric 3rd-order elements and 101 dof is used. Curves 1 correspond to the analytical solutions. Curves 2, 3, 4 and 5 correspond to the observation times $T = 2, 18, 98$ and 194, respectively. b) and d) show the zoomed graphs a) and c) in the range $1.6 < x < 2.4$	81
5.7 The velocity distribution along the bar after (a, b) basic computations (the non-diagonal mass matrix and small time increments) and after (c, d) post-processing. A uniform mesh with the linear elements with reduced dispersion and 101 dof is used. Curves 1 correspond to the analytical solutions. Curves 2, 3, 4 and 5 correspond to the observation times $T = 2, 18, 98$ and 194, respectively. b) and d) show the zoomed graphs a) and c) in the range $1.6 < x < 2.4$	82

5.8 The velocity distribution along the bar at the observation time $T = 18$ after post-processing. We compare the curves from Fig. 5.1, 5.2, 5.3, 5.4, 5.6 and 5.7. Curves 1 correspond to the analytical solutions. Curves 2 in (a, b), 3 in (a, b), 4 and 5 correspond to the standard linear, quadratic, 3rd-order (100 dof) and 5th-order elements with 101 dof. Curves 2 in (c, d) and 3 in (c, d) correspond to the linear elements with reduced dispersion (the non-diagonal mass matrix) with 101 and 201 dof, respectively. Curves 6 correspond to the isogeometric 3rd-order elements with 101 dof. b) and d) show the zoomed graphs a) and c) in the range $1.8 < x < 2.2$	82
5.9 The velocity distribution along the bar in the range $1.8 < x < 2.2$ at the observation times $T = 18$ (a) and $T = 194$ (b) after post-processing. We compare the curves from Fig. 5.5 - 5.7. Curves 1 correspond to the analytical solutions. Curves 2, 3 and 4 correspond to the linear elements with reduced dispersion (the non-diagonal mass matrix) with 101, 201 and 251 dof, respectively. Curves 5 and 6 correspond to the isogeometric quadratic and 3rd-order elements with 101 dof.	83
5.10 The velocity distribution along the bar after (a, b) basic computations (the lumped mass matrix and small time increments) and after (c, d) post-processing. A uniform mesh with the standard (spectral) linear elements and 101 dof is used. Curves 1 correspond to the analytical solutions. Curves 2, 3, 4 and 5 correspond to the observation times $T = 2, 18, 98$ and 194 , respectively. b) and d) show the zoomed graphs a) and c) in the range $1.6 < x < 2.4$	87
5.11 The velocity distribution along the bar after (a, b) basic computations (the lumped mass matrix and small time increments) and after (c, d) post-processing. A uniform mesh with the standard (spectral) quadratic elements and 101 dof is used. Curves 1 correspond to the analytical solutions. Curves 2, 3, 4 and 5 correspond to the observation times $T = 2, 18, 98$ and 194 , respectively. b) and d) show the zoomed graphs a) and c) in the range $1.6 < x < 2.4$	87
5.12 The velocity distribution along the bar after (a, b) basic computations (the lumped mass matrix and small time increments) and after (c, d) post-processing. A uniform mesh with the spectral 3rd-order elements and 100 dof is used. Curves 1 correspond to the analytical solutions. Curves 2, 3, 4 and 5 correspond to the observation times $T = 2, 18, 98$ and 194 , respectively. b) and d) show the zoomed graphs a) and c) in the range $1.6 < x < 2.4$	88

5.13 The velocity distribution along the bar after (a, b) basic computations (the lumped mass matrix and small time increments) and after (c, d) post-processing. A uniform mesh with the spectral 5th-order elements and 101 dof is used. Curves 1 correspond to the analytical solutions. Curves 2, 3, 4 and 5 correspond to the observation times $T = 2, 18, 98$ and 194, respectively. b) and d) show the zoomed graphs a) and c) in the range $1.8 < x < 2.2$	88
5.14 The velocity distribution along the bar after (a, b) basic computations (the lumped mass matrix and small time increments) and after (c, d) post-processing. A uniform mesh with the spectral 10th-order elements and 101 dof is used. Curves 1 correspond to the analytical solutions. Curves 2, 3, 4 and 5 correspond to the observation times $T = 2, 18, 98$ and 194, respectively. b) and d) show the zoomed graphs a) and c) in the range $1.8 < x < 2.2$	89
5.15 The velocity distribution along the bar after (a, b) basic computations (the lumped mass matrix and small time increments) and after (c, d) post-processing. A uniform mesh with the linear elements with reduced dispersion and 101 dof is used. Curves 1 correspond to the analytical solutions. Curves 2, 3, 4 and 5 correspond to the observation times $T = 2, 18, 98$ and 194, respectively. b) and d) show the zoomed graphs a) and c) in the range $1.6 < x < 2.4$	89
5.16 The velocity distribution along the bar in the range $1.8 < x < 2.2$ at the observation times $T = 18$ (a, c) and $T = 194$ (b, d) after post-processing. We compare the curves from Fig. 5.6, 5.10, 5.11, 5.13, 5.14 and 5.15. Curves 1 correspond to the analytical solutions. Curves 2 in (a, b), 2 in (c, d), 3 in (c, d) and 4 in (c, d) correspond to the linear elements with reduced dispersion (the lumped mass matrix) with 101, 201, 301 and 401 dof, respectively. Curves 3 in (a, b), 4 in (a, b), 5 in (a, b), 6 and 7 correspond to the spectral linear, quadratic, 4th-order, 5th-order and 10th-order elements with 101 dof. Curves 5 in (c, d) correspond to the isogeometric 3rd-order elements with 101 dof.	90
5.17 The velocity distribution along the bar at the observation time $T = 2$ after (a, b) basic computations (the consistent mass matrix and small time increments) and after (c, d) post-processing. A uniform mesh with the isogeometric 3rd-order elements and 101 dof is used. Curves 2, 3, 4 and 5 correspond to the following time increments in basic computations: $d\bar{t}$, $0.5d\bar{t}$, $0.2d\bar{t}$ and $0.1d\bar{t}$, respectively ($d\bar{t}=0.04$). b) and d) show the zoomed graphs a) and c) in the range $1.8 < x < 2.2$	93

- 5.18 The velocity distribution along the bar at the observation time $T = 18$ after (a, b) basic computations (the consistent mass matrix and small time increments) and after (c, d) post-processing. A uniform mesh with the isogeometric 3rd-order elements and 101 dof are used. Curves 2, 3, 4, 5 and 6 correspond to the following time increments in basic computations: $d\bar{t}$, $0.5d\bar{t}$, $0.2d\bar{t}$, $0.1d\bar{t}$ and $0.01d\bar{t}$, respectively ($d\bar{t}=0.04$). b) and d) show the zoomed graphs a) and c) in the range $1.8 < x < 2.2$ 94
- 5.19 The velocity distribution along the bar at the observation time $T = 194$ after (a, b) basic computations (the consistent mass matrix and small time increments) and after (c, d) post-processing. A uniform mesh with the isogeometric 3rd-order elements and 101 dof are used. Curves 2, 3, 4, 5 and 6 correspond to the following time increments in basic computations: $d\bar{t}$, $0.2d\bar{t}$, $0.1d\bar{t}$, $0.03d\bar{t}$ and $0.01d\bar{t}$, respectively ($d\bar{t}=0.04$). b) and d) show the zoomed graphs a) and c) in the range $1.8 < x < 2.2$ 94
- 5.20 The velocity distribution along the bar at the observation time $T = 2$ after (a, b) basic computations (the lumped mass matrix and small time increments) and after (c, d) post-processing. A uniform mesh with the spectral 3rd-order elements and 100 dof is used. Curves 2, 3 and 4 correspond to the following time increments in basic computations: $0.95dt^{st}$, $0.5dt^{st}$ and $0.1dt^{st}$, respectively ($dt^{st}=0.02817$). b) and d) show the zoomed graphs a) and c) in the range $1.8 < x < 2.2$ 95
- 5.21 The velocity distribution along the bar at the observation time $T = 18$ after (a, b) basic computations (the lumped mass matrix and small time increments) and after (c, d) post-processing. A uniform mesh with the spectral 3rd-order elements and 100 dof is used. Curves 2, 3, 4 and 5 correspond to the following time increments in basic computations: $0.95dt^{st}$, $0.5dt^{st}$, $0.3dt^{st}$ and $0.1dt^{st}$, respectively ($dt^{st}=0.02817$). b) and d) show the zoomed graphs a) and c) in the range $1.8 < x < 2.2$ 95
- 5.22 The velocity distribution along the bar at the observation time $T = 194$ after (a, b) basic computations (the lumped mass matrix and small time increments) and after (c, d) post-processing. A uniform mesh with the spectral 3rd-order elements and 100 dof is used. Curves 2, 3, 4, 5 and 6 correspond to the following time increments in basic computations: $0.95dt^{st}$, $0.5dt^{st}$, $0.3dt^{st}$, $0.1dt^{st}$ and $0.01dt^{st}$, respectively ($dt^{st}=0.02817$). b) and d) show the zoomed graphs a) and c) in the range $1.8 < x < 2.2$ 96

5.23 The velocity distribution along the bar at the observation time $T = 2$ after (a, b) basic computations (the lumped mass matrix and small time increments) and after (c, d) post-processing. A uniform mesh with the spectral 10th-order elements and 100 dof is used. Curves 2, 3 and 4 correspond to the following time increments in basic computations: $0.95dt^{st}$, $0.7dt^{st}$ and $0.1dt^{st}$, respectively ($dt^{st}=0.0113$). b) show the zoomed graphs a) in the range $1.8 < x < 2.2$. d) show the zoomed graphs c) in the range $1.8 < x < 2.2$	96
5.24 The velocity distribution along the bar at the observation time $T = 18$ after (a, b) basic computations (the lumped mass matrix and small time increments) and after (c, d) post-processing. A uniform mesh with the spectral 10th-order elements and 101 dof is used. Curves 2, 3, 4 and 5 correspond to the following time increments in basic computations: $0.95dt^{st}$, $0.7dt^{st}$, $0.5dt^{st}$ and $0.1dt^{st}$, respectively ($dt^{st}=0.0113$). b) and d) show the zoomed graphs a) and c) in the range $1.8 < x < 2.2$. . .	97
5.25 The velocity distribution along the bar at the observation time $T = 194$ after (a, b) basic computations (the lumped mass matrix and small time increments) and after (c, d) post-processing. A uniform mesh with the spectral 10th-order elements and 101 dof is used. Curves 2, 3, 4, 5 and 6 correspond to the following time increments in basic computations: $0.95dt^{st}$, $0.5dt^{st}$, $0.3dt^{st}$, $0.1dt^{st}$, and $0.01dt^{st}$, respectively ($dt^{st}=0.0113$). b) and d) show the zoomed graphs a) and c) in the range $1.8 < x < 2.2$	97

Chapter I

INTRODUCTION

Many people in the engineering community believe that the field of elastodynamics and finite element analysis for wave propagation phenomena are sufficiently mature and need only insignificant improvements. However, anyone who tries to solve these problems, even in the simplest case of linear elastic materials, will find that there is no reliable numerical technique that can yield an accurate solution because of spurious oscillations. Moreover, the amplitude of spurious oscillations in numerical solutions may increase at mesh refinement and at very small time increments. As a consequence, the problem cannot be solved and its numerical result cannot be trusted. According to Robert Cook, author of the popular textbook, *Concepts and Applications of Finite Element Analysis*, “In no way can today’s computer programs for wave propagation and impacted [problems] be treated as ‘black boxes.’ A minimum 6 months to 2 years of experience is needed to be able to use such programs successfully.”

It may be unusual to a person without experience in solving these problems to believe that existing methods fail to produce accurate results because of the appearance of spurious oscillations. For transient acoustic and elastodynamics problems, the existing numerical approaches in space-discretization methods, such as the finite element method, spectral element method, isogeometric analysis, among others, do not include techniques that separate spurious and actual oscillations in the numerical results. My research focuses on developing and implementing new finite element techniques with reduced dispersion (RD) error based on explicit time-integration methods for transient linear elastodynamics and acoustic problems under impact loading.

In my research, I consider elastodynamics and acoustic wave propagation problems with impact loading in a finite isotropic and homogeneous medium. For elastodynamics problems subject to Dirichlet conditions on boundary and initial data, I

consider the following strain-displacement relations:

$$\varepsilon_{ij} = \frac{1}{2} \left(\frac{\partial u_i}{\partial x_j} + \frac{\partial u_j}{\partial x_i} \right), \quad (1.1)$$

elastic constitutive law (Hooke's law):

$$\sigma_{ij} = \lambda \varepsilon_{kk} \delta_{ij} + 2\mu \varepsilon_{ij}, \quad (1.2)$$

equation of motion:

$$\frac{\partial \sigma_{ij}}{\partial x_j} + f_i = \rho \frac{\partial^2 u_i}{\partial t^2}, \quad (1.3)$$

where ε_{ij} , σ_{ij} , δ_{ij} , u_i , f_i , $i, j = 1 \dots 3$ respectively represent the strain tensor, stress tensor, identity matrix, displacement component, and body force component. The constants λ , μ , ρ are Lame's constant, the shear modulus, and the density.

For the initial value acoustic wave propagation problems with Dirichlet and Neumann boundary conditions, the following scalar wave equation is considered:

$$c_o^2 \nabla^2 u + f = \frac{\partial^2 u}{\partial t^2}, \quad (1.4)$$

where u , c_0 and f are respectively the field variable, wave velocity, and body force. Discretization of (1.3), (1.4) in space give the following ordinary differential equations in time

$$\mathbf{M} \ddot{\mathbf{U}} + \mathbf{K} \mathbf{U} = \mathbf{F}, \quad (1.5)$$

where \mathbf{M} and \mathbf{K} are the mass and stiffness matrices, respectively; $\mathbf{U}(t)$, $\mathbf{F}(t)$ are the vector of the nodal field variable and nodal load. Equation (1.5) can also be obtained by the application of other space-discretization methods, such as the spectral elements method (e.g., see [14, 55, 56, 57, 81] and others), the isogeometric analysis (e.g., see [10, 11, 21, 38] and others), the boundary element method (e.g., see [91]), the smoothed finite elements method (e.g., see [67, 68]), and different meshless methods (e.g., see [22, 61, 62, 63, 66, 69]). Many different numerical methods have been

developed for the time-integration of (1.5). However, for wave propagation problems, there is no reliable time-integration method.

Due to the space-discretization, the exact time-integration of (1.5) leads to the appearance of spurious high-frequency oscillations or dispersion error (e.g., see [16, 23, 29, 32, 58, 74, 88, 95, 99]). Current approaches of treating spurious oscillations introduce numerical dissipation or artificial viscosity from the first time increment. However, for known time-integration methods with numerical dissipation (e.g., the Houbolt, the Newmark, the HHT- α , the TDG, and others), there is no understanding of how to select a time increment. If time increments are very small for these methods, then numerical solutions converge to the solution of a semi-discrete problem (1.5), and contain large spurious oscillations. If time increments are large, then numerical solutions can be very inaccurate due to the error accumulation related to numerical dissipation. Moreover, numerical dissipation could also affect the accuracy of low modes in numerical solutions.

In addition, existing numerical methods with numerical dissipation do not consider the effect of the number of time increments on the accuracy of final results. Therefore, different researchers report different values of numerical dissipation that are needed to suppress spurious oscillations (see [96] and its references). However, the optimal value of numerical dissipation is not very clear, nor is the means of selecting it. Furthermore, there is also a lack of understanding of how this value depends on the number of time increments (or the observation time), the type of space-discretization methods, the order of elements, and others. Moreover, even if spurious oscillations are suppressed for a specific number of time increments (or observation time), the solution will be inaccurate for other observation times. *This contradiction between the accuracy of low modes and the suppression of spurious oscillations cannot be resolved within existing numerical methods, especially for long-term integration with a large number of time increments.*

Next, we will briefly review existing time-integration methods for elastodynamics and acoustic wave problems. Second-order accurate methods such as the Houbolt,

the Newmark, the Wilson- θ , and the HHT- α methods are most frequently used for the integration of (1.5). Zienkiewich, et al. (see [97, 98]), applying the weighted residual method to the equation of motion, developed and analyzed a set of algorithms called the unified set of a single-step method. However, the high-order, accurate method suggested in [97, 98] is not unconditionally stable for elastodynamics. Recently, new high-order accurate space-time finite elements have been developed. One group of space-time finite element formulations is derived according to Hamilton’s principle for dynamics and uses continuous weighting functions in time [2, 3, 12, 31, 78]. Several numerical techniques for elastodynamics problems based on variational formulations with continuous functions with respect to time are proposed in [4, 5, 6, 7, 8, 15]. In practice, methods of this type require more storage and computer time than existing techniques.

Another group of space-time finite element formulations for elastodynamics is based upon time-discontinuous Galerkin (TDG) methods (see [18, 37, 39, 40, 41, 59, 64, 65, 87, 89] and others). The known TDG methods do not have parameters that control high frequency behavior and lead to a spurious high-frequency response for wave propagation problems [17, 41, 71, 87], especially with non-uniform meshes (see [45, 46]). The analysis of numerical methods for elastodynamics problems based on different variational formulations is presented in [13]. Some of these formulations are close to the TDG methods. New high-order accurate methods for elastodynamics are also suggested in [28, 72]), and are based on the collocation method and the modified Nørsett method. A new unified set of time-continuous/discontinuous high-order methods is also suggested in [53, 54].

New isogeometric elements with continuous derivatives across elements are suggested in [10, 11, 38] for dynamics problems. The numerical implementation of these elements is more difficult than that of the standard finite elements and it is difficult to quantitatively estimate their advantage for elastodynamics problems from the numerical examples presented in [10].

Recently, new explicit finite element methods with unstructured meshes based

on the TDG method have been suggested for elastodynamics problems [25, 26, 94]. These technique require a special mesh (e.g., obtained by the use of the Tent Pitcher algorithm [1]) and is not easily implemented, even for a 1-D case. Another explicit method, developed in [60], is based on Hamilton’s variational principle and is implemented with piecewise linear displacement and piecewise constant velocity approximations in time. This method includes a subcycling procedure and allows different time increments for different spatial finite elements. Special subcycling integration procedures including implicit methods were also developed in [75, 84, 85, 92]. Interesting numerical schemes such as WENO and RKDG methods have been proposed for a class of hyperbolic systems, see [93] and others. However, these schemes do not include (1.5) and are not appropriate for the class of problems under consideration.

Another issue is the large computation time for real-world elastodynamics problems. Thanks to new powerful parallel computers, great progress has been made in the development and implementation of numerical algorithms on parallel computers (see [27, 51, 52, 86]), with an essential reduction in computation time for elastodynamics problems. Special techniques have also been developed for the reduction in the numerical dispersion error, which is related to “the pollution effect” (e.g., see [15-17] and others for the study of the pollution error). One simple and effective technique for elastic and acoustic wave propagation problems is based on the calculation of the mass matrix \mathbf{M} in (1.5) as a weighted average of the consistent and lumped mass matrices (see [5-8] and others).

For the 1-D case and linear finite elements, this approach reduces the error in the wave velocity for the harmonic wave from the second order to the fourth order of accuracy. However, for harmonic wave propagation in the 2-D and 3-D cases, these results are not valid (see [43]). Nevertheless, in a multidimensional case, the averaged mass matrix yields more accurate results compared with the standard mass matrix; e.g., see the numerical results in [43]. We should also mention that publications on the techniques with averaged mass matrix do not include the effect of finite time increments on the dispersion error and on the accuracy of the numerical results. We

will show that if we use the weighting coefficients for the averaged mass matrix that are independent of time increments, and if the time increments for explicit time-integration methods are close to the stability limit, then there is no advantages in the use of the averaged mass matrix compared with the lumped mass matrix.

In this paper, implicit and explicit time-integration methods are suggested for acoustic wave propagation in the the case of 2-D [95] and are based on the modified integration rule for the calculation of the mass and stiffness matrices for linear finite elements. In contrast to the averaged mass matrix, the use of the modified integration rule increases the accuracy for the phase velocity from the second order to the fourth order in the general multidimensional case of acoustic wave propagation. However, the applicability of this technique to elastodynamics problems has not been studied. The technique in [95] did not treated spurious oscillations that may significantly destroy the accuracy of numerical results. We should mention that the analysis of numerical dispersion estimates the numerical error for the propagation of harmonic wave. In the general case of loading (boundary conditions), the estimation of the accuracy of numerical techniques with reduced dispersion is difficult because of the presence of spurious high-frequency oscillations in numerical solutions (e.g., see [29, 58]).

In contrast to the existing technique, a new numerical technique has been recently suggested by Dr. Idesman to obtain non-oscillatory, accurate, and reliable solutions for elastodynamics problems (see [43]). This technique involves implicit or explicit time-integration methods with zero numerical dissipation for the integration of (1.5) as a stage of basic computations and an implicit method to filter spurious oscillations as the filtering stage. In order to exclude the error in time, we will select very small time increments at which the numerical solutions are practically independent of the size of time increments and close to the exact solution of (1.5). However, the error in space still exists due to the space-discretization of (1.5). As mentioned earlier, one of the main issues is the presence of spurious high-frequency oscillations in numerical solutions for transient elastodynamics and acoustic problems, which makes the comparison of accuracy of different numerical results difficult. We will resolve

this issue by the application of the two-stage time-integration approach developed in the papers [45, 47, 50]. Because the errors in high-frequencies do not affect the accuracy of low-frequencies, there is no need to filter spurious oscillations at each time increment. In addition, because the filtering stage is independent of the boundary and initial conditions and can be applied to any loading, it can be used as a pre- or post-processor.

One of the disadvantages of the use of implicit time-integration methods is the need to solve a system of algebraic equations that could require large computational resources for a large number of dof. Explicit time-integration methods yield an additional reduction in the computation time compared with implicit time-integration methods. Therefore, we would like to study the accurate solution of elastodynamics and acoustic wave propagation problems using linear elements with RD based on explicit time-integration methods. We will consider two techniques: a modified integration rule approach for the mass and stiffness matrices and the averaged mass matrix approach.

Furthermore, we are interested in studying the computational effectiveness of the linear elements with reduced dispersion compared with different orders of standard, spectral, and isogeometric elements. The analytical study of the numerical dispersion error is usually applied in the literature to compare different space-discretization techniques (e.g., see [16, 23, 29, 30, 58, 73, 74, 82, 83, 95, 99] and many others). We should mention that the analytical study of the dispersion error is difficult for high-order space-discretization methods. Moreover, we would like to compare the accuracy of different space-discretization techniques applied to the elastodynamics benchmark problems in which a wide range of frequencies is simultaneously excited. Because there is a very limited number of such problems with known analytical solutions, we will use the 1-D impact problem to compare the accuracy of different space-discretization techniques based on low- and high-order of standard finite elements (see [9, 36, 97]), linear finite elements with reduced dispersion (see [50, 58, 73, 74, 95]), spectral elements, and isogeometric elements. The 1-D impact

problem has the following important features: (a) all low and high frequencies of the semi-discrete system, (1.5), are excited and b) a step function is a simple analytical solution. Using this 1-D impact problem, the comparison of accuracy of the numerical solutions from different space-discretization methods could be studied when the spurious oscillations are removed.

In the first part of our study, we will analyze the numerical dispersion of the linear elements with reduced dispersion based on the explicit time-integration methods for 1-D, 2-D, and 3-D elastodynamics, and 2-D acoustic wave problems. This consists of a modification of the system of semi-discrete equations, (1.5), that can be used with explicit time-integration methods and the finite elements with reduced dispersion (Chapter II); the analysis of the numerical dispersion of elastodynamics problems for the 1-D (Section 2.1), 2-D (Section 2.2), and 3-D (Section 2.3) cases; and the analysis of the numerical dispersion of acoustic wave propagation problems for the 2-D cases (Section 2.4). We should mention that the 1-D case of the elastodynamics is equivalent to the 1-D cases of the acoustic wave problem. Next, a short description of the two-stage time-integration technique with the filtering stage will be presented in Chapter III (also see [43, 45, 50, 44, 47, 42]). The numerical examples in Chapter IV show the effectiveness of the linear elements with reduced dispersion. Moreover, the two-stage time-integration technique is used to compare the accuracy of different space-discretization methods.

In the second part of the study, we briefly introduce the standard, spectral, and the isogeometric high-order elements in Section 5.1. We compare the accuracy of different space-discretization techniques with the non-diagonal and diagonal mass matrices using the solution of the 1-D impact problem in Sections 5.2 and 5.3, respectively. These techniques are based on the implicit and explicit time-integration methods with very small time increments in basic computations. We also show that the size of time increments used at the filtering stage could be used as a quantitative comparison of the accuracy of different space-discretization techniques. In Section 5.4, the effect of the size of time increments in basic computations will be studied on

the accuracy of numerical solutions obtained with the filtering stage.

Chapter II

ANALYSIS OF NUMERICAL DISPERSION

In this section we will develop the averaged mass matrix technique and the modified integration rule technique that are used with explicit time-integration methods. These techniques significantly reduce the numerical dispersion error and the computation time compared with the standard finite element formulations for linear elastodynamics and acoustic waves problems. These results are reported in the paper [49]. In contrast to the study of the averaged mass matrix technique and the modified integration rule technique for the scalar wave equation (as considered in [58, 95]), the analytical study of these techniques for elastodynamics and acoustic problems is much more complicated due to a greater number of non-linear terms in the dispersion equation and the presence of two different types of waves (compressional and shear waves). Similar to the paper [58], we will first modify (1.5) for the use explicit time-integration methods. Let's rewrite (1.5) with the diagonal (lumped) mass matrix \mathbf{D} as follows

$$\mathbf{D} \dot{\mathbf{V}} + \mathbf{K} \mathbf{U} = \mathbf{F}, \quad (2.1)$$

where \mathbf{V} is the vector of nodal velocity. Relationships between the nodal displacements and velocities can be written down as (similar to those in [58, 95])

$$\mathbf{D} \dot{\mathbf{U}} = \mathbf{M} \mathbf{V} \quad \text{or} \quad \mathbf{D} \ddot{\mathbf{U}} = \mathbf{M} \dot{\mathbf{V}} \quad (2.2)$$

where \mathbf{M} is the non-diagonal mass matrix calculated by the averaged mass matrix technique (see (2.8) below) or by the modified integration rule technique (see (2.9)), (2.11), (2.13), (2.15) for elastodynamics and acoustic problems below). Inserting (2.2) into (2.1) we will get

$$\mathbf{D} \ddot{\mathbf{U}} + \mathbf{M} \mathbf{D}^{-1} \mathbf{K} \mathbf{U} = \mathbf{M} \mathbf{D}^{-1} \mathbf{F}. \quad (2.3)$$

Eq. (2.3) differs from the standard finite element equations with the lumped mass matrix by the stiffness matrix and the load vector which are multiplied by the term $\mathbf{M} \mathbf{D}^{-1}$. For the time integration of (2.3) we will use the standard explicit central-difference method (the most popular explicit method); e.g., see [47, 36, 9]. Replacing the second time derivative in (2.3) by the corresponding finite difference approximation used in the central-difference method, we obtain

$$\mathbf{D} [\mathbf{U}(t + \Delta t) - 2\mathbf{U}(t) + \mathbf{U}(t - \Delta t)]/\Delta t^2 + \mathbf{M} \mathbf{D}^{-1} \mathbf{K} \mathbf{U}(t) = \mathbf{M} \mathbf{D}^{-1} \mathbf{F}(t), \quad (2.4)$$

where Δt is the time increment. We will use (2.4) for the analysis of the numerical dispersion of the finite element formulations with the averaged mass matrix and modified integration rule techniques. One of the main difficulties in the analytical study of numerical dispersion is the complicated non-linear structure of the equations for numerical phase velocities. Therefore, in order to simplify the dispersion analysis, we will study the residual of these equations instead of the direct calculation of numerical phase velocities. The displacement of harmonic plane waves u_j in an infinite medium for elastodynamics with

$$u_j(\mathbf{x}, t) = \bar{u}_j \exp(i k(\mathbf{n} \cdot \mathbf{x} \pm c_o t)) \quad (2.5)$$

is used for the dispersion analysis. Here, u_j are the displacement components, \bar{u}_j are the components of the displacement amplitude vector, \mathbf{x} is the position vector, k is the wave number, \mathbf{n} is the unit normal to the wave front ($\mathbf{k} = k \mathbf{n}$ is the wave vector), c_o is the phase velocity, t is time, $i = \sqrt{-1}$. For elastodynamics problems, it is known that the substitution of (2.5) into a system of partial differential equations for an isotropic finite homogeneous elastic medium yields the following two solutions for the phase velocity [77]:

$$c_o = c_1 = \sqrt{\frac{\lambda + 2\mu}{\rho}} \quad \text{and} \quad c_o = c_2 = \sqrt{\frac{\mu}{\rho}}, \quad (2.6)$$

where c_1 and c_2 correspond to the phase velocity for the compressional and shear waves, respectively; ρ is the density; $\lambda = \frac{E\nu}{(1+\nu)(1-2\nu)}$ and $\mu = \frac{E}{2(1+\nu)}$ are the Lame coefficients that can be also expressed in terms of Young's modulus E and Poisson's ratio ν . The derivation of (2.6) does not include initial and boundary conditions. The phase velocities c_1 and c_2 are constant and independent of the wave vector \mathbf{k} . Similar to (2.5), the numerical displacement of harmonic plane waves u^n in an infinite medium for acoustic waves can be written as

$$u^n(\mathbf{x}, t) = \bar{u}^n \exp(i k(\mathbf{n} \cdot \mathbf{x} \pm c t)) \quad (2.7)$$

where c is the numerical wave velocity and \bar{u}^n is the amplitude of the acoustic wave. In this paper we study the numerical dispersion of linear finite elements on uniform meshes in the 1-D, 2-D and 3-D cases for elastodynamics and 2-D case for acoustic wave propagation problems. The following procedure is used. We calculate the nodal displacements in terms of known nodal coordinates using ((2.5) and (2.7), then insert them into (2.4) with $\mathbf{F} = \mathbf{0}$. From the solution of the residual equation $R(c) = 0$, we can estimate the corresponding numerical wave velocities c . Due to the numerical dispersion error, $R(c = c_o) \neq 0$ and the deviation of $R(c = c_o)$ from zero is related to the numerical dispersion error (the decrease in $|R(c = c_o)|$ corresponds to the decrease in the dispersion error). Because the wave propagates in all directions with the same velocity, then finite elements with the same dimensions along the coordinate axes will be used for wave propagation problems in the multi-dimensional cases (e.g., see [16, 73, 95] and others). For example, it was shown in [95] that in contrast to uniform finite element meshes with the same dimensions along the coordinate axes, uniform meshes with different dimensions along the coordinate axes do not allow to reduce the order of the dispersion error for acoustic wave propagating in different directions in the 2-D case.

In order to decrease the dispersion of finite element results, we consider the following two possibilities for the calculation of the mass and stiffness matrices: the

mass matrix \mathbf{M} is calculated as a weighted average of the consistent \mathbf{M}^{cons} and lumped \mathbf{D} mass matrices with the weighting factor γ (similar to that used in [58, 73, 82])

$$\mathbf{M}(\gamma) = \mathbf{D}\gamma + \mathbf{M}^{cons}(1 - \gamma) \quad (2.8)$$

or the mass and stiffness matrices of each finite element are calculated with the modified integration rule (similar to those used in [95])

$$\mathbf{M}^e(\alpha_M) = \rho A \int_{-1}^1 \mathbf{N}^T(s) \mathbf{N}(s) \det(\mathbf{J}) ds \approx \rho A \sum_{m=1}^2 \mathbf{N}^T((-1)^m \alpha_M) \mathbf{N}((-1)^m \alpha_M) \det(\mathbf{J}) \quad (2.9)$$

$$\mathbf{K}^e(\alpha_K) = A \int_{-1}^1 E \mathbf{B}^T(s) \mathbf{B}(s) \det(\mathbf{J}) ds \approx \sum_{m=1}^2 A E \mathbf{B}^T((-1)^m \alpha_K) \mathbf{B}((-1)^m \alpha_K) \det(\mathbf{J}) \quad (2.10)$$

in the 1-D case for elastodynamics problems,

$$\begin{aligned} \mathbf{M}^e(\alpha_M) &= \rho b \int_{-1}^1 \int_{-1}^1 \mathbf{N}^T(s, t) \mathbf{N}(s, t) \det(\mathbf{J}) ds dt \\ &\approx \rho b \sum_{m=1}^2 \sum_{j=1}^2 \mathbf{N}^T((-1)^m \alpha_M, (-1)^j \alpha_M) \mathbf{N}((-1)^m \alpha_M, (-1)^j \alpha_M) \det(\mathbf{J}) \end{aligned} \quad (2.11)$$

$$\begin{aligned} \mathbf{K}^e(\alpha_K) &= \int_{-1}^1 \int_{-1}^1 \mathbf{B}^T(s, t) \bar{\mathbf{C}} \mathbf{B}(s, t) \det(\mathbf{J}) ds dt \\ &\approx \sum_{m=1}^2 \sum_{j=1}^2 \mathbf{B}^T((-1)^m \alpha_K, (-1)^j \alpha_K) \bar{\mathbf{C}} \mathbf{B}((-1)^m \alpha_K, (-1)^j \alpha_K) \det(\mathbf{J}) \end{aligned} \quad (2.12)$$

in the 2-D case for elastodynamics problems,

$$\mathbf{M}^e(\alpha_M) = \rho \int_{-1}^1 \int_{-1}^1 \int_{-1}^1 \mathbf{N}^T(s, t, q) \mathbf{N}(s, t, q) \det(\mathbf{J}) ds dt dq$$

$$\begin{aligned} & \approx \rho \sum_{m=1}^2 \sum_{j=1}^2 \sum_{p=1}^2 \mathbf{N}^T((-1)^m \alpha_M, (-1)^j \alpha_M, (-1)^p \alpha_M) \\ & \quad \mathbf{N}((-1)^m \alpha_M, (-1)^j \alpha_M, (-1)^p \alpha_M) \det(\mathbf{J}), \end{aligned} \quad (2.13)$$

$$\begin{aligned} \mathbf{K}^e(\alpha_K) &= \int_{-1}^1 \int_{-1}^1 \int_{-1}^1 \mathbf{B}^T(s, t, q) \bar{\mathbf{C}} \mathbf{B}(s, t, q) \det(\mathbf{J}) ds dt dq \\ &\approx \sum_{m=1}^2 \sum_{j=1}^2 \sum_{p=1}^2 \mathbf{B}^T((-1)^m \alpha_K, (-1)^j \alpha_K, (-1)^p \alpha_K) \bar{\mathbf{C}} \\ & \quad \mathbf{B}((-1)^m \alpha_K, (-1)^j \alpha_K, (-1)^p \alpha_K) \det(\mathbf{J}) \end{aligned} \quad (2.14)$$

in the 3-D case for elastodynamics problems,

$$\begin{aligned} \mathbf{M}^e(\alpha_M) &= \int_{-1}^1 \int_{-1}^1 \mathbf{N}^T(s, t) \mathbf{N}(s, t) \det(\mathbf{J}) ds dt \\ &\approx \sum_{m=1}^2 \sum_{j=1}^2 \mathbf{N}^T((-1)^m \alpha_M, (-1)^j \alpha_M) \mathbf{N}((-1)^m \alpha_M, (-1)^j \alpha_M) \det(\mathbf{J}), \end{aligned} \quad (2.15)$$

$$\begin{aligned} \mathbf{K}^e(\alpha_K) &= c_o^2 \int_{-1}^1 \int_{-1}^1 \mathbf{B}^T(s, t) \mathbf{B}(s, t) \det(\mathbf{J}) ds dt \\ &\approx c_o^2 \sum_{m=1}^2 \sum_{j=1}^2 \mathbf{B}^T((-1)^m \alpha_K, (-1)^j \alpha_K) \mathbf{B}((-1)^m \alpha_K, (-1)^j \alpha_K) \det(\mathbf{J}) \end{aligned} \quad (2.16)$$

in the 2-D case for acoustic wave propagation problems. Here, \mathbf{N} is the standard finite element shape matrix and $\mathbf{B} = \frac{\partial \mathbf{N}}{\partial x}$ is its derivative. $\bar{\mathbf{C}}$ is the matrix of elastic coefficients:

$$\bar{\mathbf{C}} = \frac{E(1-\nu)}{(1+\nu)(1-2\nu)} \begin{pmatrix} 1 & \frac{\nu}{1-\nu} & 0 \\ \frac{\nu}{1-\nu} & 1 & 0 \\ 0 & 0 & \frac{1-2\nu}{2(1-\nu)} \end{pmatrix}$$

in the 2-D case of plane strain and

$$\bar{\mathbf{C}} = \frac{E(1-\nu)}{(1+\nu)(1-2\nu)} \begin{pmatrix} 1 & \frac{\nu}{1-\nu} & \frac{\nu}{1-\nu} & 0 & 0 & 0 \\ \frac{\nu}{1-\nu} & 1 & \frac{\nu}{1-\nu} & 0 & 0 & 0 \\ \frac{\nu}{1-\nu} & \frac{\nu}{1-\nu} & 1 & 0 & 0 & 0 \\ 0 & 0 & 0 & \frac{1-2\nu}{2(1-\nu)} & 0 & 0 \\ 0 & 0 & 0 & 0 & \frac{1-2\nu}{2(1-\nu)} & 0 \\ 0 & 0 & 0 & 0 & 0 & \frac{1-2\nu}{2(1-\nu)} \end{pmatrix}$$

in the 3-D case for elastodynamics problems; the diagonal terms of the lumped mass matrix \mathbf{D} (except those for the boundary nodes) for the linear elements are dx ; dx^2 ; dx^3 which are the line elements in the 1-D case, square elements in the 2-D case, and cubic elements in the 3-D case; \mathbf{J} is the Jacobian matrix ($\det(\mathbf{J}) = dx/2$; $dx^2/4$; $dx^3/8$ in the 1-D case, in the 2-D case for square elements and in the 3-D case for cubic elements, respectively; dx is the length of a finite element); A is the cross sectional area in the 1-D case; b is the thickness in the 2-D case of plane strain; s, t, q are the isoparametric coordinates; α_M and α_K are the coordinates of the integration points for the mass and stiffness matrices to be determined (2, $2 \times 2 = 4$ and $2 \times 2 \times 2 = 8$ integration points are used for linear elements in the 1-D, 2-D and 3-D cases, respectively); e.g., see [36, 9] for the derivation of finite element matrices. The integration error due to the application of the modified integration rule for the mass and stiffness matrices does not change the convergence rate of finite element solutions; see [95]. We use the dispersion analysis presented below in order to find such γ , α_M and α_K that reduce the dispersion error.

2.1 Analysis of numerical dispersion of elastodynamics problems in the 1-D case

For the analysis of the numerical phase velocity of harmonic plane wave on a uniform mesh in the 1-D case, only one algebraic expression for any node should be used. It can be obtained by the substitution of the nodal displacements calculated with the help of (2.5) into the left-hand side of (2.4) where the numerical wave velocity c is used in (2.5) instead of c_o . This expression R can be derived by considering of two adjacent elements with the common node (see Fig. 2.1a) and has the following form

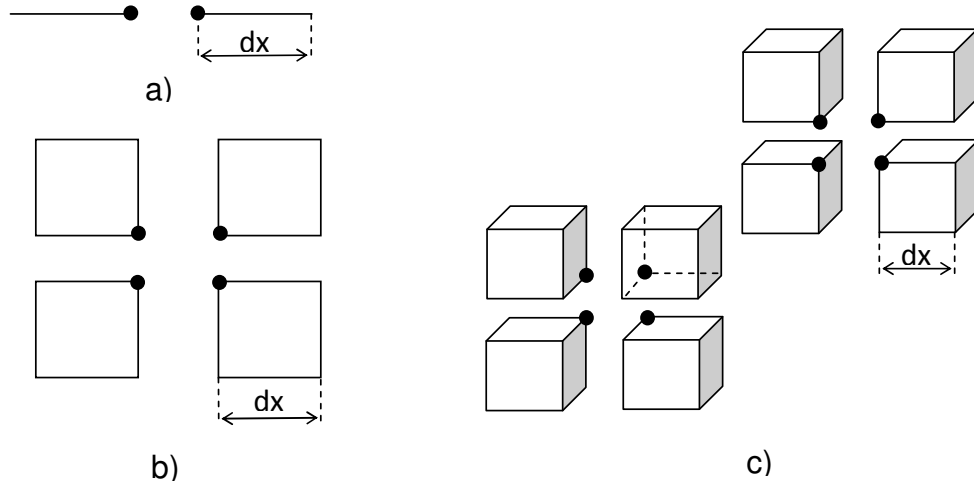


Figure 2.1: Adjacent quadrilateral finite elements used for the derivation of the dispersion equation for the common node in the 1-D (a), 2-D (b) and 3-D (c) cases.

$$R = \bar{R} \exp(ik(x - ct)) \quad (2.17)$$

where

$$\begin{aligned} \bar{R} = & \frac{3(\gamma + 1)c_o^2 + ((\gamma - 1)\cos(2kdx) - 2(2\gamma + 1)\cos(kdx))c_o^2}{3dx} \\ & + \frac{6dx^2(\cos(kc\Delta t) - 1)/\Delta t^2}{3dx} \end{aligned} \quad (2.18)$$

in the case of the averaged mass matrix, Eq. ((2.8)) and

$$\begin{aligned} \bar{R} = & \frac{(3\alpha_M^2 + 1) c_o^2 + ((\alpha_M^2 - 1) \cos(2kdx) - 4\alpha_M^2 \cos(kdx)) c_o^2}{2dx} \\ & + \frac{4dx^2(\cos(kc\Delta t) - 1)/\Delta t^2}{2dx} \end{aligned} \quad (2.19)$$

in the case of the modified integration rule, (2.9) (in the 1-D case the stiffness matrix K^e is constant for linear elements and is independent of the coordinates α_K of the integration points). Here $c_o = \sqrt{E/\rho}$ is the wave velocity in the 1-D case. Because for harmonic plane wave the right-hand side of (2.4) is zero, then this leads to the following algebraic equation $R(c) = \bar{R}(c) = 0$. From this equation we can find the numerical wave velocity c , the dispersion error $\frac{c-c_o}{c_o}$ and the parameters γ and α_M to reduce the dispersion error. The different between the numerical wave velocity c exact wave velocity c_o that leads to the numerical dispersion error ($\Delta c = c - c_o$). However, the same results related to the reduction in the wave velocity error can be obtained if we expand the residual \bar{R} of (2.18) or (2.19) into the Taylor series at $c = c_o$ (e.g., see the paper [43] for implicit methods). As can be seen from (2.18) and (2.19), the residual \bar{R} on uniform meshes is independent of x and t , and its expansion into the Taylor series at $c = c_o$ and small dx and Δt (i.e., at $kdx \ll 1$ and $kc_o\Delta t \ll 1$) yields

$$\bar{R}(c = c_o) = \frac{1}{12}c_o^2 dx^3 (\bar{\tau}^2 + 2\gamma - 3) k^4 + \frac{1}{360} (11 - 10\gamma - \bar{\tau}^4) c_o^2 dx^5 k^6 + O(dx^6) \quad (2.20)$$

for (2.18)

$$\bar{R}(c = c_o) = \frac{1}{12}c_o^2 dx^3 (3\alpha_M^2 + \bar{\tau}^2 - 4) k^4 + \frac{1}{360} (16 - 15\alpha_M^2 - \bar{\tau}^4) c_o^2 dx^5 k^6 + O(dx^6) \quad (2.21)$$

for (2.19) where $\bar{\tau} = \frac{c_o\Delta t}{dx}$ is the Courant number.

Due to the difference between the exact and numerical wave velocities for harmonic plane wave, the residual \bar{R} in (2.20) and (2.21) is non-zero at $c = c_0$. The smaller residual means the smaller difference between the exact and numerical wave

velocities. For small dx , the order of the leading term for the residual \bar{R} (the order of accuracy) increases at $\gamma = \gamma^{opt} = \frac{3-\bar{\tau}^2}{2}$ (see the first term in (2.20)) and at $\alpha_M = \alpha_M^{opt} = \sqrt{\frac{4-\bar{\tau}^2}{3}}$ (see the first term in (2.21)). We should mention that at $\bar{\tau} \approx 0$ (for very small time increments), the optimal value of $\gamma^{opt} = \frac{3}{2}$ coincides with the results obtained in [58] for the 1-D case. However, the size of time increments may significantly affect γ^{opt} . For example, the stability limit for the time integration of (2.4) on uniform meshes with linear elements equals $\Delta t^{st} = \frac{dx}{c_o}$ or $\bar{\tau} = 1$. In this case, $\gamma^{opt} = 1$ and $\mathbf{M} = \mathbf{D}$ (see (2.8)); i.e., for this particular case, (2.4) reduces to the standard finite element formulation with the lumped mass matrix (it is known that in the 1-D case, the standard linear finite elements and the explicit central difference method yields the exact solution to the 1-D impact problem at $\bar{\tau} = 1$; e.g., see [36]). It can be also seen that at $\gamma^{opt} = \frac{3-\bar{\tau}^2}{2}$, the first term in (2.20) is zero, the second term in (2.20) equals $\frac{1}{360}(\bar{\tau}^2 - 1)(\bar{\tau}^2 - 4)c_o^2 dx^5 k^6$ and is zero at $\bar{\tau} = 1$ and increases with the decrease in $\bar{\tau}$ (for $\bar{\tau} < 1$). This means that for linear elements with the averaged mass matrix and 1-D uniform meshes, the dispersion error increases with the decrease in the size of time increments Δt for time increments smaller than the stability limit.

At $\gamma = (3\alpha_M^2 - 1)/2$, (2.18) and (2.19) are equivalent and yield the same relationships between the exact c_o and numerical c wave velocities (with the optimal value of $\alpha_M^{opt} = \sqrt{\frac{4-\bar{\tau}^2}{3}}$ or the same as in [95]). The mass matrices calculated with the use of (2.8) and (2.9) are also equivalent at $\gamma = (3\alpha_M^2 - 1)/2$ (e.g., $\gamma = 1$ and $\alpha_M = \pm 1$ correspond to the lumped matrix). This means that the modified integration rule and the average mass matrix are completely equivalent techniques in the 1-D case.

2.2 Analysis of numerical dispersion of elastodynamics problems in the 2-D case

For the analysis of the numerical phase velocity of the harmonic plane wave on a uniform mesh in the 2-D case (plane strain), only two algebraic equations (for the x

and y directions) for any node should be used. They can be obtained by the substitution of the nodal displacements (calculated with the help of Eq. (2.5)) into Eq. (2.4). These two homogeneous equations, which are linear with respect to two unknown amplitudes \bar{u}_1 and \bar{u}_2 , can be determined by the consideration of four adjacent elements with the common node; see Fig. 2.1b. For non-zero amplitudes of the displacements \bar{u}_1 and \bar{u}_2 , the determinant R of the system of algebraic equations has to be zero. Due to lengthy expression for the determinant R , we present it only for small dx (dx is the length of a square finite element).

$$R = (a_4 dx^4 + a_6 dx^6 + O(dx^8)) \exp(2ik(x \cos(\Theta) + y \sin(\Theta) - ct)), \quad (2.22)$$

where the expressions for coefficients a_4 and a_6 are given below for different techniques.

2.2.1 The modified integration rule

In the case of the calculation of the mass and stiffness matrices with the help of Eqs. (2.11) and (2.12), the coefficients a_4 and a_6 can be found as follows:

$$\begin{aligned} a_4 &= \frac{1}{2\nu-1} k^4 \left(c^2 - \frac{\mu}{\rho} \right) \left(c^2(2\nu-1) - 2\frac{\mu}{\rho}(\nu-1) \right), \\ a_6 &= \frac{k^6}{96(c_2 - 2c_2\nu)^2} (16\tau^2(1-2\nu)^2 c^6 - 8(\frac{\mu}{\rho})\tau^2(2\nu(4\nu-5)+3)c^4 \\ &\quad + 6(4\alpha_M^2 + \alpha_K^2 - 6)c_2^2(\frac{\mu}{\rho})(2\nu(4\nu-5)+3)c^2 - 3c_2^2(\frac{\mu}{\rho})^2(32(\nu-1)(2\nu-1)\alpha_M^2 \\ &\quad + \alpha_K^2(3-4\nu)^2 - 48(\nu-1)(2\nu-1)) + c_2^2(\frac{\mu}{\rho})((\frac{\mu}{\rho})(3\alpha_K^2(3-4\nu)^2 - 16(\nu-1)(2\nu-1)) \\ &\quad - 2(3\alpha_K^2 - 2)c^2(2\nu(4\nu-5)+3)) \cos(4\Theta)). \end{aligned} \quad (2.23)$$

Here $\tau = \frac{c_2 \Delta t}{dx}$ is the Courant number, the components of the unit vector \mathbf{n} in Eq. (2.5) are represented as $n_1 = \cos(\Theta)$ and $n_2 = \sin(\Theta)$. The difference between the numerical and exact wave velocities for plane wave can be estimated by means of the leading term of the residual R in Eq. (2.22) at small dx for $c = c_1$ and for $c = c_2$

(see the explanations for the 1-D case). At $c = c_1$ and at $c = c_2$, coefficient a_4 is zero ($a_4 = 0$), and coefficient a_6 has the following forms:

$$\begin{aligned} a_6(c = c_1) &= \frac{k^6(\frac{\mu}{\rho})^2}{96(2\nu - 1)^3} \{ [-48(\nu - 1)(2\nu - 1)\alpha_M^2 - 8(4(\nu - 1)\tau^2 - 18\nu + 9)(\nu - 1) \\ &\quad - 3\alpha_K^2(2\nu(4\nu - 5) + 3)] + [(2\nu - 1)(3(4\nu - 3)\alpha_K^2 - 8\nu + 8)] \cos(4\Theta) \} \end{aligned} \quad (2.24)$$

and

$$\begin{aligned} a_6(c = c_2) &= -\frac{k^6(\frac{\mu}{\rho})^2}{96(1 - 2\nu)^2} \{ [24(2\nu - 1)\alpha_M^2 + 4(2\tau^2 - 9)(2\nu - 1) + 3\alpha_K^2(4\nu - 3)] \\ &\quad + [(9 - 12\nu)\alpha_K^2 + 8\nu - 4] \cos(4\Theta) \} . \end{aligned} \quad (2.25)$$

Assuming that the expressions in two square brackets of Eq. (2.24) (or Eq. (2.25)) are zeros, from these two algebraic equations we can find such α_K and α_M at which $a_6(c = c_1) = 0$ (or $a_6(c = c_2) = 0$). Unfortunately, these solutions for α_K and α_M are different for Eqs. (2.24) and (2.25). This means that we can only find such α_K and α_M at which a_6 is zero for one of Eqs. (2.24) and (2.25); i.e., at $\alpha_M = \sqrt{\frac{4-\tau^2}{3}}$ and $\alpha_K = \sqrt{\frac{4(2\nu-1)}{3(4\nu-3)}}$ equations (2.24) and (2.25) reduce to

$$\begin{aligned} a_6(c = c_1, \alpha_M &= \sqrt{\frac{4 - \tau^2}{3}}, \alpha_K = \sqrt{\frac{4(2\nu - 1)}{3(4\nu - 3)}}) \\ &= \frac{k^6(\frac{\mu}{\rho})^2}{24(2\nu - 1)^3} (4(\nu - 1)\tau^2 - 2\nu + (2\nu - 1) \cos(4\Theta) + 1) , \\ a_6(c = c_2, \alpha_M &= \sqrt{\frac{4 - \tau^2}{3}}, \alpha_K = \sqrt{\frac{4(2\nu - 1)}{3(4\nu - 3)}}) &= 0 \end{aligned} \quad (2.26)$$

or at $\alpha_M = \sqrt{\frac{4-(\tau c_1/c_2)^2}{3}}$ and $\alpha_K = \sqrt{\frac{8(1\nu-1)}{3(4\nu-3)}}$ equations (2.24) and (2.25) reduce to

$$a_6(c = c_1, \alpha_M = \sqrt{\frac{4 - (\tau c_1/c_2)^2}{3}}, \alpha_K = \sqrt{\frac{8(1\nu - 1)}{3(4\nu - 3)}}) = 0 ,$$

$$\begin{aligned}
a_6(c = c_2, \alpha_M &= \sqrt{\frac{4 - (\tau c_1/c_2)^2}{3}}, \alpha_K = \sqrt{\frac{8(1\nu - 1)}{3(4\nu - 3)}}) \\
&= \frac{k^6(\frac{\mu}{\rho})^2}{24(1 - 2\nu)^2} (2\tau^2 + \cos(4\Theta) - 1). \tag{2.27}
\end{aligned}$$

As will be shown later (see Eq. (3.3) below), the plane wave with velocity $c = c_2$ yield a greater error in numerical solutions than the plane wave with velocity $c = c_1$. Therefore, the optimal choice for the selection of α_M and α_K corresponds to $\alpha_M = \sqrt{\frac{4-\tau^2}{3}}$ and $\alpha_K = \sqrt{\frac{4(2\nu-1)}{3(4\nu-3)}}$ used in Eq. (2.26). In this case (see Eq. (2.26)), coefficient $a_6 = 0$ is zero for the shear plane wave ($c = c_2$) propagating in all directions at any τ and for the compressional plane wave ($c = c_1$) propagating along the x_1 ($\Theta = 0$) or x_2 ($\Theta = \pi/2$) axis at $\tau = 0$ (for very small time increments).

Similar results can be found if the mass matrix is calculated according to Eq. (2.8) and the stiffness matrix is calculated according to Eq. (2.12). In this case, coefficient a_4 is the same as in Eq. (2.23) and coefficient a_6 is calculated as follows:

$$\begin{aligned}
a_6 &= \frac{k^6}{96(\frac{\mu}{\rho})(1 - 2\nu)^2} (16\tau^2(1 - 2\nu)^2c^6 - 8(\frac{\mu}{\rho})\tau^2(2\nu(4\nu - 5) + 3)c^4 \\
&\quad + 2(3\alpha_K^2 + 8\gamma - 14)(\frac{\mu}{\rho})^2(2\nu(4\nu - 5) + 3)c^2 + (\frac{\mu}{\rho})^3(-3\alpha_K^2(3 - 4\nu)^2 - 16(4\gamma - 7)(\nu - 1)(2\nu - 1)) \\
&\quad + (\frac{\mu}{\rho})^2((\frac{\mu}{\rho})(3\alpha_K^2(3 - 4\nu)^2 - 16(\nu - 1)(2\nu - 1)) - 2(3\alpha_K^2 - 2)c^2(2\nu(4\nu - 5) + 3)) \cos(4\Theta)). \tag{2.28}
\end{aligned}$$

Then, similar to the use of modified integration rule for the mass matrix in Eqs. (2.26) and (2.27), coefficient a_6 is zero for one of the plane waves at $\gamma = \frac{3-\tau^2}{2}$ and $\alpha_K = \sqrt{\frac{4(2\nu-1)}{3(4\nu-3)}}$

$$\begin{aligned}
a_6(c = c_1, \gamma &= \frac{3 - \tau^2}{2}, \alpha_K = \sqrt{\frac{4(2\nu - 1)}{3(4\nu - 3)}}) \\
&= a_6(c = c_1, \alpha_M = \sqrt{\frac{4 - \tau^2}{3}}, \alpha_K = \sqrt{\frac{4(2\nu - 1)}{3(4\nu - 3)}}),
\end{aligned}$$

$$a_6(c = c_2, \gamma = \frac{3 - \tau^2}{2}, \alpha_K = \sqrt{\frac{4(2\nu - 1)}{3(4\nu - 3)}}) = 0 \quad (2.29)$$

or at $\gamma = \frac{3-\tau^2}{2}$ and $\alpha_K = \sqrt{\frac{8(1\nu-1)}{3(4\nu-3)}}$

$$\begin{aligned} a_6(c = c_1, \gamma = \frac{3 - (\tau c_1/c_2)^2}{2}, \alpha_K = \sqrt{\frac{8(1\nu-1)}{3(4\nu-3)}}) &= 0, \\ a_6(c = c_2, \gamma = \frac{3 - (\tau c_1/c_2)^2}{2}, \alpha_K = \sqrt{\frac{8(1\nu-1)}{3(4\nu-3)}}) \\ &= a_6(c = c_2, \alpha_M = \sqrt{\frac{4 - (\tau c_1/c_2)^2}{3}}, \alpha_K = \sqrt{\frac{8(1\nu-1)}{3(4\nu-3)}}). \end{aligned} \quad (2.30)$$

However, we should mention that in contrast to the 1-D case, the mass matrices calculated by the use of Eq. (2.11) at $\alpha_M = \sqrt{\frac{4-\tau^2}{3}}$ and by the use of Eq. (2.8) at $\gamma = \frac{3-\tau^2}{2}$ are different in the 2-D case; e.g., at $\tau = 0$ these matrices are:

$$\mathbf{M}(\alpha_M = \sqrt{\frac{4}{3}}) = \left(\begin{array}{cccccccc} 49 & 0 & -7 & 0 & 1 & 0 & -7 & 0 \\ 0 & 49 & 0 & -7 & 0 & 1 & 0 & -7 \\ -7 & 0 & 49 & 0 & -7 & 0 & 1 & 0 \\ 0 & -7 & 0 & 49 & 0 & -7 & 0 & 1 \\ 1 & 0 & -7 & 0 & 49 & 0 & -7 & 0 \\ 0 & 1 & 0 & -7 & 0 & 49 & 0 & -7 \\ -7 & 0 & 1 & 0 & -7 & 0 & 49 & 0 \\ 0 & -7 & 0 & 1 & 0 & -7 & 0 & 49 \end{array} \right) \frac{\rho dx^2}{144} \quad (2.31)$$

and

$$\mathbf{M}(\gamma = \frac{3}{2}) = \begin{pmatrix} 46 & 0 & -4 & 0 & -2 & 0 & -4 & 0 \\ 0 & 46 & 0 & -4 & 0 & -2 & 0 & -4 \\ -4 & 0 & 46 & 0 & -4 & 0 & -2 & 0 \\ 0 & -4 & 0 & 46 & 0 & -4 & 0 & -2 \\ -2 & 0 & -4 & 0 & 46 & 0 & -4 & 0 \\ 0 & -2 & 0 & -4 & 0 & 46 & 0 & -4 \\ -4 & 0 & -2 & 0 & -4 & 0 & 46 & 0 \\ 0 & -4 & 0 & -2 & 0 & -4 & 0 & 46 \end{pmatrix} \frac{\rho dx^2}{144}. \quad (2.32)$$

The selection of time increments Δt (or τ) in the 2-D case differs from that in the 1-D case described in Section 2.1. Because we can zero the coefficient a_6 in the expression for the dispersion error, Eqs. (2.24) and (2.25), for one plane wave with $c = c_1$ or $c = c_2$, then for another plane wave we can only minimize non-zero coefficient a_6 by the selection of τ (or Δt). Let us consider non-zero coefficient a_6 in the first formula of Eq. (2.26). If we find τ from the condition that $a_6(c = c_1, \alpha_M = \sqrt{\frac{4-\tau^2}{3}}, \alpha_K = \sqrt{\frac{4(2\nu-1)}{3(4\nu-3)}}) = 0$ then we will get $\tau^2 = \frac{(1-2\nu)\sin^2(2\Theta)}{2(1-\nu)}$. This means that τ is different for different Θ and $a_6(c = c_1, \alpha_M = \sqrt{\frac{4-\tau^2}{3}}, \alpha_K = \sqrt{\frac{4(2\nu-1)}{3(4\nu-3)}})$ cannot be zero for all Θ for the compressional plane wave with $c = c_1$. As we mentioned before, in order to zero a_6 for the compressional plane wave propagating along the x_1 ($\Theta = 0$) or x_2 ($\Theta = \pi/2$) we should use very small time increments Δt at which τ is close to zero. We will also analyze the selection of optimal time increments using numerical experiments (see Section IV below).

It is interesting to note that small time increments are also required for the dispersion-reduction technique used in the paper [43] with the implicit trapezoidal rule. It seems that for any time-integration method, the error in time is minimal compared to the error in space in the multidimensional case. Therefore, small time increments can be recommended for the reduction of the error in time.

2.2.2 The averaged mass matrix

For the averaged mass matrix, coefficient a_4 is the same as that in Eq. (2.23) and coefficient a_6 is given by Eq. (2.28). At $\gamma = \frac{3-\tau^2}{2}$ (as in Eq. (2.29)) and the standard stiffness matrix (this corresponds to the use of Eq. (2.12) with $\alpha_K = \sqrt{\frac{1}{3}}$), it follows from Eq. (2.28) that in the general case, coefficient a_6 is non-zero for both plane waves at $c = c_1$ and at $c = c_2$ (coefficient a_4 is zero); i.e.,

$$\begin{aligned} a_6(c = c_1, \gamma = \frac{3 - \tau^2}{2}, \alpha_K = \sqrt{\frac{1}{3}}) \\ = \frac{k^6(\frac{\mu}{\rho})^2}{96(2\nu - 1)^3} (16(\nu - 1)\tau^2 + 2\nu(4\nu - 7) + (2(7 - 4\nu)\nu - 5) \cos(4\Theta) + 5), \\ a_6(c = c_2, \gamma = \frac{3 - \tau^2}{2}, \alpha_K = \sqrt{\frac{1}{3}}) = \frac{k^6(\frac{\mu}{\rho})^2(-1 + 4\nu) \sin^2(2\Theta)}{48(1 - 2\nu)^2}. \end{aligned} \quad (2.33)$$

However, coefficient a_6 is zero for the plane wave propagating along the x_1 ($\Theta = 0$) or x_2 ($\Theta = \pi/2$) axis at any τ for the shear wave ($c = c_2$) and at $\tau = 0$ (for very small time increments) for the compressional wave ($c = c_1$); see Eq. (2.33). We will also analyze the selection of optimal time increments using numerical experiments (see Section IV below).

2.2.3 Existing approaches

For the existing approaches with the lumped ($\gamma = 1$) mass matrix and the standard stiffness matrix ($\alpha_K = \sqrt{\frac{1}{3}}$), coefficient a_6 is non-zero and has the following values (coefficient a_4 is zero at $c = c_1$ and at $c = c_2$):

$$\begin{aligned} a_6(c = c_1, \gamma = 1, \alpha_K = \sqrt{\frac{1}{3}}) \\ = \frac{k^6(\frac{\mu}{\rho})^2}{96(2\nu - 1)^3} (-32\tau^2(\nu - 1)^2 + 40\nu^2 - 62\nu + (2(7 - 4\nu)\nu - 5) \cos(4\Theta) + 21), \end{aligned}$$

$$\begin{aligned}
& a_6(c = c_2, \gamma = 1, \alpha_K = \sqrt{\frac{1}{3}}) \\
&= \frac{k^6(\frac{\mu}{\rho})^2}{96(1 - 2\nu)^2} (8(2\nu - 1)\tau^2 - 20\nu + (4\nu - 1)\cos(4\Theta) + 9). \quad (2.34)
\end{aligned}$$

Using these results, we can estimate the effect of a time increment Δt (or τ) on the dispersion error for the standard central difference with the lumped mass matrix in the 2-D case. For example, as show our numerical results and the formula (3.3) (see also the paper [47]), the range of spurious oscillations and the accuracy of numerical results are defined by the harmonic wave propagating with the velocity c_2 or by the coefficient $a_6(c = c_2, \gamma = 1, \alpha_K = \sqrt{\frac{1}{3}})$ in Eq. (2.34). This coefficient is zero at $\tau^2 = \tau_0^2 = \frac{20\nu+(1-4\nu)\cos(4\Theta)-9}{16\nu-8}$. However, admissible τ^2 may vary between $0 \leq \tau^2 \leq \tau_{max}^2$ where $\tau_{max} = \frac{c_2 \Delta t^{st}}{dx}$.

The stability limit Δt^{st} in the 2-D case for the plane strain state equals $\Delta t^{st} = \frac{dx}{c_1}$; e.g., see [16]. This means that $\tau_{max} = \frac{c_2}{c_1} = \sqrt{1 - \frac{1}{2(1-\nu)}}$. The comparison of these expressions for τ_0^2 and τ_{max}^2 shows that at $0 \leq \nu \leq \frac{9-\sqrt{33}}{8} = 0.40693$, we have $\tau_0^2 \geq \tau_{max}^2$ at any Θ . This means that coefficient $a_6(c = c_2, \gamma = 1, \alpha_K = \sqrt{\frac{1}{3}})$ in Eq. (2.34) has the minimum value at $\tau = \tau_{max}$ among all admissible τ and $0 \leq \nu \leq 0.40693$. For $0.40693 < \nu \leq 0.5$ and some angles Θ , the coefficient $a_6(c = c_2, \gamma = 1, \alpha_K = \sqrt{\frac{1}{3}})$ in Eq. (2.34) has the minimum value for $\tau < \tau_{max}$ (or for $\Delta t < \Delta t^{st}$). However, even at $\tau = \tau_{max}$ (or $\Delta t = \Delta t^{st}$), the difference between coefficient $a_6(c = c_2, \gamma = 1, \alpha_K = \sqrt{\frac{1}{3}})$ at $\Delta t = \Delta t^{st}$ ($\tau = \tau_{max}$) and $\Delta t = 0$ ($\tau = 0$) is not very big. For example, for different angles Θ , the ratio $\frac{a_6(\Delta t = \Delta t^{st})}{a_6(\Delta t = 0)}$ for coefficient $a_6(c = c_2, \gamma = 1, \alpha_K = \sqrt{\frac{1}{3}})$ in Eq. (2.34) varies between $0.55 \div 0.63$ at $\nu = 0.1$, $0.67 \div 0.72$ at $\nu = 0.3$, $0.35 \div 0.83$ at $\nu = 0.4$. These results are very different from the 1-D case for which the dispersion error and the corresponding coefficients in the Taylor series for the dispersion error are zero at $\Delta t = \Delta t^{st}$ (see the discussion after Eq. (2.21)).

2.3 Analysis of numerical dispersion of elastodynamics problems in the 3-D case

For the analysis of the numerical phase velocity of the plane wave on a uniform mesh in the 3-D case, only three algebraic equations (for the three directions along the axes of the Cartesian coordinate system) for any node should be used. They can be obtained by the substitution of the nodal displacements (calculated with the help of Eq. (2.5)) into Eq. (2.4). These three homogeneous equations, which are linear with respect to three unknown amplitudes \bar{u}_1 , \bar{u}_2 and \bar{u}_3 , can be determined by the consideration of eight adjacent elements with the common node; see Fig. 2.1c. For non-zero solutions for the displacements \bar{u}_1 , \bar{u}_2 and \bar{u}_3 , the determinant R of the system of algebraic equations has to be zero. Due to lengthy expression for the determinant R , we present it only for small dx (dx is the length of a cubic finite element):

$$R = (a_6 dx^6 + a_8 dx^8 + a_{10} dx^{10} + O(dx^{11}))$$

$$\exp(3ik(x \cos(\Theta) + y \sin(\Theta) \cos(\Psi) + z \sin(\Theta) \sin(\Psi) - ct)) \quad (2.35)$$

with

$$a_6 = \frac{1}{2\nu - 1} k^6 \left(c^2 - \frac{\mu}{\rho} \right)^2 \left(c^2(2\nu - 1) - 2\frac{\mu}{\rho}(\nu - 1) \right). \quad (2.36)$$

Here the components of the unit vector \mathbf{n} in Eq. (2.5) are represented in terms of two angles Θ and Ψ as $n_1 = \cos(\Theta)$, $n_2 = \sin(\Theta) \cos(\Psi)$ and $n_3 = \sin(\Theta) \sin(\Psi)$. At $c = c_1$ and at $c = c_2$, coefficient a_6 is zero (see Eq. (2.36)). At $c = c_2$, coefficient a_8 is zero at any α_M and α_K (in the 3-D case there are three roots of the determinant for the phase velocity c , two of them are the same and equal $c = c_2$). In the 3-D case, the increase in accuracy for the calculation of the phase velocity corresponds to the decrease in the absolute value of coefficient a_8 at $c = c_1$ and to the decrease in the absolute value of coefficient a_{10} at $c = c_2$.

2.3.1 The modified integration rule

Below we present coefficients a_8 and a_{10} at the optimal values of $\alpha_M = \sqrt{\frac{4-\tau^2}{3}}$ and $\alpha_K = \sqrt{\frac{4(2\nu-1)}{3(4\nu-3)}}$ determined above in the 2-D case:

$$\begin{aligned}
& a_8(c = c_1, \alpha_M = \sqrt{\frac{4-\tau^2}{3}}, \alpha_K = \sqrt{\frac{4(2\nu-1)}{3(4\nu-3)}}) \\
&= \frac{k^8 \frac{\mu}{\rho}^3}{768(1-2\nu)^4(4\nu-3)} (-48 \cos(4\Psi) \sin^4(\Theta) - 128\tau^2(\nu-1)(4\nu-3) + 2(2\nu-1)(82\nu-63) \\
&\quad - 78 \cos(4\Theta) - 3 \cos(6\Theta) + \cos(2\Theta)(48(1-2\nu)^2 \cos(4\Psi) \sin^4(\Theta) - 116\nu^2 + 148\nu - 45) \\
&\quad + 4\nu(-16(\nu-2) \cos(4\Psi) \sin^4(\Theta)(64-50\nu) \cos(4\Theta) - 3(\nu-1) \cos(6\Theta))) , \\
& a_{10}(c = c_2, \alpha_M = \sqrt{\frac{4-\tau^2}{3}}, \alpha_K = \sqrt{\frac{4(2\nu-1)}{3(4\nu-3)}}) \\
&= \frac{k^{10} \left(\frac{\mu}{\rho}\right)^3 \sin^4(\Theta) \sin^2(2\Theta) \sin^2(2\Psi)}{576(3-4\nu)^2(2\nu-1)} (-2 \cos(4\Psi) \sin^2(\Theta) + 7 \cos(2\Theta) + 9). \quad (2.37)
\end{aligned}$$

Similar results can be found if the mass matrix is calculated according to Eq. (2.8) (the averaged mass matrix) and the stiffness matrix is calculated according to Eq. (2.14) (the modified integration rule). In this case

$$\begin{aligned}
& a_8(c = c_1, \gamma = \frac{3-\tau^2}{2}, \alpha_K = \sqrt{\frac{4(2\nu-1)}{3(4\nu-3)}}) \\
&= a_8(c = c_1, \alpha_M = \sqrt{\frac{4-\tau^2}{3}}, \alpha_K = \sqrt{\frac{4(2\nu-1)}{3(4\nu-3)}}), \\
& a_{10}(c = c_2, \gamma = \frac{3-\tau^2}{2}, \alpha_K = \sqrt{\frac{4(2\nu-1)}{3(4\nu-3)}}) \\
&= a_{10}(c = c_2, \alpha_M = \sqrt{\frac{4-\tau^2}{3}}, \alpha_K = \sqrt{\frac{4(2\nu-1)}{3(4\nu-3)}}); \quad (2.38)
\end{aligned}$$

i.e., coefficients a_8 and a_{10} are the same as in Eq. (2.37). However, the mass matrices calculated by the use of Eq. (2.8) at $\gamma = \frac{3-\tau^2}{2}$ or by the use of Eq. (2.13) at $\alpha_M = \sqrt{\frac{4-\tau^2}{3}}$ are different (similar to the considered 2-D case).

As can be seen from Eq. (2.37), in the 3-D case (in contrast to the 1-D and 2-D cases) the modified integration rule for the mass and stiffness matrices does not increase the order of accuracy of the phase velocity of the shear plane wave for all possible directions of the unit vector \mathbf{n} . However, for the harmonic shear wave ($c = c_2$) propagating in the planes x_1x_2 ($\Psi = 0$), x_1x_3 ($\Psi = \pi/2$) or x_2x_3 ($\Theta = \pi/2$), coefficient a_{10} is zero $a_{10} = 0$ at any τ (see Eq. (2.37)); i.e., the order of accuracy in the calculation of the phase velocity of the harmonic shear wave in these directions is increased at $\alpha_M = \sqrt{\frac{4-\tau^2}{3}}$ (or $\gamma = \frac{3-\tau^2}{2}$) and $\alpha_K = \sqrt{\frac{4(2\nu-1)}{3(4\nu-3)}}$.

For the compressional harmonic plane wave ($c = c_1$) propagating in the directions of the x_1 ($\Theta = 0$), x_2 ($\Theta = \pi/2$ and $\Psi = 0$) or x_3 ($\Theta = \pi/2$ and $\Psi = \pi/2$) axis, the coefficient $a_8 = 0$ at $\tau = 0$ (or very small time increments); i.e., the order of accuracy in the calculation of the phase velocity of the harmonic compressional wave in these directions is increased at $\alpha_M = \sqrt{\frac{4}{3}}$ (or $\gamma = \frac{3}{2}$), $\alpha_K = \sqrt{\frac{4(2\nu-1)}{3(4\nu-3)}}$ and $\tau = 0$ (i.e., at very small time increments $\Delta t \approx 0$).

2.3.2 The averaged mass matrix

Below we present coefficients a_8 and a_{10} for the averaged mass matrix with the optimal value of $\gamma = \frac{3-\tau^2}{2}$ and the standard stiffness matrix ($\alpha_K = \sqrt{\frac{1}{3}}$):

$$\begin{aligned} a_8(c = c_1, \gamma = \frac{3-\tau^2}{2}, \alpha_K = \sqrt{\frac{1}{3}}) &= \frac{k^8(\frac{\mu}{\rho})^3}{3072(1-2\nu)^4} (-16(2\nu-1)(8\nu-7) \cos(4\Psi) \sin^4(\Theta) \\ &+ 352\nu^2 + 512\tau^2(\nu-1) - 604\nu - 2(2\nu-1)(56\nu-67) \cos(4\Theta) + 6\nu \cos(6\Theta) - 3 \cos(6\Theta) \\ &- (2\nu-1) \cos(2\Theta)(48 \cos(4\Psi) \sin^4(\Theta) + 64\nu - 77) + 214), \\ a_{10}(c = c_2, \gamma = \frac{3-\tau^2}{2}, \alpha_K = \sqrt{\frac{1}{3}}) &= \frac{k^{10}(\frac{\mu}{\rho})^3 \sin^4(\Theta)}{589824(2\nu-1)^3} [16(4\nu(8\nu-9) \end{aligned}$$

$$\begin{aligned}
& + (7 - 12\nu) \cos(2\Theta) + 11) \cos(8\Psi) \sin^4(\Theta) - 16(12\nu(48\nu - 49) + 8(56\nu^2 - 66\nu + 21) \cos(2\Theta) \\
& + (21 - 36\nu) \cos(4\Theta) + 163) \cos(4\Psi) \sin^2(\Theta) + 27200\nu^2 - 20856\nu + 32000\nu^2 \cos(2\Theta) \\
& - 24156\nu \cos(2\Theta) + 4091 \cos(2\Theta) + 6336\nu^2 \cos(4\Theta) - 4296\nu \cos(4\Theta) + 526 \cos(4\Theta) \\
& + 156\nu \cos(6\Theta) - 91 \cos(6\Theta) + 3666] . \tag{2.39}
\end{aligned}$$

Similar to the 2-D case, for the averaged mass matrix the order of accuracy in the calculation of the phase velocity of the plane wave propagating in the directions of the x_1 ($\Theta = 0$), x_2 ($\Theta = \pi/2$ and $\Psi = 0$) or x_3 ($\Theta = \pi/2$ and $\Psi = \pi/2$) axis is increased for the shear plane wave at any τ and for the compressional plane wave at $\tau = 0$ (for very small time increments $\Delta t \approx 0$). In these cases, coefficients a_8 and a_{10} are zero; see Eq. (2.39).

2.4 Analysis of numerical dispersion of acoustic wave propagation problems in the 2-D case

Due to the lengthy expression for $R(c = c_o)$, we present it only for small Δt and dx (dx is the length of a square finite element) using a Taylor series

$$R(c = c_o) = (a_4 k^4 dx^4 + a_6 k^6 dx^6 + O(dx^8)) , \tag{2.40}$$

where the expressions for coefficients a_4 and a_6 are given below for the different techniques.

2.4.1 The modified integration rule

In the case of the calculation of the mass and stiffness matrices with the help of Eqs. (2.15) and (2.16), the coefficients a_4 and a_6 can be found as follows:

$$a_4 = \frac{1}{48} \{ [-4\tau^2 - 3(4\alpha_M^2 + \alpha_K^2 - 6)] + [3\alpha_K^2 - 2] \cos(4\Theta) \} ,$$

$$a_6 = \frac{1}{5760} \{ 16\tau^4 - 5[9(\alpha_M^2 + 2\alpha_K^2 - 8)\alpha_M^2 - 24\alpha_K^2 + 71] \\ + 3[5(3\alpha_M^2 + 6\alpha_K^2 - 8)\alpha_M^2 - 40\alpha_K^2 + 33] \cos(4\Theta) \}. \quad (2.41)$$

Here $\tau = \frac{c_o \Delta t}{dx}$ is the Courant number, the components of the unit vector \mathbf{n} in Eq. (2.5) are represented as $n_1 = \cos(\Theta)$ and $n_2 = \sin(\Theta)$. Assuming that the expressions in two square brackets for coefficient a_4 in Eq. (2.41) are zeros, from these two algebraic equations we can find such $\alpha_K = \sqrt{\frac{2}{3}}$ and $\alpha_M = \sqrt{\frac{4-\tau^2}{3}}$ at which $a_4 = 0$ and the dispersion error is decreased from the second order to the fourth order. The coefficient a_6 in this case is

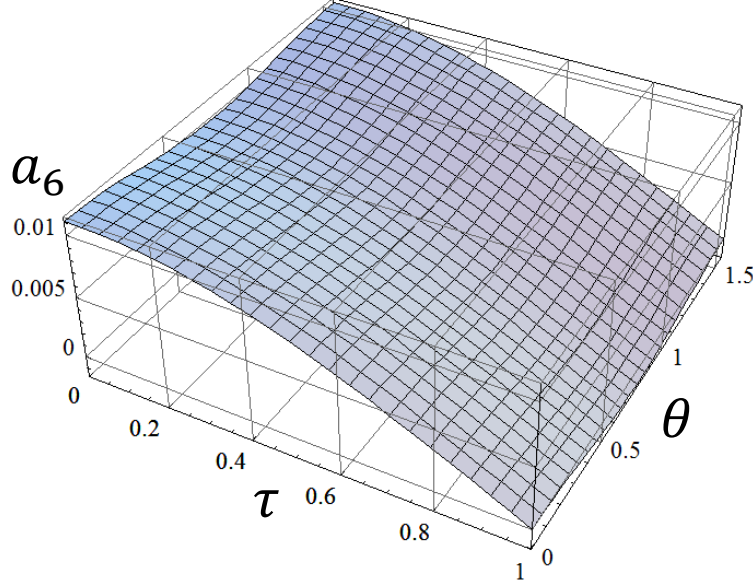
$$a_6(\alpha_M = \sqrt{\frac{4-\tau^2}{3}}, \alpha_K = \sqrt{\frac{2}{3}}) = \frac{11\tau^4 - 60\tau^2 + (5\tau^4 - 20\tau^2 + 19) \cos(4\Theta) + 45}{5760}. \quad (2.42)$$

A time increment Δt for the explicit central difference method can vary between zero and the stability limit Δt^{st} ; i.e., $0 \leq \Delta t \leq \Delta t^{st}$. As a consequence, the range of the Courant number is $0 \leq \tau \leq \tau^{st} = \frac{c_o \Delta t^{st}}{dx}$. As shown in [95], $\tau^{st} = 0.7587$ for the modified integration rule technique. The analysis of Eq. (2.42) (see also Fig. 2.2) shows that at any angle Θ , the absolute value of coefficient $a_6(\alpha_M = \sqrt{\frac{4-\tau^2}{3}}, \alpha_K = \sqrt{\frac{2}{3}})$ has the minimum value at $\tau = \tau^{st}$; i.e., the dispersion error has a minimum value at time increments close to the stability limit Δt^{st} ; see also curve 1 in Fig. 2.3 for a_6 at $\tau = \tau^{st}$.

2.4.2 The averaged mass matrix

Another way to reduce the numerical dispersion is based on the calculation of the mass matrix according to Eq. (2.8) and the stiffness matrix according to Eq. (2.12). In this case, coefficients a_4 and a_6 in Eq. (2.40) are as follows:

$$a_4 = \frac{1}{48} \{ [-3\alpha_K^2 - 4\tau^2 - 8\gamma + 14] + [3\alpha_K^2 - 2] \cos(4\Theta) \}$$

Figure 2.2: Coefficient a_6 in Eq. (2.42) as a function of Θ and τ .

$$a_6 = \frac{(45 - 30\gamma)\alpha_K^2 + 4(2\tau^4 + 25\gamma - 30) + (15(2\gamma - 3)\alpha_K^2 - 20\gamma + 32)\cos(4\Theta)}{2880}. \quad (2.43)$$

Assuming that the expressions in two square brackets for coefficient a_4 in Eq. (2.43) are zeros, from these two algebraic equations we can find such $\alpha_K = \sqrt{\frac{2}{3}}$ and $\gamma = \frac{3-\tau^2}{2}$ at which $a_4 = 0$ and the dispersion error decreases from the second order to the fourth order. The coefficient a_6 in this case is

$$a_6(\gamma = \frac{3-\tau^2}{2}, \alpha_K = \sqrt{\frac{2}{3}}) = \frac{15 - 20\tau^2 + \tau^4 + \cos(4\Theta)}{1440}. \quad (2.44)$$

As shown in [95], $\tau^{st} = 0.805$ in this case. The analysis of Eq. (2.44) (see also Fig. 2.4) shows that at any angle Θ , the absolute value of coefficient $a_6(\gamma = \frac{3-\tau^2}{2}, \alpha_K = \sqrt{\frac{2}{3}})$ has the minimum value at $\tau = \tau^{st}$; i.e., the dispersion error has a minimum value at time increments close to the stability limit Δt^{st} ; see also curve 2 in Fig. 2.3 for a_6 at $\tau = \tau^{st}$. From Figs. 2.2 and 2.4 we can also see that the maximum dispersion error (or the maximum absolute value of coefficient a_6) in the 2-D case occurs for the acoustic wave propagating along the Cartesian axes with $\Theta = 0, \frac{\pi}{2}$ for the two cases

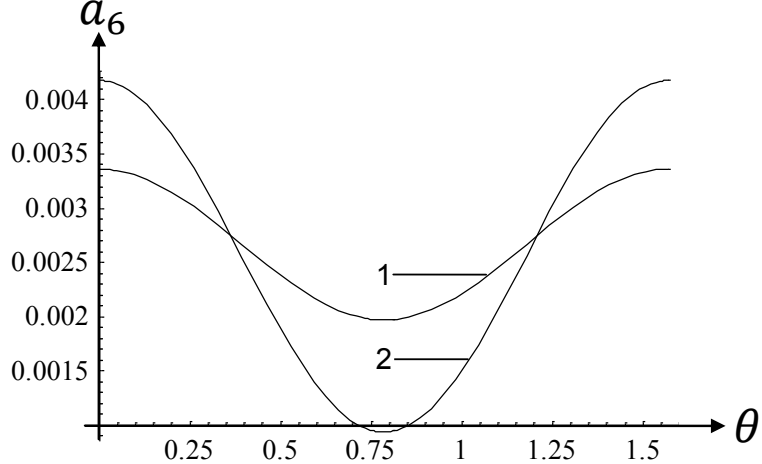


Figure 2.3: Coefficients a_6 in Eq. (2.44) at $\tau = \tau^{st} = 0.805$ (curve 1) and in Eq. (2.42) at $\tau = \tau^{st} = 0.7587$ (curve 2) as a function of Θ .

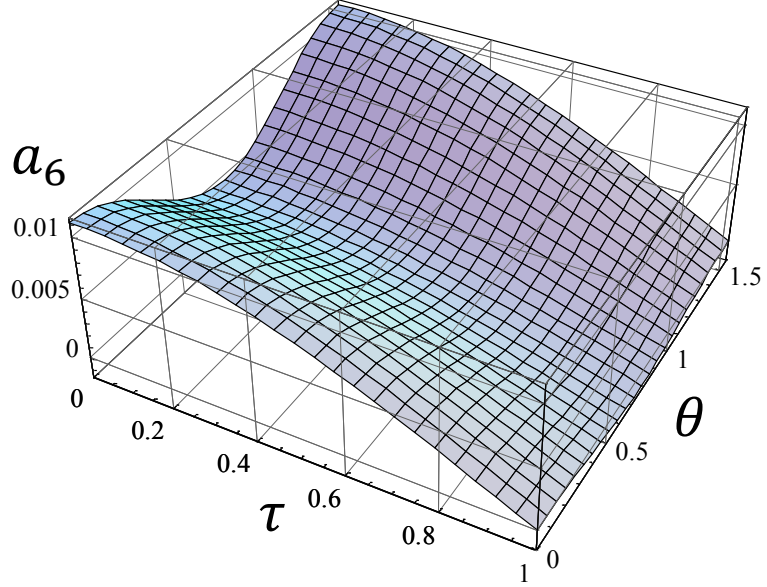
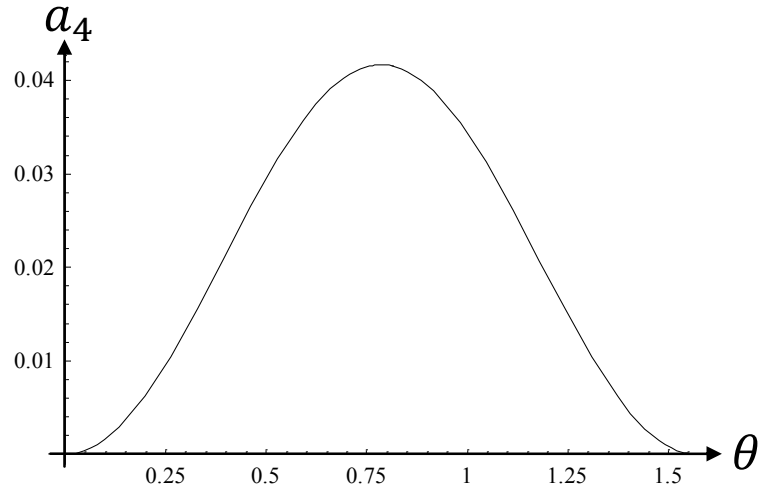
considered above; at $\tau = \tau^{st}$ for each technique, this error is slightly smaller for the technique with $\gamma = \frac{3-\tau^2}{2}$ and $\alpha_K = \sqrt{\frac{2}{3}}$; see curves 1 and 2 in Fig. 2.3. Therefore, for the numerical examples in Section IV we will consider the technique with reduced dispersion based on $\gamma = \frac{3-\tau^2}{2}$ and $\alpha_K = \sqrt{\frac{2}{3}}$ (this technique also allows slightly larger time increments compared with those for the technique based on $\alpha_M = \sqrt{\frac{4-\tau^2}{3}}$ and $\alpha_K = \sqrt{\frac{2}{3}}$ as indicated above).

The dispersion error for the approaches based on the averaged mass matrix and the standard stiffness matrix (e.g., see [58]) can be also obtained from Eq. (2.43). For the standard stiffness matrix, the location of the integration points corresponds to $\alpha_K = \sqrt{\frac{1}{3}}$. In this case, coefficients a_4 and a_6 in Eq. (2.43) are

$$a_4(\gamma = \frac{3-\tau^2}{2}, \alpha_K = \sqrt{\frac{1}{3}}) = \frac{1}{24} \sin^2(2\Theta),$$

$$a_6(\gamma = \frac{3-\tau^2}{2}, \alpha_K = \sqrt{\frac{1}{3}}) = \frac{30 - 45\tau^2 + 8\tau^4 + (2 + 5\tau^2) \cos(4\Theta)}{2880}. \quad (2.45)$$

As can be seen, for the standard stiffness matrix, the coefficient a_4 in Eq. (2.45) is independent of the Courant number τ and equals zero at the angles $\Theta = 0, \frac{\pi}{2}, \pi, \frac{3\pi}{2}$ in the range $0 \leq \Theta \leq 2\pi$ (for all other angles the coefficient $a_4 \neq 0$); see Fig. 2.5.

Figure 2.4: Coefficient a_6 in Eq. (2.44) as a function of Θ and τ .Figure 2.5: Coefficient a_4 in Eq. (2.45) as a function of Θ .

For example, at $\Theta = 0, \frac{\pi}{2}, \pi, \frac{3\pi}{2}$, the coefficient a_4 is zero and the absolute value of the coefficient a_6 in Eq. (2.45) has the minimum value at $\tau = \tau^{st}$. Therefore, in the case of the averaged mass matrix and the standard stiffness matrix, time increments close to the stability limit can be recommended for the decrease in the dispersion error. It can be checked that the stability limit in this case corresponds to $\tau^{st} = 1$; i.e., $\gamma = \frac{3-\tau^2}{2} = 1$ at $\tau = \tau^{st} = 1$ and according to Eq. (2.8), this case reduces to the

standard approach with the lumped mass matrix and the time increments equal to the stability limit.

It is also necessary to note that the weighting coefficient $\gamma = 1.5$ was used in the average mass technique suggested in [58]. However, as can be seen from Eq. (2.43), $\gamma = 1.5$ does not lead to the decrease in the order of the dispersion error at finite time increments even in the 1-D case (i.e., the coefficient a_4 is non-zero); see also the numerical example below. Only for very small time increments $\Delta t \approx 0$ (or $\tau \approx 0$), the weighting coefficient derived above from Eq. (2.43) is $\gamma = \frac{3-\tau^2}{2} \approx 1.5$.

2.4.3 The standard approach with the lumped mass matrix

For the standard approach with the lumped mass matrix ($\gamma = 1$) and the standard stiffness matrix ($\alpha_K = \sqrt{\frac{1}{3}}$), the dispersion error can be also analyzed with the help of Eq. (2.43). The coefficient a_4 in this case is

$$a_4(\gamma = 1, \alpha_K = \sqrt{\frac{1}{3}}) = \frac{1}{48}(-4\tau^2 - \cos(4\Theta) + 5) \quad (2.46)$$

According to Eq. (2.46), the coefficient a_4 has the minimum value at $\tau = \tau^{st} = 1$ for all angles Θ ; see Fig. 2.6 (as we mentioned in previous Section 2.2.2, the stability limit is $\tau^{st} = 1$ for the standard approach). That is, $a_4(\gamma = 1, \alpha_K = \sqrt{\frac{1}{3}}) = \frac{1}{24} \sin^2(2\Theta)$ at $\tau = \tau^{st} = 1$. The dispersion error in the 1-D case for all approaches considered above coincides with that from the formulas for the 2-D case at $\Theta = 0$. It can be shown that all coefficients in a Taylor series of $R(c = c_o)$ are zero in the 1-D case at $\tau = \tau^{st} = 1$; i.e., in this case the dispersion error is zero. In contrast to the 1-D case, the dispersion error in the 2-D case for $\tau = \tau^{st} = 1$ is zero only for the wave propagating along the Cartesian axes ($\Theta = 0, \frac{\pi}{2}$) and has the maximum value for the wave propagating along the directions at which $\sin^2(2\Theta) = 1$ (or at $\Theta = \frac{\pi n}{4}$ where $n = 1, 3, 5, \dots$); see also Fig. 2.5. In this case the coefficient a_4 is $a_4 = \frac{1}{24}$ at $\Theta = \frac{\pi n}{4}$ and $\tau = \tau^{st} = 1$. It is interesting to note that for the same dispersion error in the 1-D case ($\Theta = 0$), the Courant number should be $\tau \approx 0.71$; i.e., $a_4(\gamma = 1, \alpha_K = \sqrt{\frac{1}{3}}) \approx \frac{1}{24}$

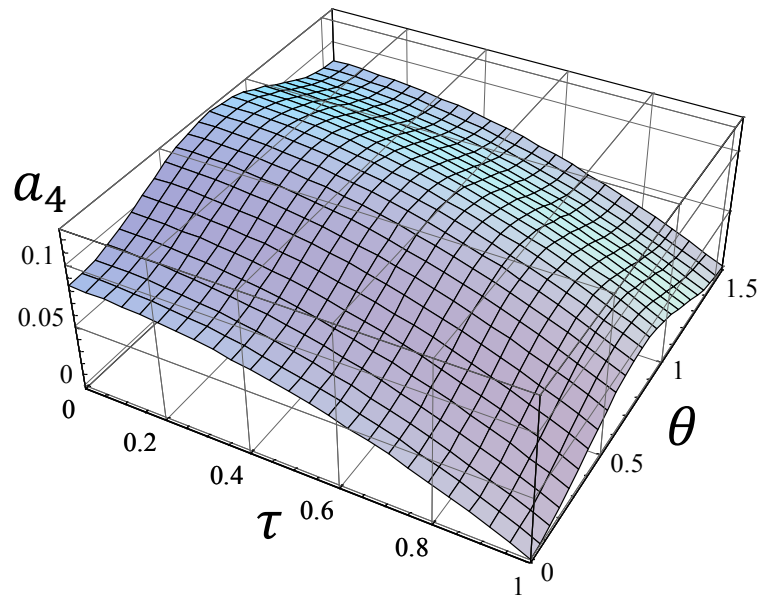


Figure 2.6: Coefficient a_4 in Eq. (2.46) as a function of Θ and τ .

at $\Theta = 0$ and $\tau \approx 0.71$. This $\tau \approx 0.71$ we will use for the determination of coefficients a_1 and a_2 in Eqs. (3.1)-(3.3) used for the standard approach at the filtering stage ; see Section 3.1.

Chapter III

The two-stage time-integration technique with filtering spurious oscillations

One of the main issues is the presence of spurious high-frequency oscillations in numerical solutions for transient elastodynamics and acoustic problems that makes numerical results very inaccurate. Despite a large number of publications related to the treatment of spurious oscillations, this issue has not been resolved in the literature. We would like to mention few recent papers [19, 24, 70, 80] dealing with the reduction of spurious oscillations for elastodynamics problems for the linear and quadratic finite elements. However, even for the standard low-order finite elements, the techniques in [19, 24, 70, 80] cannot remove all spurious oscillations and may yield inaccurate results at long-term integration. We should mention that it is difficult to predict and estimate the amplitudes of the spurious oscillations which are excited by the initial and boundary conditions and which depend also on the observation time (e.g., for the same space mesh, the amplitudes of spurious oscillations can become much larger with the increase in the observation time; see Section IV below). For example, due to the spurious oscillations we have not seen in the literature the accurate numerical solutions of elastodynamics problems at impact loading (or high-frequency loading) for the spectral and isogeometric elements as well as for the standard high-order finite elements. We will resolve this issue by the application of the two-stage time-integration approach recently developed in the papers; e.g., see [45, 47, 50] and will show that this approach can be effectively used with any space-discretization method.

In order to filter spurious high-frequency oscillations, numerical dissipation (or artificial damping) is usually introduced in existing approaches for the time integration of Eq. (1.5). As we showed in the paper [47], the use of a time-integration method with numerical dissipation (or artificial damping) at each time increment leads to inaccurate numerical results for low frequencies as well, especially for a long-

term integration. It is also unclear in this case how to select the amount of numerical dissipation and to determine the range of spurious high-frequencies to be filtered. To resolve these issues, Dr. Idesman developed the two-stage time-integration technique (see [45, 47, 50]) with the stage of basic computations and the filtering stage. This technique is based on the fact that for linear elastodynamics problems, there is no necessity to filter spurious oscillations at each time increment because the errors in high-frequencies do not affect the accuracy of low-frequencies during time integration; see [47]. In the basic computations, we can use the implicit trapezoidal rule or the standard explicit central-difference time-integration method (without numerical dissipation or artificial viscosity) in order to obtain an accurate solution of the semi-discrete elastodynamics problem, Eq. (1.5). Note this solution will contain spurious high-frequency oscillations. We should mention that other known implicit and explicit time-integration methods can be also used in basic computations.

3.1 Quantification of spurious oscillations and selection of amount of numerical dissipation (in terms of time increments) for their filtering

For the filtering of spurious oscillations, the implicit time-continuous Galerkin (TCG) method with large numerical dissipation developed in [47] is used at the filtering stage with $N = 10$ uniform time increments (5 positive plus 5 negative time increments). This means that there is no real time integration at the filtering stage (the sum of 10 time increments used at the filtering stage is zero). As shown in [47], this time integration is equivalent to the multiplication of each velocity and displacement of the uncoupled system of the semi-discrete equations by a factor of $\left(\frac{(3+m)^2+\Omega^2}{(3+m)^2+(2+m)^2\Omega^2}\right)^5$ (where $\Omega = \omega_j\Delta t$ and ω_j are the eigen-frequencies of the semi-discrete system, Δt is the time increment as well as $m = 15$ is used) and does not require the modal decomposition and the calculation of eigen-frequencies. As can be seen, this factor

is close to zero for large Ω and is close to unity for small Ω . The size Δt of time increments at the filtering stage indirectly defines the amount of numerical dissipation and the range of spurious oscillations and is calculated according to the following formulas (for uniform meshes).

$$\Delta t = \alpha \left(\frac{c_o T}{dx} \right) \frac{dx \Omega_{0.1}(N)}{c_o}, \quad (3.1)$$

with

$$\alpha \left(\frac{c_o T}{dx} \right) = a_1 \left(\frac{c_o T}{dx} \right)^{a_2} \quad (3.2)$$

in the 1-D case and

$$\begin{aligned} \Delta t &= \max_{m,j} \left[\alpha \left(\frac{c_m T}{dx_j} \right) \frac{dx_j}{c_m} \right] \Omega_{0.1}(N) = \max_{m,j} \left[\frac{dx_j}{c_m} \right]^{1-a_2} a_1 T^{a_2} \Omega_{0.1}(N) \\ &= \left[\frac{\max_j dx_j}{\min_m c_m} \right]^{1-a_2} a_1 T^{a_2} \Omega_{0.1}(N) = \left[\frac{dx_{\max}}{c_2} \right]^{1-a_2} a_1 T^{a_2} \Omega_{0.1}(N), \end{aligned} \quad (3.3)$$

in the 2-D and 3-D cases (see the papers [47, 50]).

Here, $c_o = \sqrt{\frac{E}{\rho}}$ is the wave velocity; $dx = \frac{L}{n_{dof}-1}$ is the size of an element in the 1-D case (L is the length of the bar and n_{dof} is the number of dof for a uniform mesh); T is the observation time; $\Omega_{0.1}(N = 10) = 0.81$ for the TCG method with $N = 10$ time increments. Using the calibration procedure described in [50], Table 1 shows the coefficients a_1 and a_2 for different implicit (non-diagonal matrix) and explicit (diagonal matrix) space-discretization methods. These coefficients are calibrated in the 1-D case for the filtering of numerical results obtained in basic computations with very small time increments. We should mention that the filtering stage can be applied in the beginning of calculations as a pre-processor, in the end of calculations as a post-processor or at some intermediate times (see [42, 43, 44, 47] for numerous 1-D, 2-D and 3-D examples of the application of the two-stage time-integration technique.)

Table 1. Coefficients a_1 and a_2 for different space-discretization techniques

Types of Elements	Coefficients						
		1 st	2 nd	3 rd	4 th	5 th	10 th
Standard Finite Elements (Consistent mass matrix)	a_1	0.3574	0.3156	0.4485	0.5495	0.5115	
	a_2	0.3204	0.2364	0.1571	0.1111	0.1078	
Spectral Elements (Lumped mass matrix)	a_1	0.3342	0.448	0.5659	0.4790	0.4461	0.4317
	a_2	0.3363	0.1845	0.1139	0.1128	0.1073	0.0759
Isogeometric Elements (Consistent mass matrix)	a_1			0.2513	0.2311		
	a_2			0.2035	0.1508		
Linear Elements with Reduced Dispersion (Non-diagonal matrix)	a_1	0.2979					
	a_2	0.2074					
Linear Elements with Reduced Dispersion (Diagonal matrix)	a_1	0.3296					
	a_2	0.2180					

3.2 The implicit TCG method for the filtering stage

The method is based on the linear approximations of displacements $\mathbf{U}(t)$ and velocities $\mathbf{V}(t)$ within a time step Δt ($0 \leq t \leq \Delta t$) (see [47]):

$$\mathbf{U}(t) = \mathbf{U}_0 + \mathbf{U}_1 t, \quad \mathbf{V}(t) = \mathbf{V}_0 + \mathbf{V}_1 t, \quad (3.4)$$

and has the first order of accuracy. Here \mathbf{U}_0 and \mathbf{V}_0 are the known initial nodal displacements and velocities, and the unknown nodal vector \mathbf{V}_1 can be expressed in terms of the unknown nodal vector \mathbf{U}_1 as follows:

$$\mathbf{V}_1 = \frac{1}{a_1} \mathbf{U}_1 - \frac{1}{a_1} \mathbf{V}_0. \quad (3.5)$$

Finally, the following system of algebraic equations is solved in order to determine \mathbf{U}_1 :

$$(\mathbf{M} + a_1^2 \mathbf{K}) \mathbf{U}_1 = -a_1 \mathbf{K} \mathbf{U}_0 + \mathbf{M} \mathbf{V}_0 + \mathbf{R}_1, \quad (3.6)$$

$$a_1 = \frac{m+2}{m+3} \Delta t,$$

$$\mathbf{R}_1 = \frac{(m+2)^2}{(m+3)\Delta t^{m+1}} \int_0^{\Delta t} \mathbf{R}(t) t^{m+1} dt. \quad (3.7)$$

After the calculation of \mathbf{U}_1 from Eq. (3.6), vectors $\mathbf{U}(\Delta t)$ and $\mathbf{V}(\Delta t)$ at the end of a time increment Δt are calculated using Eqs. (3.4) and (3.5) for $t = \Delta t$:

$$\mathbf{U}(\Delta t) = \mathbf{U}_0 + \mathbf{U}_1 \Delta t, \quad \mathbf{V}(\Delta t) = \mathbf{V}_0 + \mathbf{V}_1 \Delta t. \quad (3.8)$$

The parameter m (see Eq. (3.7)) is responsible for the amount of numerical dissipation and is taken $m = 15$, see [47].

Chapter IV

Numerical modeling

The new finite element techniques with reduced dispersion and explicit time-integration methods are implemented into the finite element code FEAP [97]. Below they are applied to 1-D, 2-D and 3-D impact linear transient elastodynamics and acoustic problems for which all low and high frequencies are excited. Due to spurious high-frequency oscillations, these problems cannot be accurately solved by existing time-integration methods based on the introduction of artificial viscosity (or numerical dissipation) at each time increment, especially in the case of long-term integration. Therefore, the two-stage time integration technique developed in the papers [50, 44, 47] is used (see also Chapter III). The filtering stage of this technique includes the TCG method with $N = 10$ time increments (5 positive plus 5 negative time increments) the size of which is calculated according to Eqs. (3.1) - (3.3). We also compare the numerical results obtained below with those obtained in the paper [43] using the implicit trapezoidal rule with very small time increments at basic computations. Sections 4.1, 4.2, 4.2 are the impact of an elastic bar against a rigid wall for 1-D, 2-D, and 3-D cases, respectively. In Section 4.4 we solve a 2-D transient acoustic problems and show the findings ‘are also valid in the multidimensional case.

4.1 1D impact of an elastic bar against a rigid wall

First, the impact of an elastic bar of the length $L = 4$ and the cross section $A = 1$ against a rigid wall is considered in the 1-D case (see Fig. 4.1a). Young’s modulus is chosen to be $E = 1$ and the density to be $\rho = 1$. The following boundary conditions are applied: the displacement $u(0, t) = t$ (which corresponds to the velocity $v(0, t) = v_0 = 1$) and $u(4, t) = 0$ (which corresponds to the velocity $v(4, t) = 0$). Initial displacements and velocities are zero; i.e., $u(x, 0) = v(x, 0) = 0$. The analytical

solution to this problem includes the continuous variation of displacements $u_a(x, t) = t - x$ for $t \geq x$ and $u_a(x, t) = 0$ for $t \leq x$, and the piecewise continuous variation of velocities and stresses $v_a(x, t) = -\sigma^a(x, t) = 1$ for $t \geq x$ and $v_a(x, t) = \sigma^a(x, t) = 0$ for $t \leq x$ (at the interface $x = t$, jumps in stresses and velocities occur).

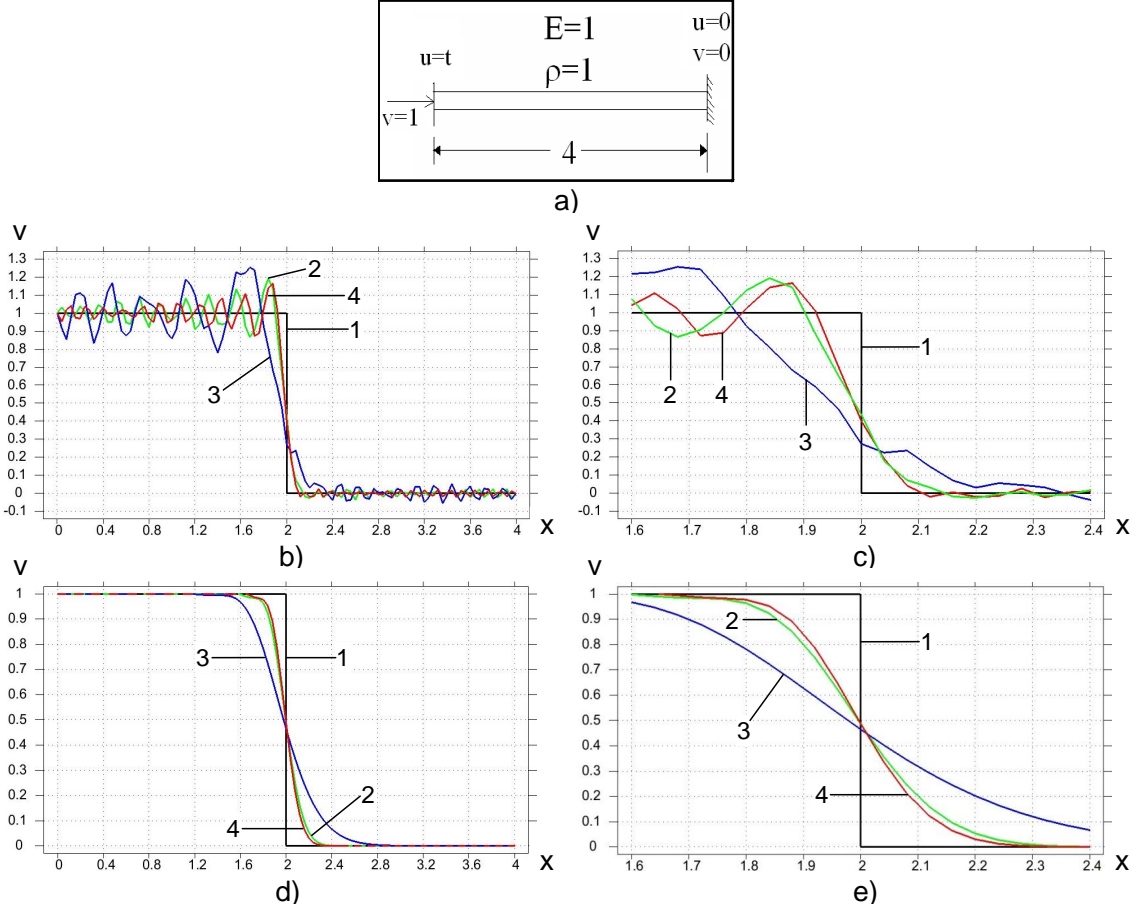


Figure 4.1: Impact of an elastic bar of length $L = 4$ against a rigid wall (a). The velocity distribution along the bar at observation time $T = 18$ after basic computations with small time increments $\Delta t = \Delta t^{st}/20 = 0.002$ (b, c) and after post-processing (d, e). Curves 1 correspond to the analytical solution. Curves 2 and 3 correspond to the numerical solutions with the averaged ($\gamma = \frac{3-\tau^2}{2}$) and lumped mass matrices on a uniform mesh with 100 linear 2-node finite elements. Curves 4 correspond to the numerical solutions from the paper [47]) for the averaged mass matrix ($\gamma = 0.5$) and the implicit time-integration method on a uniform mesh with 100 linear 2-node finite elements. c) and e) show the zoomed graphs b) and d) in the range $1.6 < x < 2.4$.

For time $4 \leq t \leq 8$ the solution is similar to that for $0 \leq t \leq 4$ with the

difference that the elastic wave reflect from the right end and propagate to the left. For time $8 \leq t \leq 12$ the solution is the same as for time $0 \leq t \leq 4$ and so on. The observation time is chosen to be $T = 18$. During this time the velocity pulse travels within the bar with two reflections from each end of the bar.

It is known that the application of traditional semi-discrete methods to this problem leads to oscillations in velocities and stresses due to the spurious high-frequency response [45, 41, 47]. As we will see (e.g., from Fig. 4.1b,c), finite elements with reduced numerical dispersion reduce these oscillations after basic computations but they do not completely remove them from the numerical solution. Therefore, the two-stage procedure with the filtering stage as described in the Chapter III will be applied for accurate and non-oscillatory solutions. The 1-D impact problem with propagating discontinuities in stresses and velocities can be considered a good benchmark problem for the testing of new numerical methods for wave propagation problems.

The problem is solved on uniform meshes with 100 and 300 linear two-node finite elements with the lumped and averaged ($\gamma = \frac{3-\tau^2}{2}$) mass matrices using the standard explicit central difference method in time based on Eq. (2.3) (for the lumped mass matrix $\mathbf{M} = \mathbf{D}$, Eq. (2.3) reduces to the standard form of the explicit central difference method). We will consider very small time increments $\Delta t = t^{st}/20$ (much smaller than the stability limit Δt^{st} ; e.g., $\Delta t^{st} = 0.04$ and $\Delta t^{st} = 0.013333$ for uniform meshes with 100 and 300 linear finite elements, respectively). Very small time increments for the 1-D problems are the worst case from the point of view of accuracy because at basic computations for the time increments equal to the stability limit, the numerical solutions on uniform meshes with linear elements coincide with the exact solution; see Section 2.1. We should also mention that the techniques based on the modified integration rule with $\alpha_M = \sqrt{\frac{4-\tau^2}{3}}$ and on the averaged mass matrix with $\gamma = \frac{3-\tau^2}{2}$ are completely equivalent and yield the same results in the 1-D case; see Section 2.1.

Fig. 4.1 shows the numerical results for linear elements obtained with the lumped and averaged mass matrices after basic computations with very small time

increments $\Delta t = t^{st}/20$ and after the filtering stage (post-processing). The use of the formulation with the reduced dispersion error (see curve 2 in Fig. 4.1b,c) reduces the amplitudes of spurious oscillations and yields a more accurate slope of the wave front at $x = 2$ compared with those for the lumped mass matrix at the same numbers of elements (see curve 3 in Fig. 4.1b,c). However, the presence of spurious high-frequency oscillations makes it difficult to compare the numerical results. After the filtering of spurious oscillations, we can see that for the selected observation time and at the same accuracy, the use of the averaged mass matrix reduces the number of dof by a factor of three as compared with that for the standard lumped mass matrix (see curves 2 and 3 in Fig. 4.2).

We should mention that with the increase in the observation time, the difference in accuracy between the linear elements with reduced dispersion and the standard linear elements increases; i.e., the efficiency of the linear elements with reduced dispersion increases with the increase in the observation time (see curves 2 and 3 in Fig. 4.2c-f at the observation times $T = 18$ and $T = 194$). It is also interesting to note that the linear elements with reduced dispersion used with the implicit (as in the paper [43]) and explicit (as in the current study) time-integration methods with very small time increments yield similar results at the stage of basic computations and after the filtering stage; see curves 2 and 4 in Fig. 4.1 (curves 4 for the implicit method is slightly more accurate than curves 2 for the explicit method). The analysis of the dispersion error in the 1-D case for averaged mass matrix technique shows (see Chapter II and the paper [43]) that despite the same order of accuracy, the leading term for the dispersion error is slightly smaller for the implicit method than that for the explicit method.

In Fig. 4.3, we have also analyzed the numerical results for the averaged mass matrix with $\gamma = \frac{3}{2}$ (as suggested in [58]) and the explicit central difference method with time increments close to the stability limit at basic computations. As we can see, in this case the results after basic computations (curve 4 in Fig. 4.3a,b) are less accurate than those described by curve 2 in Fig. 4.3a,b. If we filter these results

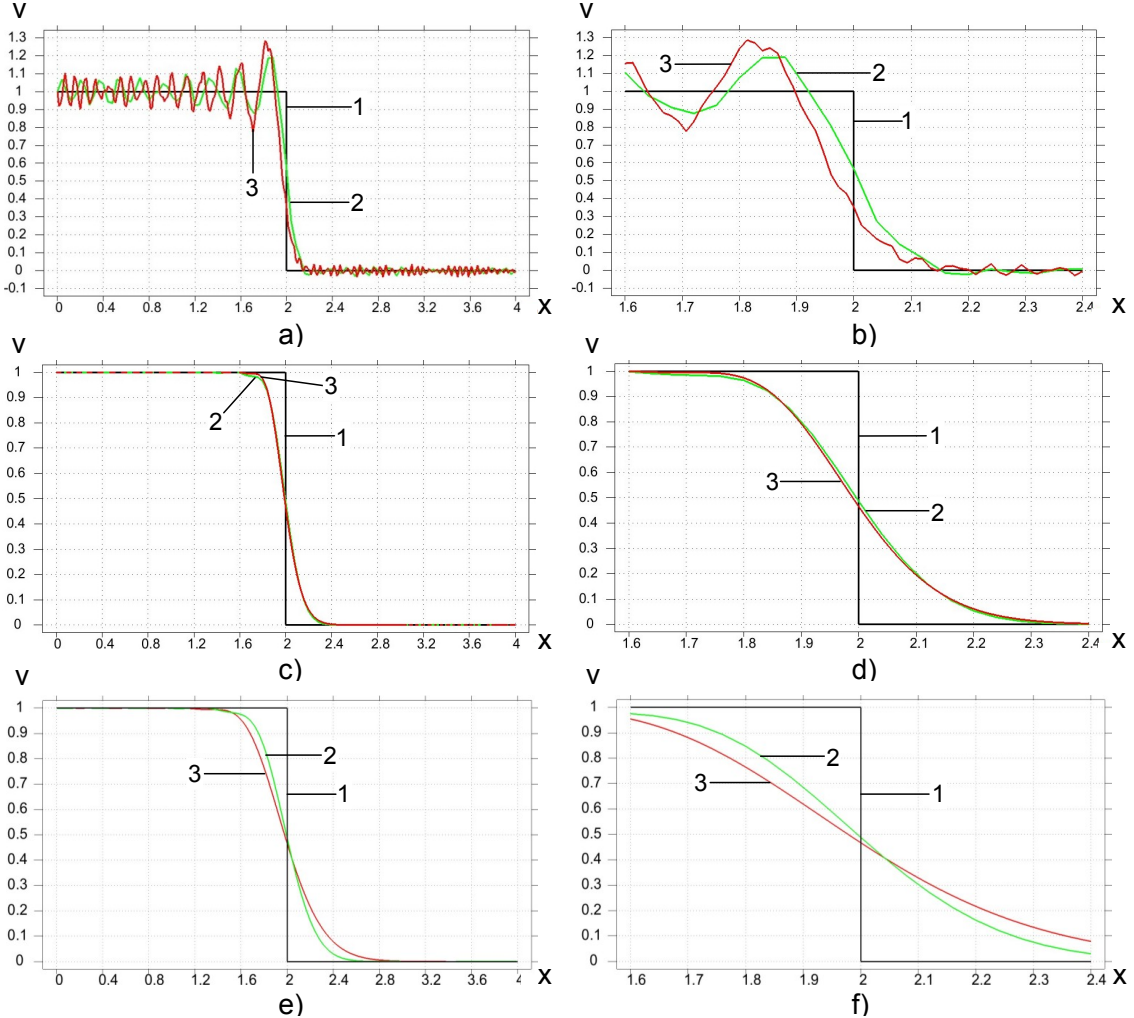


Figure 4.2: The velocity distribution along the bar at observation time $T = 18$ after basic computations with small time increments $\Delta t = \Delta t^{st}/20$ (a, b) and after post-processing (c, d). Curves 1 correspond to the analytical solution. Curves 2 correspond to the numerical solutions with the averaged ($\gamma = \frac{3-\tau^2}{2}$) mass matrix on a uniform mesh with 100 linear 2-node finite elements. Curves 3 correspond to the numerical solutions with the lumped mass matrix on a uniform mesh with 300 linear 2-node finite elements. b) and d) show the zoomed graphs a) and c) in the range $1.6 < x < 2.4$.

(curve 4 in Fig. 4.3a,b) with the amount of numerical dissipation (time increments) used for curve 2 in Fig. 4.3a,b, then spurious oscillations remain after the filtering stage (curve 4 in Fig. 4.3c,d). If we use a sufficient amount of numerical dissipation at the filtering stage then the results (curve 5 in Fig. 4.3c,d) are close to curve 3 in

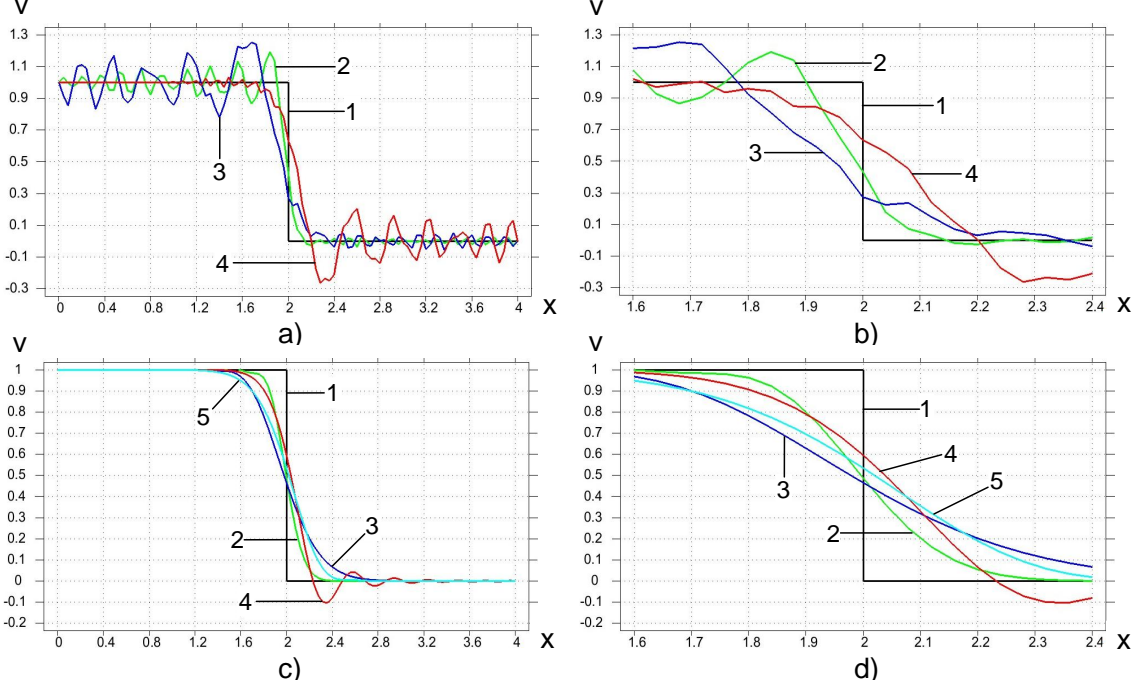


Figure 4.3: The velocity distribution along the bar at observation time $T = 18$ after basic computations (a, b) and after post-processing (c, d). A uniform mesh with 100 linear 2-node finite elements is used. Curves 1 correspond to the analytical solution. Curves 2 and 3 correspond to the numerical solutions with the averaged ($\gamma = \frac{3-\tau^2}{2}$) and lumped mass matrices (with small time increments $\Delta t = \Delta t^{st}/20$ in basic computations). Curves 4 correspond to the numerical solutions for the averaged ($\gamma = 1.5$) mass matrix and the time increments in basic computations close to the stability limit. b) and d) show the zoomed graphs a) and c) in the range $1.6 < x < 2.4$. Curves 4 and 5 in c) and d) differ by the amount of numerical dissipation used at the filtering stage; see the text.

Fig. 4.3c,d. This means that the approach suggested in [58]) for the averaged mass matrix does not improve the dispersion error and the accuracy of numerical results if relative large time increments (close to the stability limit) are used in calculations. However, at small time increments $\Delta t \approx 0$, parameter $\tau \approx 0$ is also small and $\gamma = \frac{3-\tau^2}{2} \approx \frac{3}{2}$; i.e., the results for $\gamma = \frac{3}{2}$ will coincide with curve 2 in Fig. 4.3 at small time increments in basic computations. It is also interesting to note that because the numerical solutions with the implicit (see the paper [43]) and explicit (as in the current study) time-integration methods for the linear elements with reduced dispersion are similar (see curves 2 and 4 in Fig. 4.1), then some conclusions from

the paper [43] are also applicable to the linear elements with reduced dispersion and explicit time-integration methods. E.g., after the filtering stage, the numerical results obtained with the averaged mass matrix $\gamma = \frac{3-\tau^2}{2}$ (or the modified integration rule with $\alpha_M = \sqrt{\frac{4-\tau^2}{3}}$) converge to the analytical solution at mesh refinement (similar to the results in [43]).

The linear elements with the reduced dispersion and the explicit time-integration methods are more accurate than the standard quadratic elements with the consistent mass matrix (similar to the results in [43]). Similar to the results in [43], the range of frequencies included in numerical solutions after the filtering stage is indirectly determined by the size of the time increments calculated by Eqs. (3.1) - (3.3) (see Chapter III). The numerical results show that if the time increments calculated according to Eqs. (3.1) - (3.3) for the filtering stage are close to each other for the formulations with the lumped, consistent or averaged mass matrices on different uniform meshes, then the numerical solutions obtained on these different uniform meshes are close to each other. This means that Eqs. (3.1) - (3.3) allow the quantitative estimation of the advantage of the averaged mass matrix ($\gamma = \frac{3-\tau^2}{2}$) compared with the standard approaches with the lumped and consistent mass matrices. For example, at the integration by the explicit central-difference method with very small time increments, for a uniform mesh with 100 linear finite elements and the averaged mass matrix ($\gamma = \frac{3-\tau^2}{2}$), the size of the time increments at the filtering stage is $\Delta t_1 = 0.04083$ according to Eqs. (3.1) - (3.2). For a uniform mesh with 300 linear finite elements and the lumped mass matrix, the size of the time increments at the filtering stage is $\Delta t_2 = 0.04075$ according to Eqs. (3.1) - (3.2). Because Δt_2 is close to Δt_1 , then curves 2 and 3 in Fig. 4.2c,d are close to each other; see also the analytical solution, curve 1.

4.2 2D impact of an elastic bar against a rigid wall

This problem is a more general plane strain formulation of the 1-D impact problem considered in Section 4.1; see Fig. 4.4a. In contrast to the 1-D impact problem, compressional and shear elastic waves propagate in the 2-D case. A bar of length

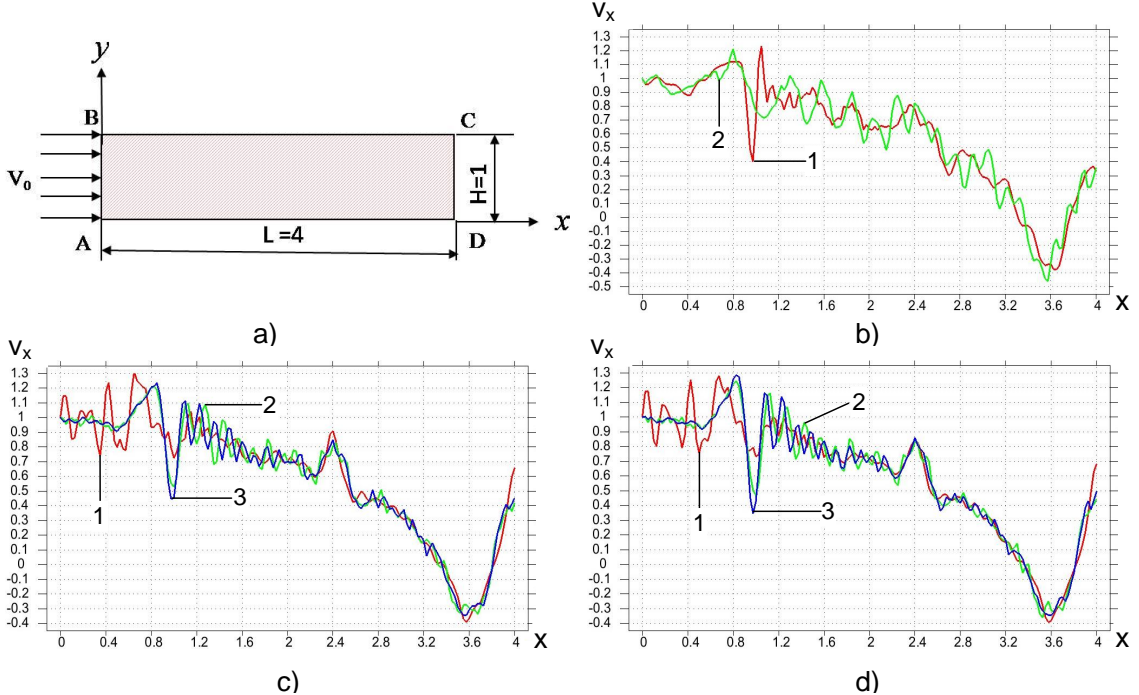


Figure 4.4: A 2-D plane strain impact problem (a). The axial velocity distribution along the axis of symmetry AD at observation time $T = 13$ for the Poisson's ratio $\nu = 0.3$. The results are shown after basic computations obtained by the explicit central difference method with the lumped mass matrix (b), with the modified integration rule (c), and with the averaged mass matrix (d). Curves 1 and 2 correspond to the numerical solutions obtained with the time increments Δt^{st} and $\Delta t^{st}/20$, respectively. Curves 3 correspond to the numerical solutions (from the paper [47]) obtained by the implicit time-integration method with the modified integration rule (c) and the averaged mass matrix (d). A uniform mesh with $40 \times 160 = 6400$ linear 4-node finite elements is used.

$L = 4$ and height $2H = 2$ is considered. Due to symmetry, the problem is solved for a half of the bar $ABCD$ where AD is the axis of symmetry. Young's modulus is chosen to be $E = 1$ and the density to be $\rho = 1$. Three cases of different Poisson's ratios $\nu = 0.1$, $\nu = 0.3$ and $\nu = 0.49$ are studied. The following boundary conditions

are applied: along boundary AB $u_n = t$ (it corresponds to velocity $v_n = v_0 = 1$) and $\tau_n = 0$; along boundaries BC and CD $\sigma_n = 0$ and $\tau_n = 0$; along boundary AD $u_n = 0$ and $\tau_n = 0$, where u_n , v_n , and σ_n are the normal displacements, velocities and the tractive forces, respectively; τ_n are the tangential tractive forces. Initial displacements and velocities are zero; i.e., $u(x, y, 0) = v(x, y, 0) = 0$. The observation time is chosen to be $T = 13$. During this time the velocity pulse travels within the bar with multiple reflections from the ends of the bar and from the external surface BC .

The problem is solved on uniform coarse and fine meshes with linear four-node quadrilateral finite elements with the modified integration rule for the mass and stiffness matrices ($\alpha_M = \sqrt{\frac{4-\tau^2}{3}}$ and $\alpha_K = \sqrt{\frac{4(2\nu-1)}{3(4\nu-3)}}$) and with the lumped and averaged ($\gamma = \frac{3-\tau^2}{2}$) mass matrices. In order to study the effect of time increments at basic calculations on the accuracy of numerical results, we will use time increments $\Delta t \approx \Delta t^{st}$ close to the stability limit Δt^{st} and smaller than the stability limit ($\Delta t = 0.5\Delta t^{st}$ and very small time increments $\Delta t = \Delta t^{st}/20$).

Figs. 4.4 - 4.8 show the distribution of the axial velocity along the axis of symmetry AD at observation time $T = 13$ for Poisson's ratio $\nu = 0.3$ after basic computations (Fig. 4.4) and for Poisson's ratios $\nu = 0.1$, $\nu = 0.3$ and $\nu = 0.49$ after the filtering stage (Figs. 4.9 - 4.8). Similar to the previous 1-D impact problem, the numerical results after basic computations with the lumped stiffness matrix and the formulations with reduced numerical dispersion contain spurious oscillations at very small time increments $\Delta t = \Delta t^{st}/20 = \frac{dx}{20c_1}$; see curves 2 in Fig. 4.4. However, in contrast to the 1-D impact problem, the spurious oscillations and the dispersion error at basic computations do not disappear at the time increments close to the stability limit; see curves 1 in Fig. 4.4. This is explained by the fact that we cannot zero the coefficients a_6 for the dispersion error simultaneously for the compressive ($c = c_1$) and shear ($c = c_2$) waves; see Section 2.2. It also can be seen from Fig. 4.4 (see curves 1 and 2) that the results after basic computation for the time increments close to the stability limit and for very small time increments are different for all methods. We should also note that at very small time increments, the numerical solutions for the

linear elements with reduced dispersion obtained with the explicit central difference method (curves 2 in Fig. 4.4c,d) and with the implicit trapezoidal rule (see the paper [43] as well as curves 3 in Fig. 4.4c,d) are close to each other. However, it is difficult to compare the accuracy of different approaches after basic computations due to large spurious oscillations.

After filtering spurious oscillations at the filtering stage, the solutions at basic computations obtained by the explicit central difference method at very small time increments $\Delta t^{st}/20$ with the modified integration rule (curves 3 in Fig. 4.5) and with the averaged mass matrix (curves 4 in Fig. 4.5) are close to each other. The results in Fig. 4.5 show that despite the impact along the x -axis elastic wave propagate in all directions and the magnitudes of the transverse velocity v_y are comparable with those for the axial velocity v_x ; i.e., a general case of propagation of elastic wave occurs for the considered problem. As can be seen from Fig. 4.5, after the filtering stage the results obtained by the explicit central difference method at very small time increments $\Delta t^{st}/20$ and the lumped mass matrix (curves 1) are much less accurate than those obtained with the elements with reduced dispersion (curves 3 and 4). The results obtained by the standard time integration on a fine mesh with $120 \times 480 = 57600$ linear elements (curves 2 in Fig. 4.5) show that at the selected observation time, the elements with reduced dispersion reduce the number of dof by a factor of 9 compared with those for the standard approach at the same accuracy (compare curves 3 or 4 for a mesh with $40 \times 160 = 6400$ linear elements and curves 2 for a mesh with $120 \times 480 = 57600$ linear elements in Fig. 4.5).

Similar to the 1-D case in Section 4.1 and the results reported in the paper [43] for implicit time-integration methods, the size of the time increments calculated by Eqs. (3.1) - (3.3) for the filtering stage allows the quantitative estimation of the advantage of the modified integration rule (or the averaged mass matrix) technique compared with the standard lumped mass matrix. For example, for a uniform mesh with $40 \times 160 = 6400$ linear finite elements and the modified integration rule (or the averaged mass matrix), the size of the time increments at the filtering stage is $\Delta t_1 =$

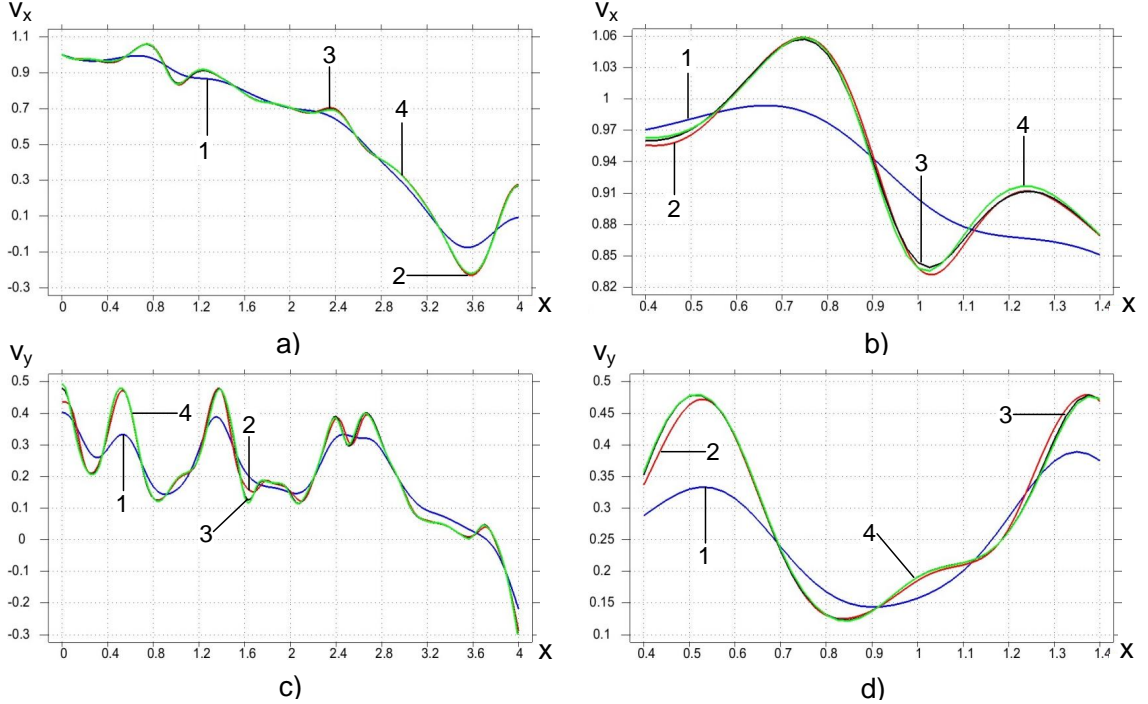


Figure 4.5: The axial velocity distribution v_x along the axis of symmetry AD (a, b) and the transverse velocity distribution v_y along the external surface BC (c, d) at observation time $T = 13$ for the Poisson's ratio $\nu = 0.3$. The results are shown after the filtering of the solutions at basic computations obtained by the explicit central difference method with the lumped mass matrix (curves 1 and 2), with the modified integration rule (curve 3), and with the averaged mass matrix (curve 4). Small time increments $\Delta t^{st}/20$ are used at basic computations (see Fig. 4.4). Uniform meshes with $40 \times 160 = 6400$ (curves 1, 3 and 4) and $120 \times 480 = 57600$ (curve 2) linear elements are used. b) and d) show the zoomed graphs a) and c) in the range $0.4 < x < 1.4$.

0.038204 according to Eqs. (3.1) - (3.3). For a uniform mesh with $120 \times 480 = 57600$ linear finite elements and the lumped mass matrix, the size of the time increments at the filtering stage is $\Delta t_2 = 0.036717$ according to Eqs. (3.1) - (3.3). Because Δt_2 is close to Δt_1 , then curves 2 and 3 (or 4) in Fig. 4.5 are close to each other. We should also mention that with the increase in the observation time, the effectiveness of the elements with reduced dispersion increases compared with that for the standard approach; i.e., according to Eqs. (3.1) - (3.3), for the same accuracy of numerical results, the ratio $\frac{N_{FE}^{lump}}{N_{FE}^{red}}$ is an increasing function of the observation time (N_{FE}^{lump} and

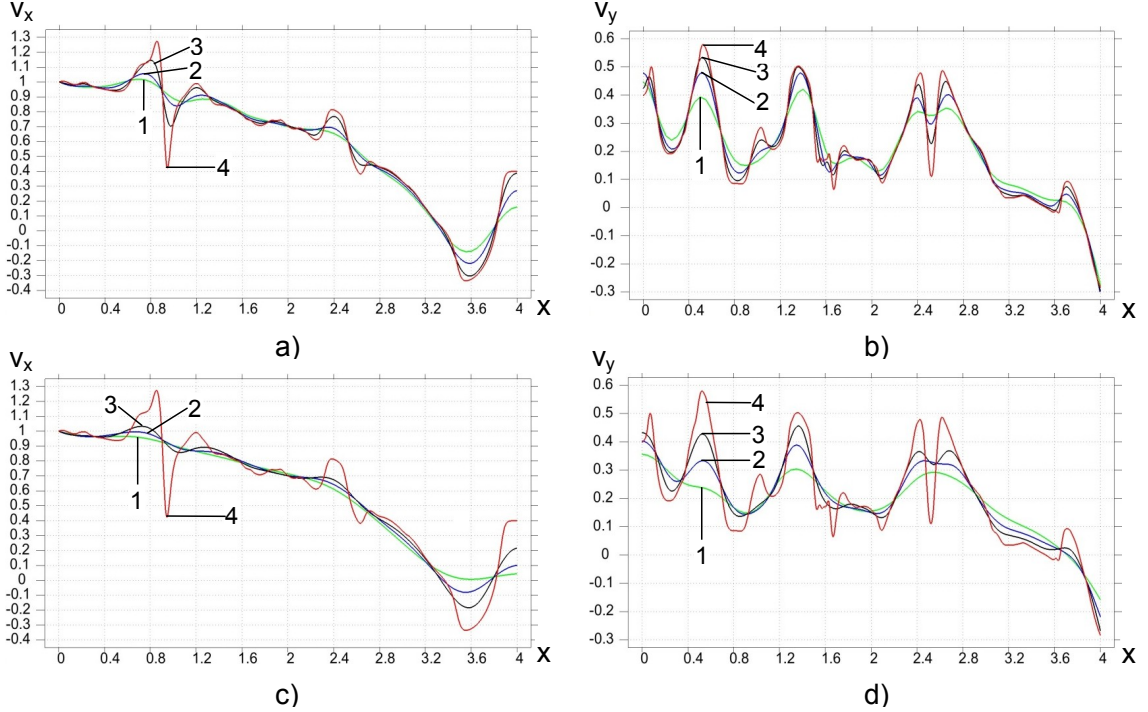


Figure 4.6: The axial velocity distribution v_x along the axis of symmetry AD (a, c) and the transverse velocity distribution v_y along the external surface BC (b, d) at observation time $T = 13$ for the Poisson's ratio $\nu = 0.3$. The results are shown after the filtering of the solutions at basic computations obtained by the explicit central difference method with the modified integration rule (a, b) and with the standard approach (curves 1-3 in (c, d)). Small time increments $\Delta t^{st}/20$ are used at basic computations. Curves 1, 2, 3, 4 correspond to uniform meshes with $20 \times 80 = 1600$, $40 \times 160 = 6400$, $80 \times 320 = 25600$, and $320 \times 1280 = 409600$ linear elements. Curves 4 in (a, b, c, d) correspond to the modified integration rule and are considered as a reference solution.

N_{FE}^{red} are the numbers of finite elements used with the standard formulation and with the formulations with reduced dispersion).

The convergence of the numerical results at mesh refinement obtained by the linear elements with the modified integration rule technique and by the standard approach is shown in Fig. 4.6 (the results are presented after the filtering stage). Uniform meshes with $20 \times 80 = 1600$, $40 \times 160 = 6400$, $80 \times 320 = 25600$, and $320 \times 1280 = 409600$ linear elements are used. Fig. 4.6 shows that for any mesh, the modified integration rule technique yields much more accurate solutions than the

standard approach. We do not include the results for the average mass matrix technique because they are very close to those for the modified integration rule technique in Fig. 4.6 (a,b).

In order to quantify the analysis of convergence for different techniques, we introduce the following error in velocity:

$$e = \sqrt{\sum_{k=1}^m [v_x(k) - v_x^{ref}(k)]^2 + [v_y(k) - v_y^{ref}(k)]^2}, \quad (4.1)$$

where $v_x(k)$ and $v_y(k)$ are the x - and y -components of the nodal velocity at node k , superscript “*ref*” designates the reference solution, $m = 1701$ is the total number of nodes of the coarse mesh with $20 \times 80 = 1600$ elements. In order to simplify the calculation of the error in Eq. (4.1) for different meshes, we use only nodes that are common for all meshes and correspond to the nodes of the coarse mesh with $20 \times 80 = 1600$ elements. Because for the 2-D impact problem we do not have the analytical solution then the numerical results obtained on the finest mesh with the $320 \times 1280 = 409600$ linear elements with reduced dispersion are used as a reference solution in Eq. (4.1). Fig. 4.7 shows the error e versus the number of dof n for the standard linear elements (curve 1) and the linear elements with reduced dispersion (curves 2 and 3) using the logarithmic scale. It can be seen from Fig. 4.7 that the dispersion reduction techniques based on the modified integration rule and on the averaged mass matrix yield approximately the same results for elastodynamics problems (curves 2 and 3 in Fig. 4.7 practically coincide). We can also see that these techniques significantly reduce the number of dof compared with the standard linear finite elements at the same accuracy; e.g., at accuracy $\log e \approx 0.6$ this reduction is approximately equal to a factor of 9 (see curves 1 and 2 at $\log e \approx 0.6$).

Figs. 4.8 and 4.9 show the effect of the size of time increments on the accuracy of the results with the new formulations for different Poisson’s ratios. As can be seen, the results at very small time increments $\Delta t^{st}/20$ (curves 4) are more accurate than

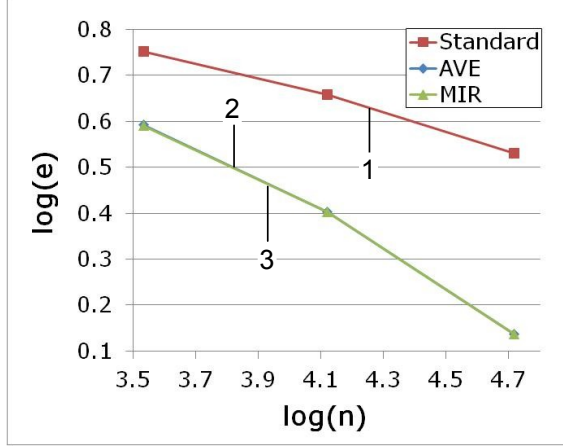


Figure 4.7: The error in velocity e versus the number of dof for standard approach (curve 1), for the modified integration rule technique (curve 2) and for the averaged mass matrix technique (curve 3). The logarithmic scale is used. Curve 2 and 3 practically coincide.

those at time increments close the stability limit Δt^{st} (curves 2); see also the reference solution (curves 1) from the paper [47] obtained by the implicit time-integration method with the modified integration rule on a fine mesh with $300 \times 1200 = 360000$ linear finite elements (the modified integration rule on a fine mesh with $320 \times 1280 = 409600$ linear finite elements and explicit time integration yields approximately the same reference solution; e.g., see curve 4 in Fig. 4.6 and curve 1 in Fig. 4.9c). This means that in contrast to the standard approach with the explicit central difference method (for which time increments close to the stability limit yield more accurate results), very small time increments (much smaller than the stability limit) yield more accurate results for the formulations with reduced dispersion in the 2-D case (see also analysis in Section 2.2). It is also necessary to note that small time increments $0.5\Delta t^{st}$ (curves 3) and $\Delta t^{st}/20$ (curves 4) yield practically the same results for the formulations with the reduced dispersion; i.e., from the computational point of view, the time increments $0.5\Delta t^{st}$ can be recommended for these new formulations.

Figs. 4.9 and 4.8 also show that after the filtering stage, the difference between numerical results obtained with the modified integration rule and the averaged mass matrix is small at different Poisson's ratios. This difference is slightly larger at Pois-

son's ratio close to 0.5. But even in this case it can be neglected compared with the change in the numerical results at mesh refinement (see curves 1 in Figs. 4.9 and 4.8).

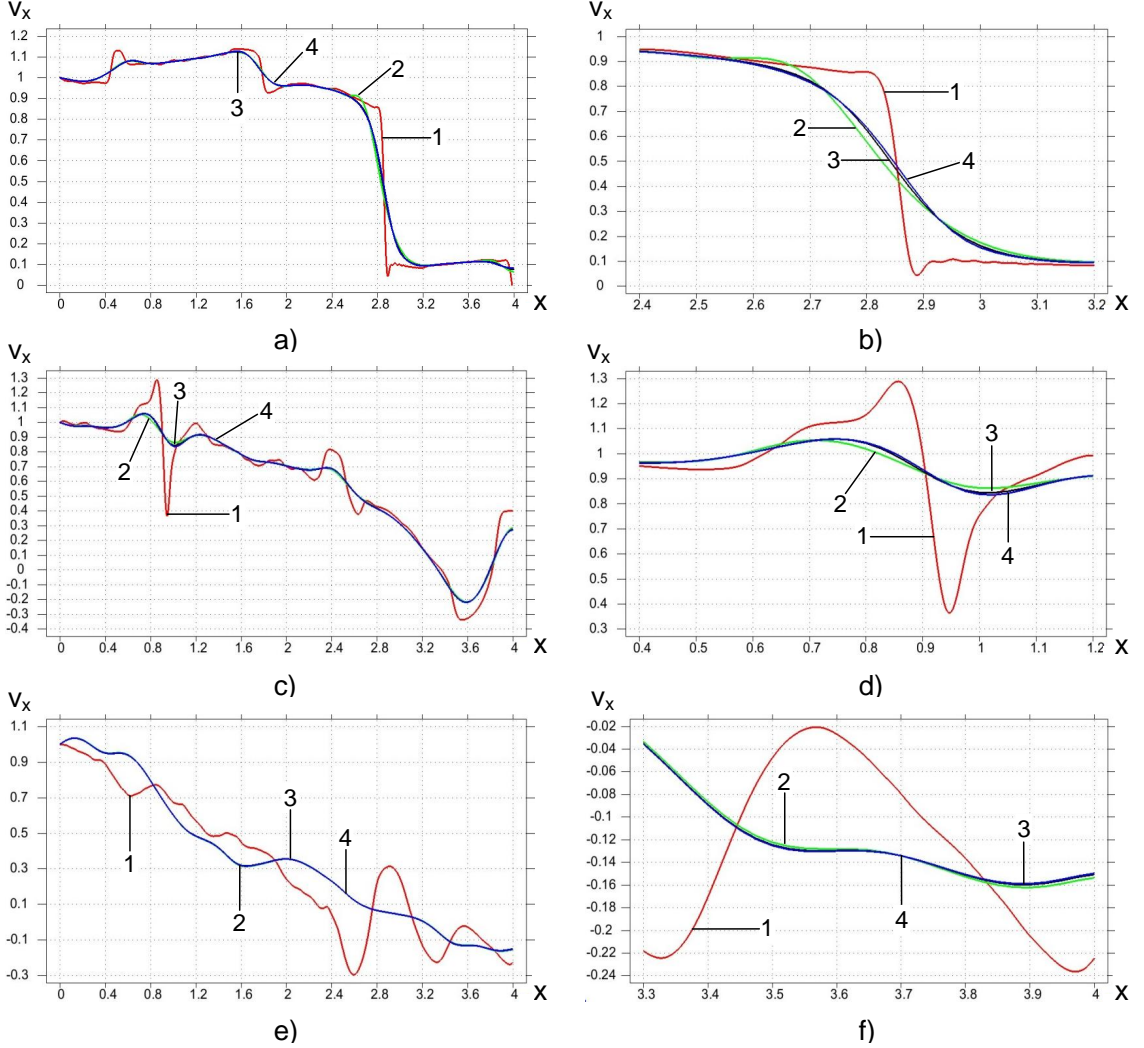


Figure 4.8: The axial velocity distribution along the axis of symmetry AD at observation time $T = 13$ for the Poisson's ratios $\nu = 0.1$ (a, b), $\nu = 0.3$ (c, d) and $\nu = 0.49$ (e, f). The results are shown after the filtering of the solutions at basic computations obtained by the explicit central difference method with the averaged mass matrix and the following time increments: Δt^{st} (curves 2), $0.5\Delta t^{st}$ (curves 3) and $\Delta t^{st}/20$ (curves 4). A uniform mesh with $40 \times 160 = 6400$ linear 4-node finite elements is used. Curves 1 are the reference solutions (from the paper [47]) obtained by the implicit time-integration method with the averaged mass matrix on a fine mesh with $300 \times 1200 = 360000$ linear finite element. b), d) and f) show the zoomed graph a), c) and e), respectively.

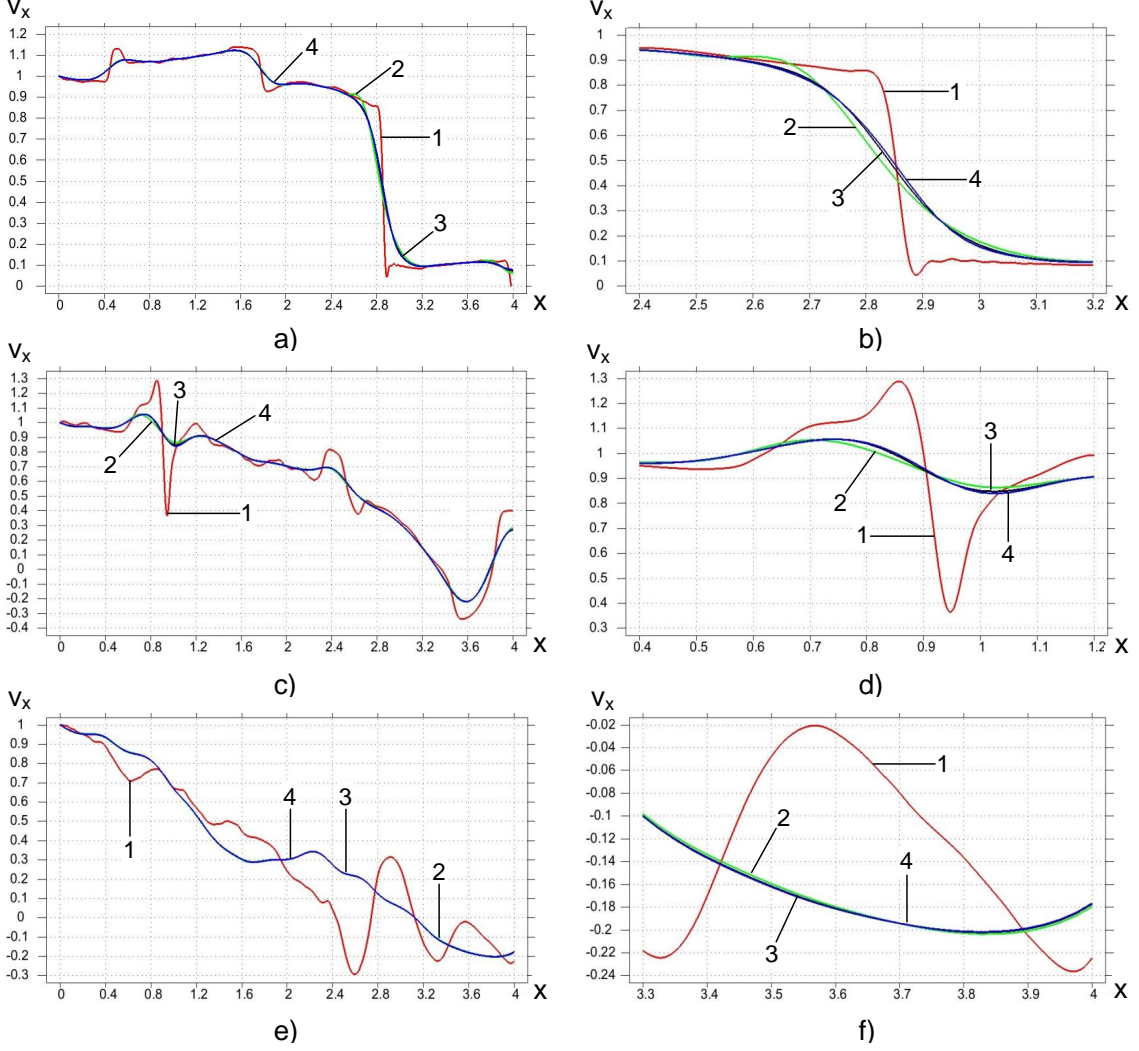


Figure 4.9: The axial velocity distribution along the axis of symmetry AD at observation time $T = 13$ for the Poisson's ratios $\nu = 0.1$ (a, b), $\nu = 0.3$ (c, d) and $\nu = 0.49$ (e, f). The results are shown after the filtering of the solutions at basic computations obtained by the explicit central difference method with the modified integration rule and the following time increments: Δt^{st} (curves 2), $0.5\Delta t^{st}$ (curves 3) and $\Delta t^{st}/20$ (curves 4). A uniform mesh with $40 \times 160 = 6400$ linear 4-node finite elements is used. Curves 1 are the reference solutions (from the paper [47]) obtained by the implicit time-integration method with the modified integration rule on a fine mesh with $300 \times 1200 = 360000$ linear finite element. b), d), and f) show the zoomed graph a), c), and e), respectively.

4.3 3D impact of an elastic bar against a rigid wall

A solid 3-D bar of length $L = 2$ with a square cross section $a \times a$ ($a = 2$) under impact loading at the left end $ACEM$ is considered; see Fig. 4.10. Due to symmetry,

the problem is solved for a quarter of the bar $ACEMNFDB$ where planes $ABDC$ and $ABNM$ are the planes of symmetry. Young's modulus is chosen to be $E = 1$, Poisson's ratio to be $\nu = 0.3$, and the density to be $\rho = 1$. The following boundary conditions are applied: along the left end $ACEM$: $u_n = t$ (which corresponds to the instantaneous application of velocity $v_{load}(t) = v_0 = 1$) and $\tau_n = 0$; along planes $BDFN$, $CDFE$ and $EFNM$: $\sigma_n = 0$ and $\tau_n = 0$ (free surfaces); along planes $ABDC$, $ABNM$: $u_n = 0$ and $\tau_n = 0$ where u_n , v_n , and σ_n are the normal displacements, velocities and the tractive forces, respectively; τ_n are the tangential tractive forces.

The observation time is chosen to be $T = 7$. During this time the velocity pulse travels within the bar with multiple reflections from the ends of the bar and from the external surfaces $CDFE$ and $EFNM$. The problem is solved by the explicit central-difference method on uniform meshes with $20 \times 20 \times 40 = 16000$ linear eight-node quadrilateral elements with the modified integration rule for the mass and stiffness matrices ($\alpha_M = \sqrt{\frac{4-\tau^2}{3}}$ and $\alpha_K = \sqrt{\frac{4(2\nu-1)}{3(4\nu-3)}}$) as well as with the lumped and averaged ($\gamma = \frac{3-\tau^2}{2}$) mass matrices. The numerical results in Figs. 4.11 - 4.14 show the distribution of the axial velocity V_z along lines EF and AB (see Fig. 4.10) at the observation time $T = 7$.

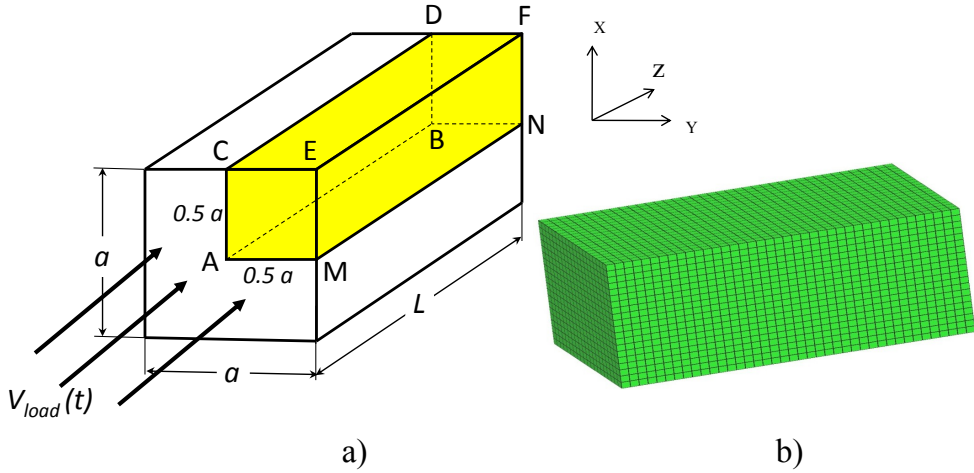


Figure 4.10: Impact of an elastic 3-D square bar of length $L = 2$ and width $a = 2$ against a rigid wall (a). A uniform mesh with $20 \times 20 \times 40 = 16000$ linear $Q8$ finite elements (b).

Similar to the previous 1-D and 2-D impact problems, the numerical results after basic computations contain spurious oscillations for all formulations; see Fig. 4.11. For the standard approach with the lumped mass matrix, the solution with time increments close to the stability limit Δt^{st} is more accurate than that with very small time increments $\Delta t^{st}/20$; e.g., see curves 1 and 2 in Fig. 4.11 (curve 1 is closer to more accurate results, curves 3 and 4, obtained by the use of the formulations with reduced dispersion).

Figs. 4.12-4.14 show the results after the filtering stage for the formulations with reduced dispersion as well as for the standard formulation with the lumped mass matrix. As can be seen from Figs. 4.12 and 4.13, the results obtained at basic computation at very small time increments $\Delta t^{st}/20$ (curves 3) and at time increments close the stability limit Δt^{st} (curves 1) are different for some intervals along the z axis. However, similar to the 2-D case, small time increments $0.5\Delta t^{st}$ (curves 2) and $\Delta t^{st}/20$ (curves 3) yield practically the same results for the formulations with the reduced dispersion; i.e., from the computational point of view, time increments $0.5\Delta t^{st}$ can be recommended for these new formulations at basic computations. It

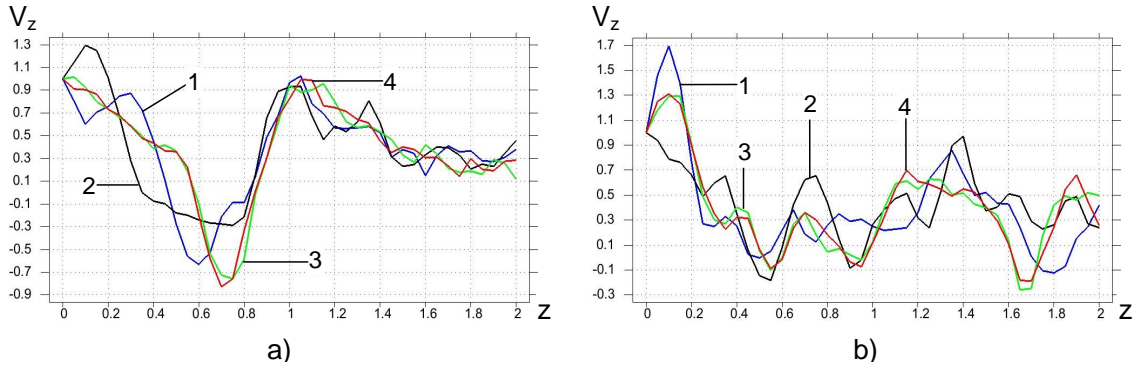


Figure 4.11: The distribution of the axial v_z velocity components along lines EF (a) and AB (b) (see Fig. 4.10) after basic computations at time $T = 7$ on a uniform mesh with $20 \times 20 \times 40 = 16000$ linear $Q8$ finite elements. The Poisson's ratio is $\nu = 0.3$. The results are obtained by the explicit central difference method with the lumped mass matrix (curves 1 and 2), with the averaged mass matrix (curves 3), and with the modified integration rule (curves 4). The following time increments are used: Δt^{st} (curves 1) and $\Delta t^{st}/20$ (curves 2-4).

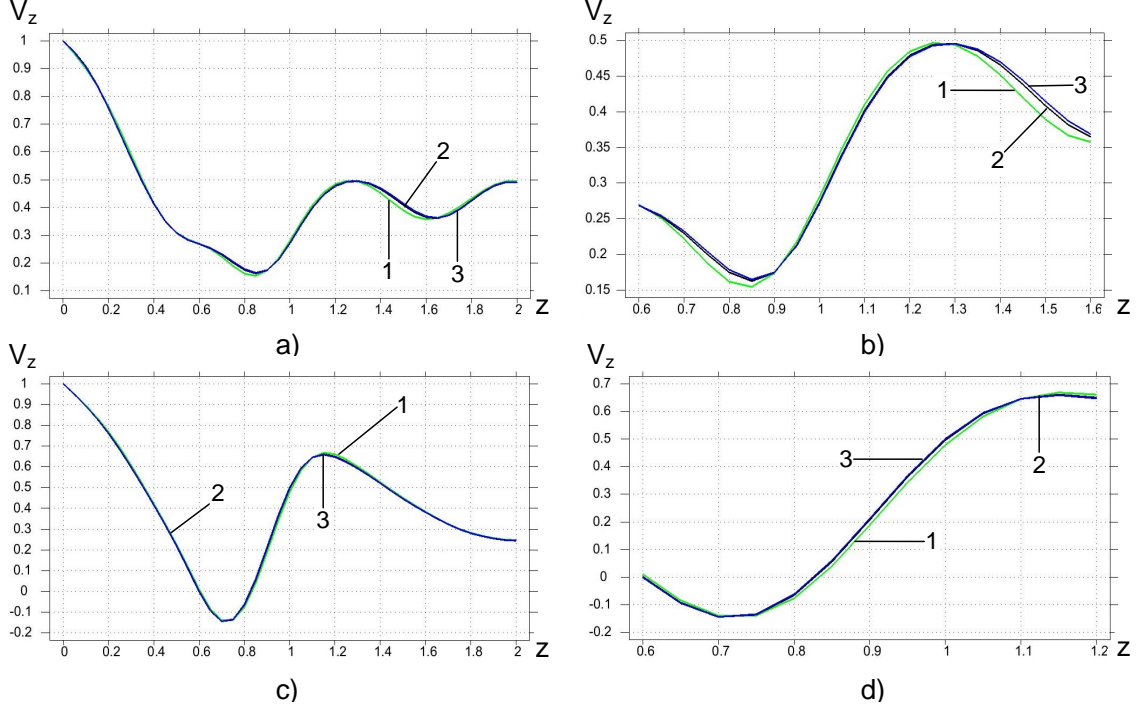


Figure 4.12: The distribution of the axial v_z velocity components along lines AB (a, b) and EF (c, d) (see Fig. 4.10) at time $T = 7$ on a uniform mesh with $20 \times 20 \times 40 = 16000$ linear Q8 finite elements. The Poisson's ratio is $\nu = 0.3$. The results are shown after the filtering of the solutions at basic computations obtained by the explicit central difference method with the averaged mass matrix and the following time increments: Δt^{st} (curves 1), $0.5\Delta t^{st}$ (curves 2) and $\Delta t^{st}/20$ (curves 3). b) and d) show the zoomed graph a) and c), respectively.

also can be seen from Fig. 4.14 that at small time increments $0.5\Delta t^{st}$, the solutions obtained with the average mass matrix and with the modified integration rule are close to each other (similar to the 2-D case). The numerical solution for the standard formulation with the lumped mass matrix is less accurate on the same mesh; see curves 5 in Fig. 4.14. We should also mention that similar to the 1-D and 2-D cases, the size of the time increments calculated by Eqs. (3.1) - (3.3) for the filtering stage allows the quantitative estimation of the advantage of the modified integration rule (or the averaged mass matrix) technique compared with the standard lumped mass matrix in the 3-D case as well.

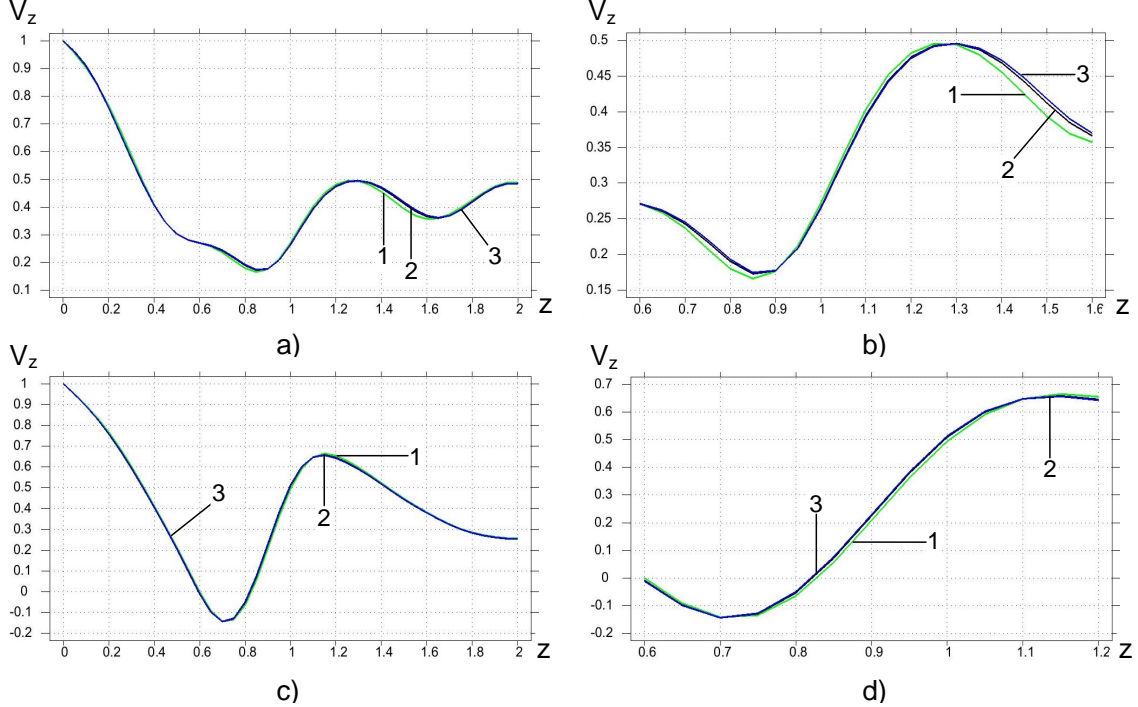


Figure 4.13: The distribution of the axial v_z velocity components along lines AB (a, b) and EF (c, d) (see Fig. 4.10) at time $T = 7$ on a uniform mesh with $20 \times 20 \times 40 = 16000$ linear Q8 finite elements. The Poisson's ratio is $\nu = 0.3$. The results are shown after the filtering of the solutions at basic computations obtained by the explicit central difference method with the modified integration rule and the following time increments: Δt^{st} (curves 1), $0.5\Delta t^{st}$ (curves 2) and $\Delta t^{st}/20$ (curves 3). b) and d) show the zoomed graph a) and c), respectively.

4.4 2D transient acoustic problems: impact of a plate

Here, we will consider the solution of a 2-D transient acoustic problem described by the scalar wave equation

$$\frac{\partial^2 u}{\partial t^2} - c_o^2 \nabla^2 u = 0, \quad (4.2)$$

where u is the field variable, c_o is the wave velocity. The application of the space discretization to Eq. (4.2) leads to the semi-discrete system, Eq. (1.5). In this section we will show that the two-stage time integration technique yields accurate numerical results for acoustic wave propagation obtained by the finite element techniques with

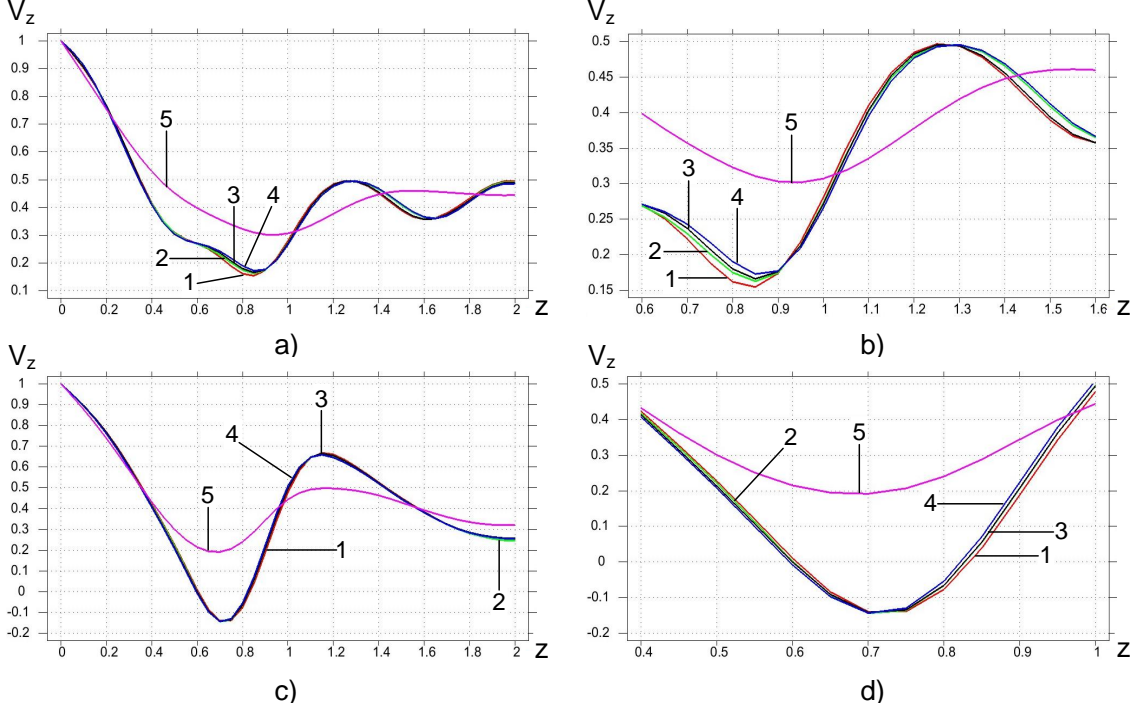


Figure 4.14: The distribution of the axial v_z velocity components along lines AB (a, b) and EF (c, d) (see Fig. 4.10) at time $T = 7$ on a uniform mesh with $20 \times 20 \times 40 = 16000$ linear Q8 finite elements. The Poisson's ratio is $\nu = 0.3$. The results are shown after the filtering of the solutions at basic computations obtained by the explicit central difference method with the averaged mass matrix (curves 1 and 2), with the modified integration rule (curves 3 and 4) and with the lumped mass matrix (curves 5) and the following time increments: Δt^{st} (curves 1 and 3), $0.5\Delta t^{st}$ (curves 2, 4, and 5). b) and d) show the zoomed graph a) and c), respectively.

reduced dispersion in the multidimensional case. Similar to the 1-D case and with the same coefficients a_1 and a_2 , the size of time increments at the filtering stage for multidimensional problems (see Eq. (3.3) from Chapter III for acoustic problems and the papers [47, 50] for elastodynamics problems) indirectly defines the border between the actual frequencies and the spurious high frequencies; i.e., indirectly defines the ranges of actual and spurious frequencies in the multidimensional case. Therefore, it can be used for the comparison and the prediction of accuracy of numerical results obtained by different space-discretization techniques. Here we will show 2-D examples of the application of the two-stage time integration technique to the standard linear and quadratic finite elements as well as to the linear elements with reduced dispersion

used with diagonal and non-diagonal mass matrices.

First, we consider a square plate of length 2×2 instantly loaded in the center. Due to symmetry, Fig. 4.15a includes only a quarter of the plate where the x - and y -axes are the axes of symmetry and $AD = AB = 1$. The wave velocity is chosen to be $c_o = 1$. The following boundary conditions are applied: $\frac{\partial u}{\partial n} = 0$ along the entire boundary AB , BC , CD and AD ($\frac{\partial}{\partial n}$ is the normal derivative at the boundary); a concentrated load is instantly applied at point A and is prescribed in terms of the value of the function $u(0, 0, t) = 1$. Zero initial conditions are used; i.e., $u(x, y, 0) = v(x, y, 0) = 0$.

The observation time is chosen to be $T = 0.8$. During this time the wave travels from point A to the boundary but does not reach it. Therefore, the zero boundary conditions at BC and CD do not affect the solution at time $T = 0.8$. By symmetry, the solution to this problem at any point depends on the radius with the center at point A and is independent of the angle between the radius and the x -axis. The problem is solved on uniform meshes with $100 \times 100 = 10000$, $300 \times 300 = 90000$, and $800 \times 800 = 640000$ linear four-node quadrilateral finite elements by the reduced-dispersion technique with ($\gamma = \frac{3-\tau^2}{2}$ and $\alpha_K = \sqrt{\frac{2}{3}}$) as well as by the standard approach with the lumped mass matrix. The time increments close to the stability limit are used in basic computations; i.e., the time increments corresponding to $\tau = 0.8$ for the reduced-dispersion technique and $\tau = 1$ for the standard approach with the lumped mass matrix. For the filtering stage, the time increments are defined by Eqs. (3.1)-(3.3) from Chapter III.

Fig. 4.15 shows the distribution of the field variable and its time derivative at the observation time $T = 0.8$ after basic computations and after the filtering stage obtained on a uniform mesh with $100 \times 100 = 10000$ linear four-node quadrilateral finite elements by the reduced-dispersion technique. As can be seen from Fig. 4.15, the filtering stage (c) just slightly improves the numerical anisotropy of the field variable u after basic computations (b) for which the small oscillations of isolines can be seen. However, due large spurious oscillations, the numerical anisotropy of the

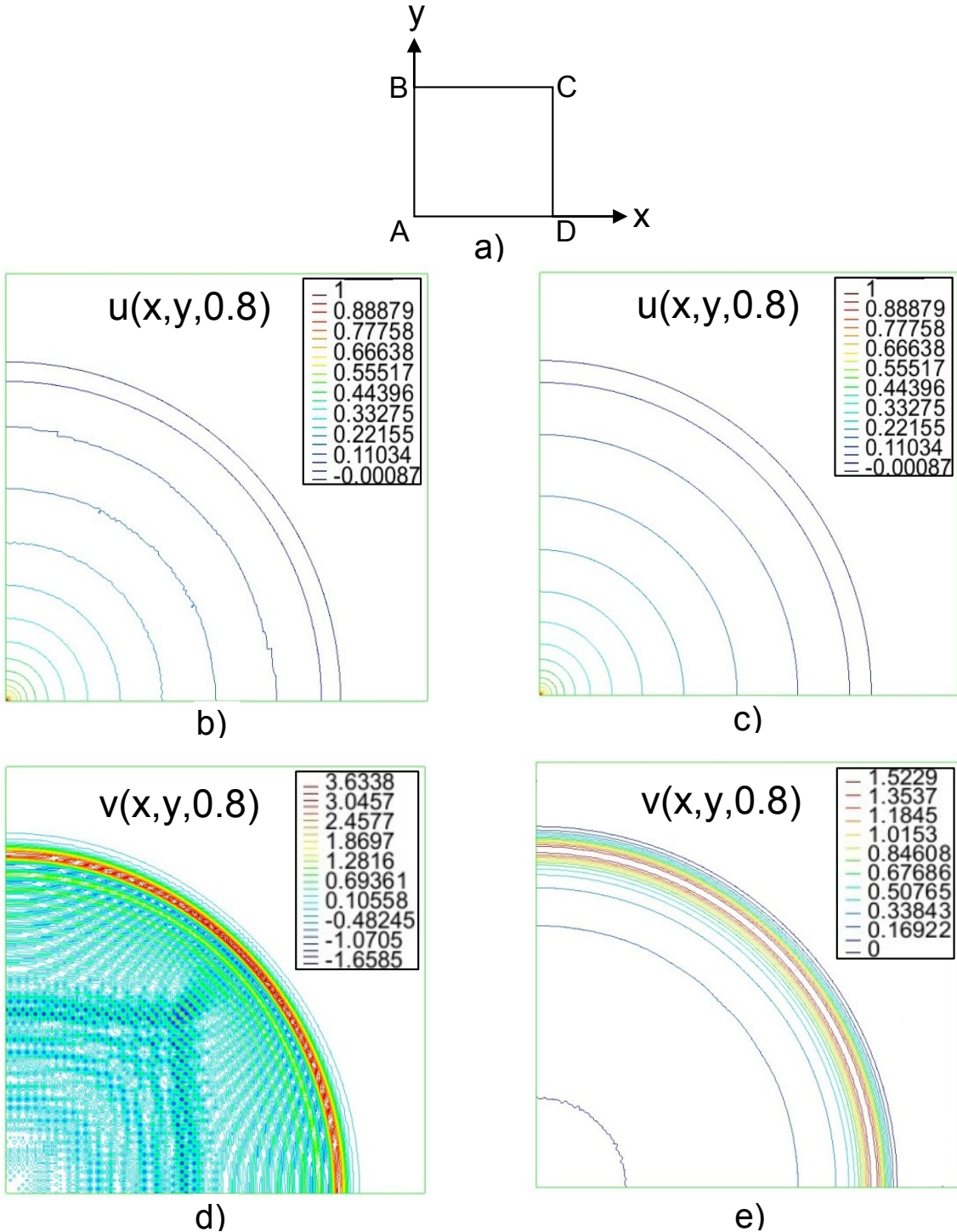


Figure 4.15: The 2-D impact of a plate by a concentrated load (a). The distribution of the field variable $u(x, y, 0.8)$ (b,c) and its time derivative $v(x, y, 0.8)$ (d,e) at the observation time $T = 0.8$ after basic computations (b,d) and after the filtering stage (c,e). A uniform mesh with $100 \times 100 = 10000$ linear four-node quadrilateral finite elements and the reduced-dispersion technique with $\gamma = \frac{3-\tau^2}{2}$ and $\alpha_K = \sqrt{\frac{2}{3}}$ are used.

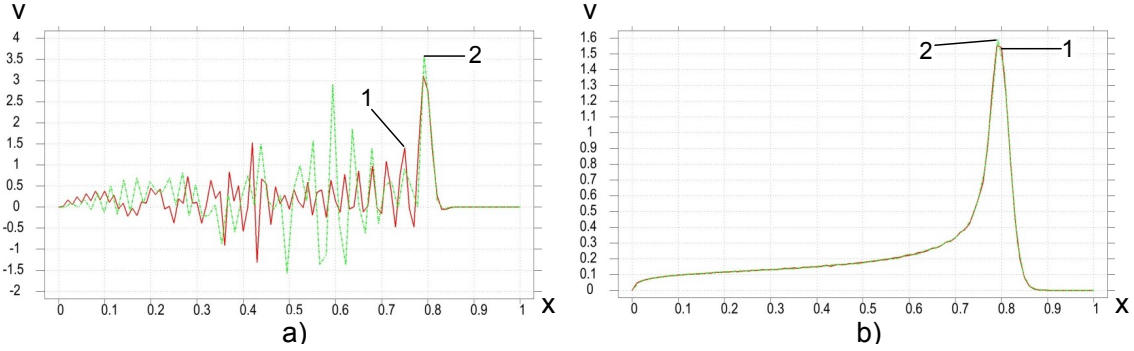


Figure 4.16: The velocity distribution along AD (curves 1) and along AC (curves 2) at the observation time $T = 0.8$ after basic computations (a) and after the filtering stage (b); see Fig. 4.15a for AD and AC . A uniform mesh with $100 \times 100 = 10000$ linear four-node quadrilateral finite elements and the reduced-dispersion technique with $\gamma = \frac{3-\tau^2}{2}$ and $\alpha_K = \sqrt{\frac{2}{3}}$ are used.

velocity v after basic computations (see (d)) is very large and makes the results non-valid (the exact solution corresponds to circular isolines for the problem). However, the filtering stage significantly reduces the numerical anisotropy for the velocity; see (e).

Let us consider the error for the velocity in Fig. 4.15 in more detail by plotting the velocity along the x -axis (line AD in Fig. 4.15a) and along the line forming angle $\Theta = \pi/4$ with the x -axis (line AC in Fig. 4.15a); see Fig. 4.16. The amplitudes of spurious oscillations after basic computations are different at different directions; see curves 1 and 2 in Fig. 4.16a. After the filtering stage, the solution for the velocity is totally different from that in basic computations; see curves 1 and 2 in Fig. 4.16b. The curves 1 and 2 after the filtering stage almost coincide; i.e, the filtering of spurious oscillations significantly reduces the numerical anisotropy. [h] It is interesting to note that mesh refinement without the filtering stage does not improve the numerical solutions. Moreover, we have divergent results at mesh refinement due to the increase in the amplitudes of spurious oscillations; see Fig. 4.17a,b,c. However, the two-stage time integration approach with the filtering stage yields convergent results at mesh refinement; see Fig. 4.17d.

As we mentioned in Section 2.4.3, the standard approach with the lumped mass matrix and time increments equal to the stability limit yields the analytical solution in the 1-D case. Therefore, it is interesting to study the accuracy of the standard approach at the time increments equal to the stability limit in the 2-D case. As can be seen from Fig. 4.18a, for the standard approach the velocity distributions after basic computations along lines AD ($\theta = 0$) and AC ($\theta = \pi/4$) are very different and the velocity distribution is more accurate along AD as predicted by the dispersion analysis in Section 2.4.3. If for the filtering stage we use the same time increments as those for the reduced dispersion technique in Figs. 4.15 - 4.17 (i.e., we use the same coefficients a_1 and a_2 in Eqs. (3.1)-(3.3)), then the velocity along line AD does not have spurious oscillations (see curve 1 in Fig. 4.18b) and is close to that in Fig. 4.16b;

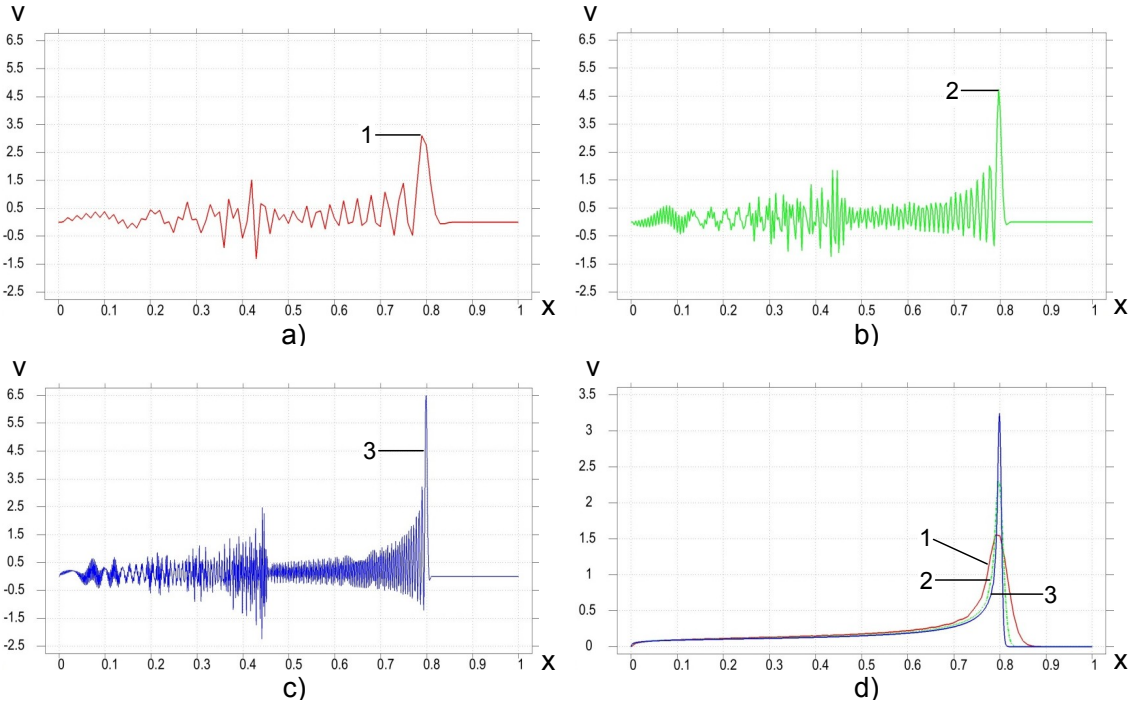


Figure 4.17: The velocity distribution along AD at the observation time $T = 0.8$ after basic computations (a,b,c) and after the filtering stage (d). Curves 1, 2 and 3 correspond to the uniform meshes with $100 \times 100 = 10000$, $300 \times 300 = 90000$, and $800 \times 800 = 640000$ linear four-node quadrilateral finite elements and the use of the reduced-dispersion technique with $\gamma = \frac{3-\tau^2}{2}$ and $\alpha_K = \sqrt{\frac{2}{3}}$.

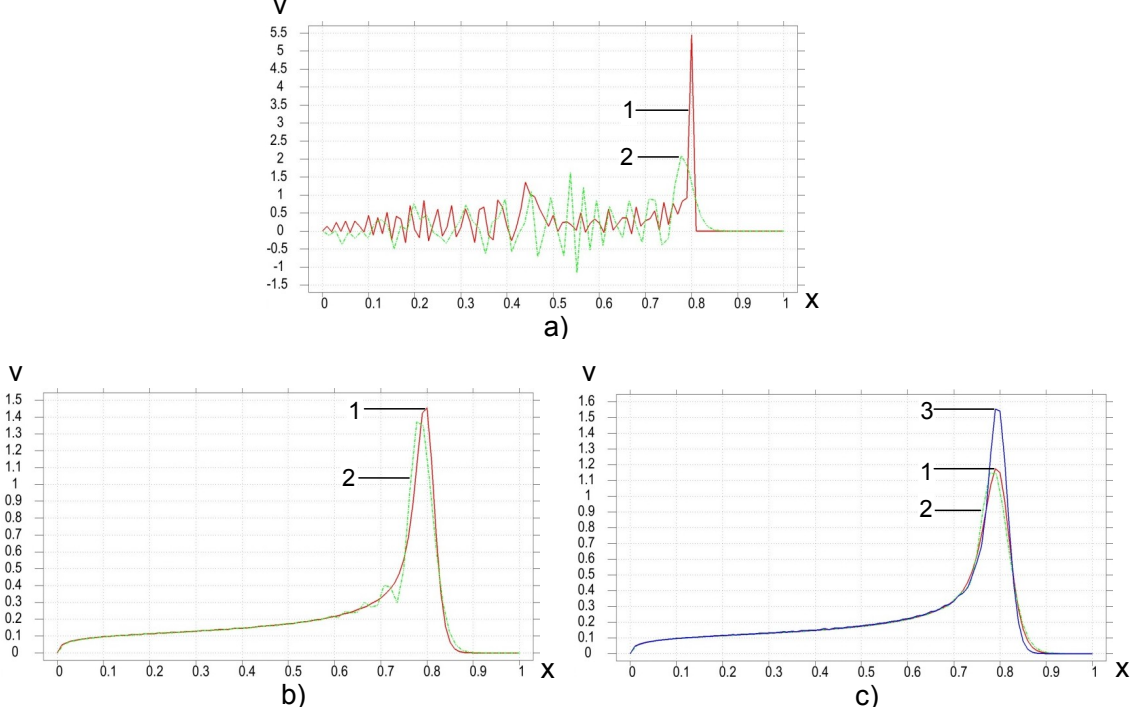


Figure 4.18: The velocity distribution along AD (curves 1) and along AC (curves 2) at the observation time $T = 0.8$ after basic computations (a) and after the filtering stage (b,c); see the text for explanations. A uniform mesh with $100 \times 100 = 10000$ linear four-node quadrilateral finite elements, the standard approach with the lumped mass matrix and the time increments equal to the stability limit in basic computations are used. The range of frequencies filtered in (b) is the same as that in Fig. 4.16b for the reduced dispersion technique. Curve 3 in (c) corresponds to curve 1 in Fig. 4.16b.

however, the velocity along line AC still has several spurious oscillations (see curve 2 in Fig. 4.18b). Therefore, in order to remove spurious oscillations in all directions, we will use the coefficients a_1 and a_2 in Eqs. (3.1)-(3.3) from Chapter III determined in the 1-D case for the standard approach with the time increments corresponding to $\tau \approx 0.71$ (see Section 2.4.3 and Section III). In this case, spurious oscillations has been removed from the numerical results (see curves 1 and 2 in Fig. 4.18c). A small difference between curves 1 and 2 in Fig. 4.18c corresponds to the numerical anisotropy of the standard approach. We can also see that the reduced dispersion technique yields much more accurate results than the standard approach (see curves 1 and 3 in Fig. 4.18c).

Second, we consider a square plate of length 1×1 , see Fig. 4.19a. The wave velocity is chosen to be $c_o = 1$. The following boundary conditions are applied: $\frac{\partial u}{\partial n} = 0$ along the boundary AB , EC , CD and AD ($\frac{\partial}{\partial n}$ is the normal derivative at the boundary); along the part BE of the upper boundary, an impact loading is prescribed in terms of the value of the field variable $u_{BE} = t$ (this corresponds to the instantaneous application of the velocity $v_{BE} = 1$). Zero initial conditions are used; i.e., $u(x, y, 0) = v(x, y, 0) = 0$. The observation time is chosen to be $T = 1.5$. During this time the wave travels from the boundary BE to all other boundaries, reflects from them and produces a complicated distribution of the velocity field at time $T = 1.5$, e.g., see Fig. 4.19b,c.

The problem is solved on uniform meshes with $100 \times 100 = 10000$ and $300 \times 300 = 90000$ linear Q4 four-node quadrilateral finite elements and on uniform meshes with $50 \times 50 = 2500$ and $66 \times 66 = 4356$ quadratic Q9 nine-node quadrilateral finite elements. For the linear Q4 elements we use the standard approach with the consistent mass matrix as well as the formulation with reduced dispersion for which the mass and stiffness matrices are calculated using the modified integration rule; see [95] (in the 1-D case this technique coincides with the averaged mass matrix technique used in Section 2.1). For the quadratic Q9 elements we use the standard formulation with the consistent mass matrix. The trapezoidal rule with very small time increments is used in basic computations for all numerical results. The time increments at the filtering stage are calculated according to Eqs. (3.1) - (3.3) for the linear and quadratic finite elements with the corresponding coefficients a_1 and a_2 from Table 1. Because we do not know the exact solution to the problem under consideration, the numerical solution after the filtering stage obtained on the fine mesh with $300 \times 300 = 90000$ linear finite elements with reduced dispersion is considered as a reference solution (we should also mention that the numerical solutions after the filtering stage converge to the unique solution at mesh refinement).

The numerical solutions after the stage of basic computations include large spurious high-frequency oscillations even for the results obtained by linear elements

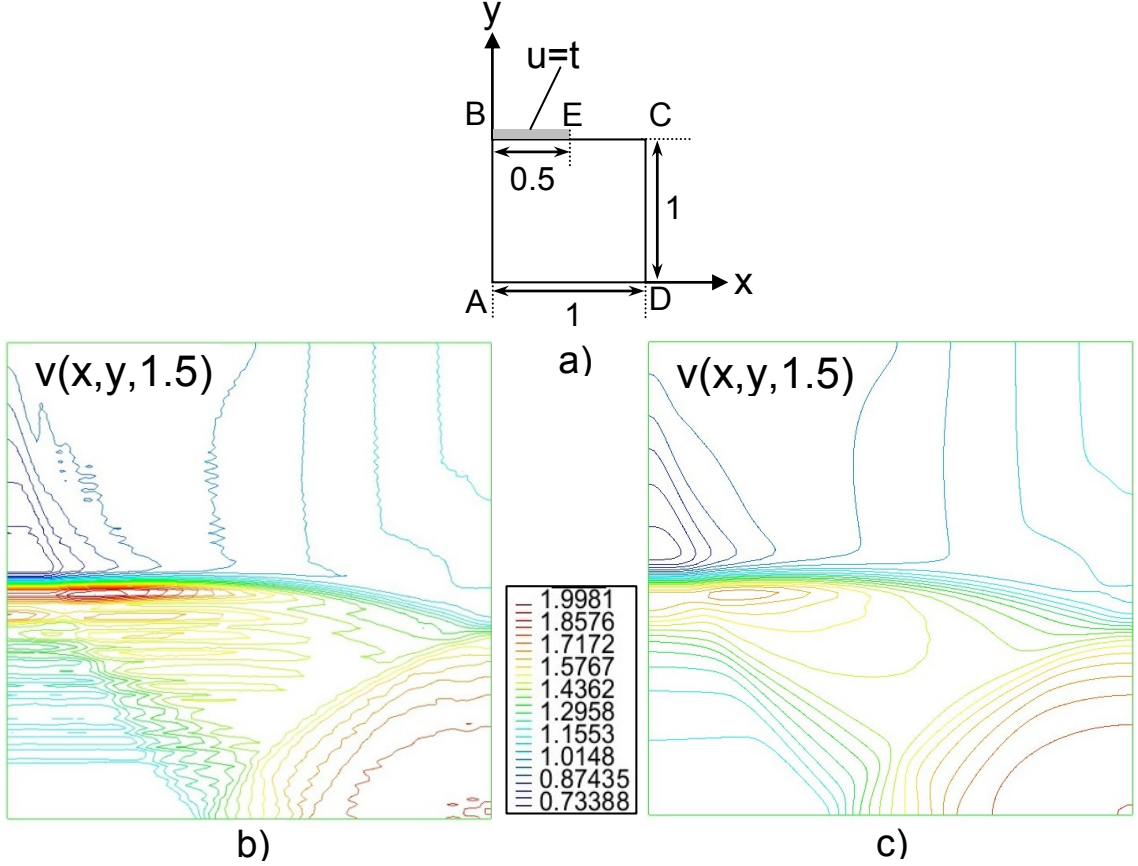


Figure 4.19: The 2-D impact of a plate (a). The distribution of the velocity $v(x, y, 1.5)$ in the plate at the observation time $T = 0.15$ after basic computations (b) and after the filtering stage (c). A uniform mesh with $100 \times 100 = 10000$ linear Q4 finite elements with reduced-dispersion is used.

with reduced dispersion; see Fig. 4.19b. These oscillations are removed from the numerical results at the filtering stage, see Fig. 4.19c. The spurious oscillations can be better seen when we plot the velocity along the boundary AB ; see Fig. 4.20a-c. Due to these oscillations, the results obtained with different space-discretization techniques are inaccurate and it is unclear how to compare them. However, after removing the spurious oscillations at the filtering stage, we can compare the numerical results (see curves 1-5 in Fig. 4.20d) with the reference solution (see curve 6 in Fig. 4.20d). As can be seen, at the same number of dof (for the meshes with $100 \times 100 = 10000$ Q4 elements and with $50 \times 50 = 2500$ Q9 elements), the linear elements with reduced

dispersion yield the most accurate results (see curve 1 in Fig. 4.20d).

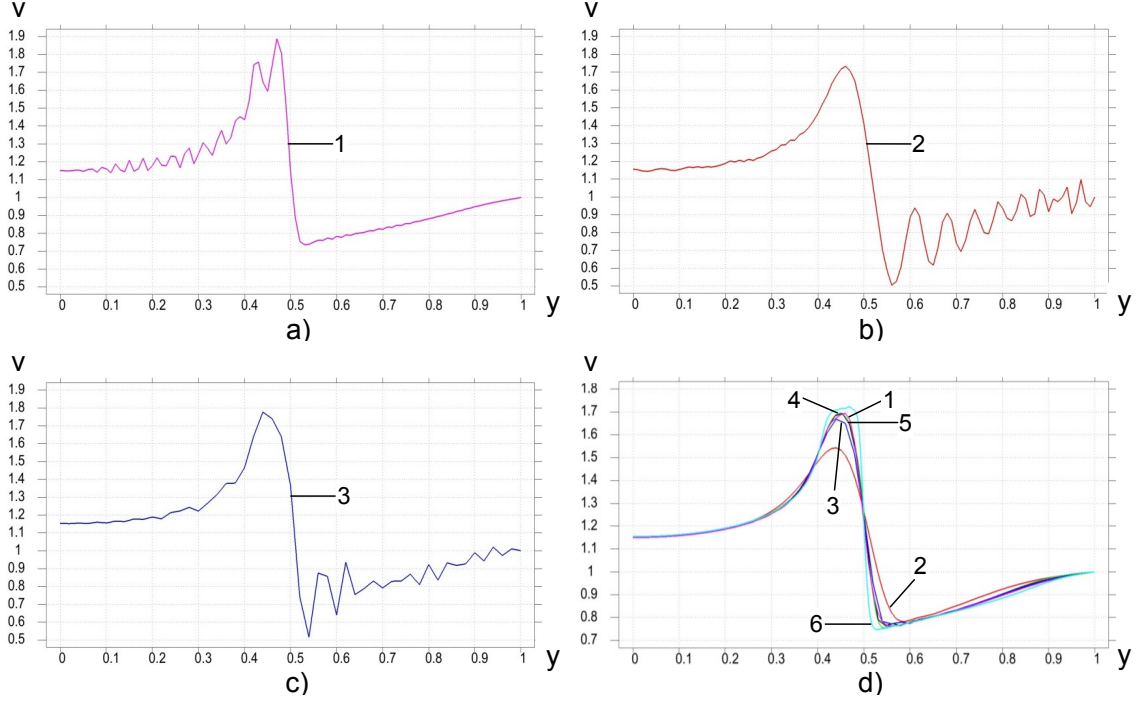


Figure 4.20: The velocity distribution along AB at the observation time $T = 1.5$ after basic computations (a-c) and after the filtering stage (d). Curves 1,2,3,4,5 and 6 correspond to the numerical results obtained on uniform meshes with $100 \times 100 = 10000$ Q4 (reduced dispersion), $100 \times 100 = 10000$ Q4 (standard), $50 \times 50 = 2500$ Q9 (standard), $300 \times 300 = 90000$ Q4 (standard), $66 \times 66 = 4356$ Q9 (standard), and $300 \times 300 = 90000$ Q4 (reduced dispersion) finite elements, respectively.

We can also see that the results obtained with the standard $300 \times 300 = 90000$ Q4 elements, with the standard $66 \times 66 = 4356$ Q9 elements and with $100 \times 100 = 10000$ Q4 elements with reduced dispersion yield approximately the same results. This means that at the same accuracy at $T = 1.5$, the linear elements with reduced dispersion reduce the number of dof by a factor of 9 compared with the standard Q4 elements and by a factor of 1.75 compared with the standard Q9 elements (moreover, the matrix bandwidth for Q9 elements is larger than the matrix bandwidth for Q4 elements and this leads to additional computational costs for Q9 elements).

Similar to the 1-D case, the results of this comparison can be predicted by the size of time increments used at the filtering stage that indirectly defines the range of

actual frequencies used in the numerical results. For example, according to Eqs. (3.1) - (3.3), the following time increments are used at the filtering stage: $\Delta t_1 = 0.00682$, $\Delta t_2 = 0.01442$, $\Delta t_3 = 0.00836$, $\Delta t_4 = 0.00683$, and $\Delta t_5 = 0.00676$ for the meshes with $100 \times 100 = 10000$ Q4 (reduced dispersion), $100 \times 100 = 10000$ Q4 (standard), $50 \times 50 = 2500$ Q9 (standard), $300 \times 300 = 90000$ Q4 (standard), and $66 \times 66 = 4356$ Q9 (standard) finite elements, respectively. As indicated in the previous section, the smaller size of time increments at the filtering stage corresponds to more accurate results; independent of space-discretization methods used, the same sizes of time increments at the filtering stage approximately correspond to the same accuracy; i.e., the sizes Δt_i ($i = 1, 2, \dots, 5$) predict the accuracy of the numerical results presented in Fig. 4.20d.

Chapter V

Comparison of accuracy of different orders of high-order standard, spectral, and isogeometric elements

The selection of the space-discretization methods used in this section is explained by their popularity as well as by the availability of the corresponding computer codes. For example, the standard high-order finite elements are implemented in the commercial finite-element code “COMSOL”, the spectral low- and high-order elements are implemented into the code “SEMLAB” (see the website “<http://www.gps.caltech.edu/ampuero/software.html>”), the isogeometric elements are implemented into the code ”IGAFEM” (see the website ”<http://sourceforge.net/projects/cmcodes/>”); we implemented the linear finite elements with reduced dispersion into the finite element code “FEAP”; see [97].

The application of time-integration methods to Eq. (1.5) yields the numerical solutions of transient elastodynamics or acoustic problems. These numerical results contain the space- and time-discretization errors. In this section, we first will study the space-discretization error introduced by different space-discretization techniques. In order to exclude the time-discretization error, we will select very small time increments at which the numerical solutions are practically independent of the size of time increments and are close the exact solution of Eq. (1.5).

The analytical study of the numerical dispersion error is very often used in the literature for the comparison of different space-discretization techniques; e.g., see [16, 23, 29, 58, 73, 74, 82, 83, 95] and many others. We should mention that the analytical study of the dispersion error is difficult for high-order space-discretization methods. Moreover, the analysis of the dispersion error based on the Helmholtz equation does not consider the effect of the observation time and time increments on the accuracy

of transient elastodynamics problems; however, this effect is very significant (see Section 5.4 below). In contrast to the study of the numerical dispersion error for the selected frequency in the Helmholtz equation, in many cases we are interested in the combined effect of a range of frequencies on the accuracy of numerical results obtained by different space-discretization techniques. This analysis can be done by the comparison of the accuracy of numerical solutions of the benchmark elastodynamics problems for which a wide range of frequencies is excited simultaneously. There is a very limited number of such benchmark elastodynamics problems with known analytical solutions.

In the present study, first we accurately solve the 1-D impact elastodynamics problem by the application of the two-stage time-integration technique consisting of the stage of basic computations and the filtering stage. The 1-D impact problem has the following important features: a) all low- and high-frequencies of the semi-discrete system, Eq. (1.5), are excited for this problem and b) the problem has a very simple analytical solution and, therefore, the comparison of the accuracy of the numerical solutions to this problem is easy when the spurious oscillations are removed.

In Section 5.1, we shortly introduce the high-order standard, spectral and iso-geometric elements. Then, in Sections 5.2 and 5.3, we accurately solve the 1-D impact problem using different space-discretization methods as well as the implicit and explicit time-integration methods with very small time increments in basic computations. For very small time increments, the error in time is much smaller than the space-discretization error and can be neglected (in this case the numerical solution in basic computations is close to the exact solution of the semi-discrete equations (1.5)) and is independent of a time-integration method used). Using the accurate numerical solutions to the 1-D impact problem, we compare the accuracy of different space-discretization techniques. We also show that the size of time increments used for the filtering of spurious oscillations at the filtering stage of the two-stage time-integration technique can be used as a quantitative measure for the comparison and prediction of the accuracy of different space-discretization approaches. In Section 5.4, we analyze

the effect of the size of time increments used in basic computations on the accuracy of numerical solutions obtained with different space-discretization techniques. According to our results, the typical statement in finite element textbooks, that for explicit methods a time increment should be close to the stability limit (e.g., see [9, 20]), is not true, because the size of a time increment should depend on the observation time and should be much smaller than the stability limit at large observation times.

We would also like to emphasize that despite a large number of different space-discretization techniques for elastodynamics problems, it is very often unclear what the best technique is. There are many factors that can affect the selection of the best method such as accuracy, computation costs, the simplicity of implementation and many others. In this section, we also estimate the computational efficiency of different space-discretization techniques for elastodynamics. We compare their computational costs for the solution of the 1-D impact problem at the same accuracy. Because for this problem all frequencies of the structure are excited and affect the accuracy, we believe that the solution to this problem can serve as the performance benchmark for different space-discretization techniques for elastodynamics.

5.1 High-order standard, spectral and isogeometric elements

The application of a space-discretization method to elastodynamics problems leads to the semi-discrete equations (1.5). Formally, for the space-discretization techniques considered in the study, the calculation of the mass and stiffness matrices can be represented by the classical finite element equations as follows:

$$\mathbf{M} = \sum_e \mathbf{M}^e, \quad \mathbf{K} = \sum_e \mathbf{K}^e \quad (5.1)$$

where the global mass \mathbf{M} and stiffness \mathbf{K} matrices have a banded structure (the dimensions of these matrices for different space-discretization techniques will be dis-

cussed below in Sections 5.2 and 5.3) and are obtained by the summation of the corresponding local (element) matrices \mathbf{M}^e and \mathbf{K}^e over all elements with eq. 2.9 and 2.10 in the 1-D case.

The shape matrix \mathbf{N} in Eq. (2.9- 2.10) are the shape functions that are polynomials for all space-discretization techniques considered in this section. For example, the standard low- and high-order finite elements are based on the uniform spacing of internal nodes within the element and the Lagrange polynomials $p_j(s)$ of degree N ($j = 1, 2, \dots, N$ where $N + 1$ is the number of nodes in an element).

For the spectral high-order elements with $N \geq 3$ (there is no difference between the standard finite elements and the spectral elements for $N \leq 2$), the Lagrange polynomials $p_j(s)$ of degree N and the non-uniform spacing of internal nodes within the element are used; the coordinates s_k ($s_k \in [-1, 1]$ with $k = 1, 2, \dots, N + 1$) of the nodes in the parametric space are the Gauss-Lobatto-Legendre points which are the $(N + 1)$ roots of the following equation

$$(1 - s_k^2)p'_N(s_k) = 0, \quad (5.2)$$

where $p'_N(s)$ is the derivative of the Legendre polynomial of degree N ; e.g., see [81]. It can also be shown that the application of the Gauss-Lobatto-Legendre integration rule with $N + 1$ integration points yields an approximate value of the mass matrix in Eq. (2.9) for the spectral elements and this approximate mass matrix is diagonal for any order of an element (e.g., see [81]).

In contrast to the standard finite elements and the spectral elements based on the piecewise-polynomial approximation of a numerical solution in the 1-D space (the derivatives of this solution are discontinuous across the element boundaries), the isogeometric elements allow the continuous derivatives of the numerical solution across the element boundaries. The shape functions for the isogeometric elements are based on the polynomial B-splines in the 1-D case; e.g., see [10, 11, 21, 38].

The semi-discrete equations for linear finite elements with reduced dispersion

can be easily obtained by the use of the global consistent \mathbf{M}^{cons} and lumped \mathbf{M}^{lump} mass matrices for the standard linear finite elements. In this case, the mass matrix \mathbf{M} in Eq. (1.5) should be replaced by the averaged mass matrix $\mathbf{M} = 0.5(\mathbf{M}^{cons} + \mathbf{M}^{lump})$ for implicit time integration methods (see [43, 58]); for explicit time-integration methods, Eq. (1.5) can be modified as follows:

$$\mathbf{M}^{lump} \ddot{\mathbf{U}} + \mathbf{M}[\mathbf{M}^{lump}]^{-1} \mathbf{K} \mathbf{U} = \mathbf{M}[\mathbf{M}^{lump}]^{-1} \mathbf{R} \quad (5.3)$$

where $\mathbf{M} = \mathbf{M}^{lump}\gamma + \mathbf{M}^{cons}(1 - \gamma)$ with $\gamma = \frac{3 - \bar{\tau}^2}{2}$ and the Courant number $\bar{\tau} = \frac{c_o \Delta t}{dx}$ (Δt is the size of a time increment, dx is the size of a linear finite element, $c_o = \sqrt{\frac{E}{\rho}}$ is the wave velocity).

The computational efficiency of a numerical technique for elastodynamics depends on the type (implicit or explicit) of a time-integration method used. Therefore, we will separately compare the numerical techniques with the diagonal mass matrices and explicit time-integration methods (they do not require the solution of a system of algebraic equations) and the numerical techniques with the non-diagonal mass matrices and implicit time-integration methods (they include the solution of a system of algebraic equations). To summarize, we will accurately solve wave propagation problems and compare the accuracy of the following space-discretization techniques:

- Standard finite elements from the 1st to the 5th order with the consistent mass matrix and implicit time integration methods
- Isogeometric elements of the 2nd and 3rd orders with the consistent mass matrix and implicit time integration methods
- Linear finite elements with reduced dispersion with the averaged mass matrix and implicit time integration methods
- Spectral elements from the 1st to the 10th order with the lumped mass matrix and explicit time integration methods

- Linear finite elements with reduced dispersion with the diagonal mass matrix (see Eq. (5.3)) and explicit time integration methods

In order to compare the results at short- and long-term integrations, the observation times are chosen to be $T = 2, 18, 98, 194$. The exact distributions of the velocities and stresses along the bar are the same at these observation times and correspond to the location of the wave front in the middle of the bar.

5.2 Space-discretization techniques with the non-diagonal mass matrix

Here, we will solve the 1-D impact problem using the standard low- and high-order finite elements (up to the 5th-order), the isogeometric 2nd- and 3rd-order elements, and the linear elements with reduced dispersion. For all these space-discretization methods, the non-diagonal mass matrices and the implicit trapezoidal rule with very small time increments in basic computations are used. Uniform meshes with 101 dof are used for all types of elements (except the standard 3rd-order elements with 100 dof); see Figs. 5.1 - 5.9. In addition to these meshes, we also use uniform meshes with 201 and 251 dof for the linear elements with reduced dispersion; see Figs. 5.8 and 5.9. For the isogeometric elements we use uniformly spaced control points as suggested in [21].

Figs. 5.1 - 5.7 show the numerical solutions for the velocity at different observation times. All space-discretization methods yield spurious oscillations after basic computations and the amplitudes of these oscillations increase with the increase in the observation time; see Figs. 5.1a,b - 5.7a,b. The slope of the wave front in the basic computations is steeper for short observation times and is more diffusive for large observation times. The filtering stage removes the spurious oscillations. However, despite the same analytical solutions at the selected observation times, the numerical results after the filtering stage are more accurate for short observation times than

those for large observation times; see Figs. 5.1c,d - 5.7c,d.

Because the error in time is very small in these calculations and can be neglected, the difference in the numerical results for different observation times is due to the space-discretization error (which is also related to the dispersion error). This difference is also smaller for higher-order elements compared with lower-order elements (the dispersion error for higher-order elements is smaller). Fig. 5.8 compares the numerical results for the standard low- and high-order finite elements at time $T = 18$. As can be seen, at the same number of dof, the increase in the order of the standard finite elements leads to the increase in accuracy. This increase is significant from the transition from the 1st-order to the 2nd-order finite elements (see curves 2 and 3 in Fig. 5.8a,b) and is much smaller from the transition from the 2nd- to the 3rd-order finite elements and so on (see curves 3-5 Fig. 5.8a,b). At the same number of dof, the calculations with higher-order elements lead to a greater computation cost (e.g., due to a greater bandwidth of the finite-element matrices for higher-order elements). Therefore, the estimation of the computation cost at the same accuracy is necessary in order to select an optimal space-discretization strategy: to use the standard high-order elements or to use the standard low-order elements with a larger number of dof (mesh refinement).

Figs. 5.8 and 5.9 also compare the accuracy of different space-discretization techniques at times $T = 18$ and $T = 194$. For all types of elements we have sparse matrices described by the bandwidth b . As can be seen, at the same number $n_1 = 101$ of dof, the isogeometric 3rd-order elements (curves 6) yield the most accurate results (compared with the standard 5th-order elements or the linear elements with reduced dispersion). The results with the standard 3rd-order elements are close to those obtained by the elements with reduced dispersion at $n_1 = 101$ (see curves 2 and 4 in Fig. 5.8c,d). However, the results at time $T = 18$ obtained by the linear elements with reduced dispersion at $n_2 = 201$ dof (with the bandwidth $b_2 = 3$) are close to those for the isogeometric 3rd-order elements with $n_1 = 101$ dof (with the bandwidth $b_1 = 7$) and are even slightly more accurate; see curves 3 and 6 in Fig. 5.9a. Implicit

time-integration methods with the considered space-discretization techniques include a solution of a system of algebraic equations with the computation cost proportional to nb^2 for the matrix factorization and to nb for the back substitution (n is the number of dof, b is the bandwidth and $n \gg b$). For 1-D uniform meshes, we have $\frac{n_1}{n_2} \approx 0.5$ and $\frac{b_1}{b_2} = \frac{7}{3}$. This means at the same accuracy at time $T = 18$, the linear elements with reduced dispersion and 201 dof require much less computation time compared with the isogeometric 3rd-order elements with 101 dof.

We should mention that for the same accuracy, the difference in the computation time between the isogeometric 3rd-order elements and the linear elements with reduced dispersion depends on the observation time. Despite the fact that the isogeometric elements become more accurate at larger observation time compared with other space-discretization techniques (see Fig. 5.9b), even at the large observation time $T = 194$, the linear elements with reduced dispersion are still more computationally efficient than the isogeometric elements. For example, the results obtained at time $T = 194$ by the linear elements with reduced dispersion for 251 dof are slightly more accurate and require less computation time compared with the isogeometric 3rd-order elements with 101 dof; see curves 4 and 6 in Fig. 5.9b.

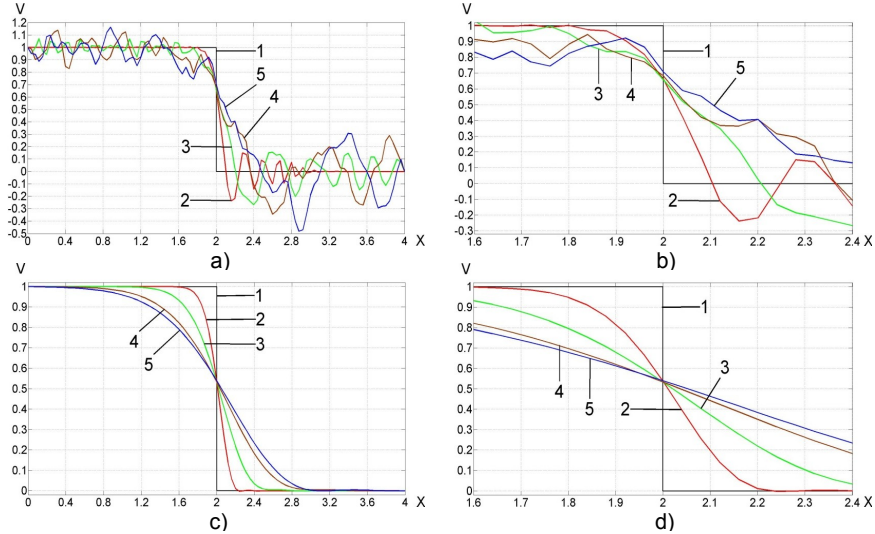


Figure 5.1: The velocity distribution along the bar after (a, b) basic computations (the consistent mass matrix and small time increments) and after (c, d) post-processing. A uniform mesh with the standard linear elements and 101 dof is used. Curves 1 correspond to the analytical solutions. Curves 2, 3, 4 and 5 correspond to the observation times $T = 2, 18, 98$ and 194, respectively. b) and d) show the zoomed graphs a) and c) in the range $1.6 < x < 2.4$.

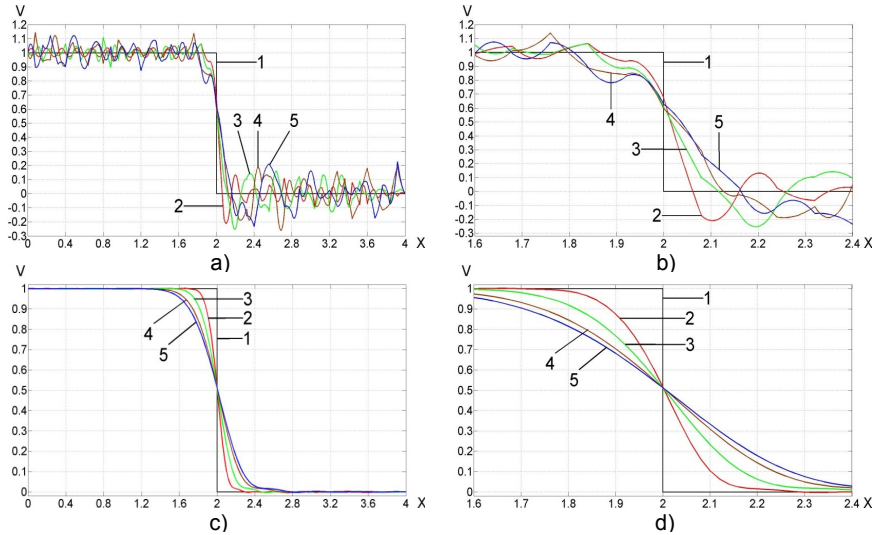


Figure 5.2: The velocity distribution along the bar after (a, b) basic computations (the consistent mass matrix and small time increments) and after (c, d) post-processing. A uniform mesh with the standard quadratic elements and 101 dof is used. Curves 1 correspond to the analytical solutions. Curves 2, 3, 4 and 5 correspond to the observation times $T = 2, 18, 98$ and 194, respectively. b) and d) show the zoomed graphs a) and c) in the range $1.6 < x < 2.4$.

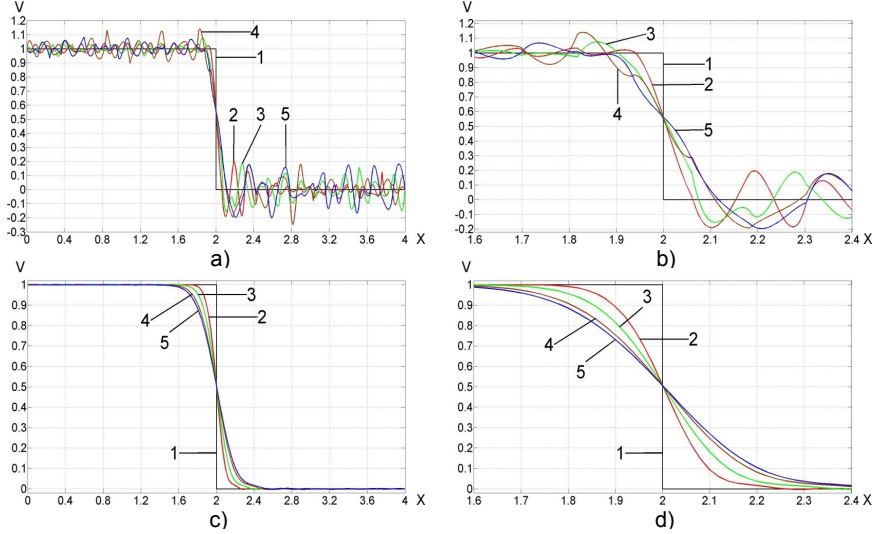


Figure 5.3: The velocity distribution along the bar after (a, b) basic computations (the consistent mass matrix and small time increments) and after (c, d) post-processing. A uniform mesh with the standard 3rd-order elements and 100 dof is used. Curves 1 correspond to the analytical solutions. Curves 2, 3, 4 and 5 correspond to the observation times $T = 2, 18, 98$ and 194 , respectively. b) and d) show the zoomed graphs a) and c) in the range $1.6 < x < 2.4$.

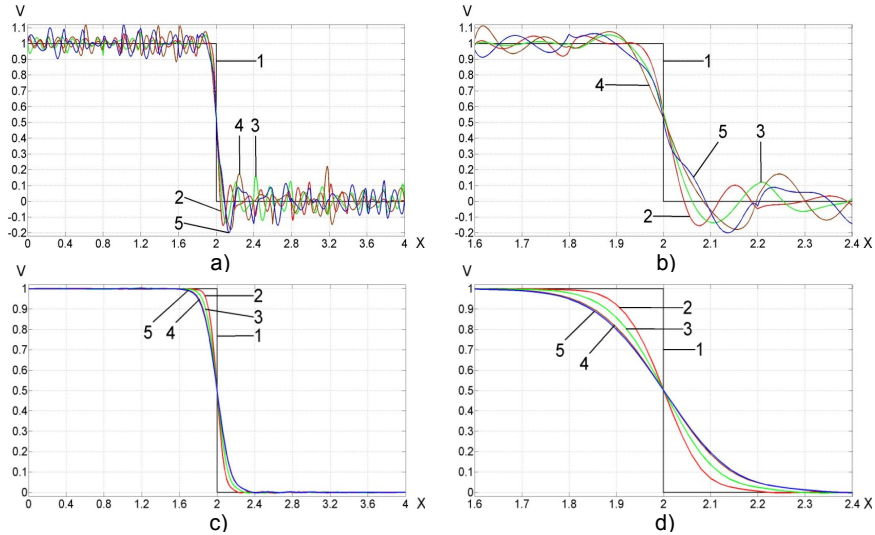


Figure 5.4: The velocity distribution along the bar after (a, b) basic computations (the consistent mass matrix and small time increments) and after (c, d) post-processing. A uniform mesh with the standard 5th-order elements and 101 dof is used. Curves 1 correspond to the analytical solutions. Curves 2, 3, 4 and 5 correspond to the observation times $T = 2, 18, 98$ and 194 , respectively. b) and d) show the zoomed graphs a) and c) in the range $1.6 < x < 2.4$.

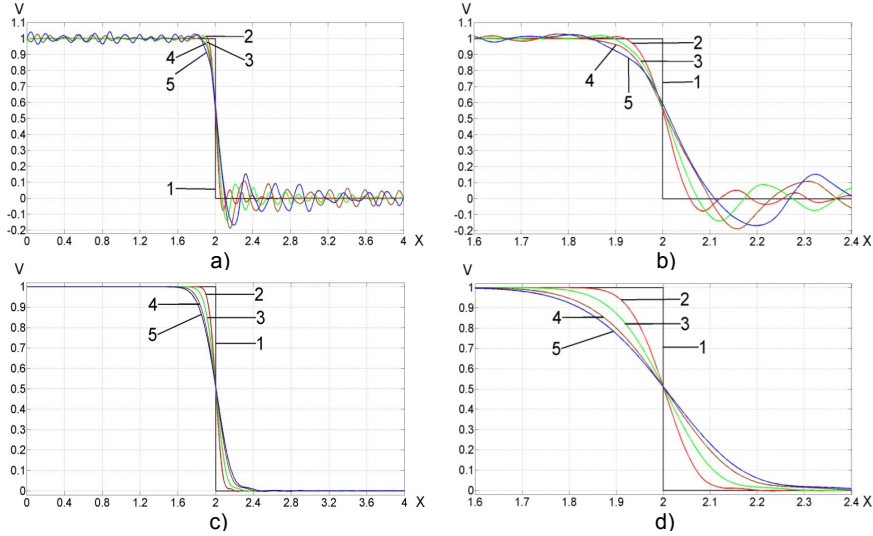


Figure 5.5: The velocity distribution along the bar after (a, b) basic computations (the consistent mass matrix and small time increments) and after (c, d) post-processing. A uniform mesh with the isogeometric quadratic elements and 101 dof is used. Curves 1 correspond to the analytical solutions. Curves 2, 3, 4 and 5 correspond to the observation times $T = 2, 18, 98$ and 194 , respectively. b) and d) show the zoomed graphs a) and c) in the range $1.6 < x < 2.4$.

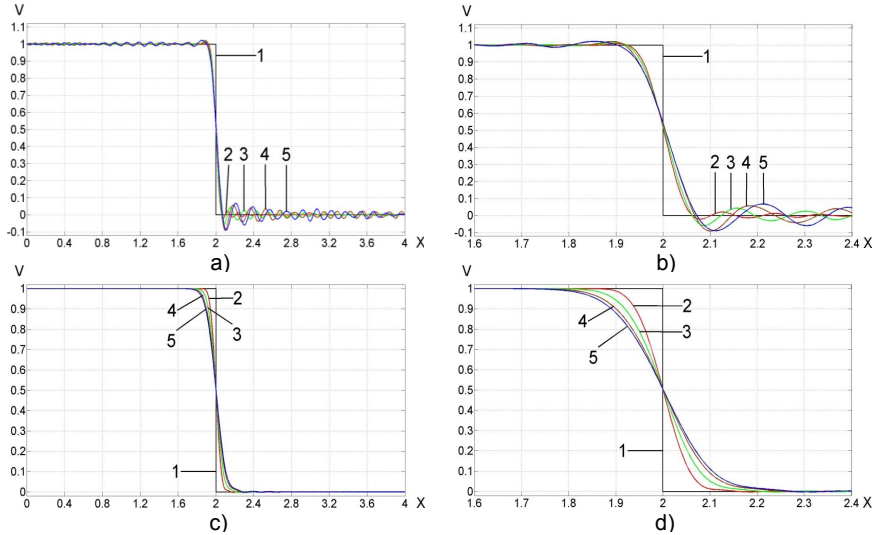


Figure 5.6: The velocity distribution along the bar after (a, b) basic computations (the consistent mass matrix and small time increments) and after (c, d) post-processing. A uniform mesh with the isogeometric 3rd-order elements and 101 dof is used. Curves 1 correspond to the analytical solutions. Curves 2, 3, 4 and 5 correspond to the observation times $T = 2, 18, 98$ and 194 , respectively. b) and d) show the zoomed graphs a) and c) in the range $1.6 < x < 2.4$.

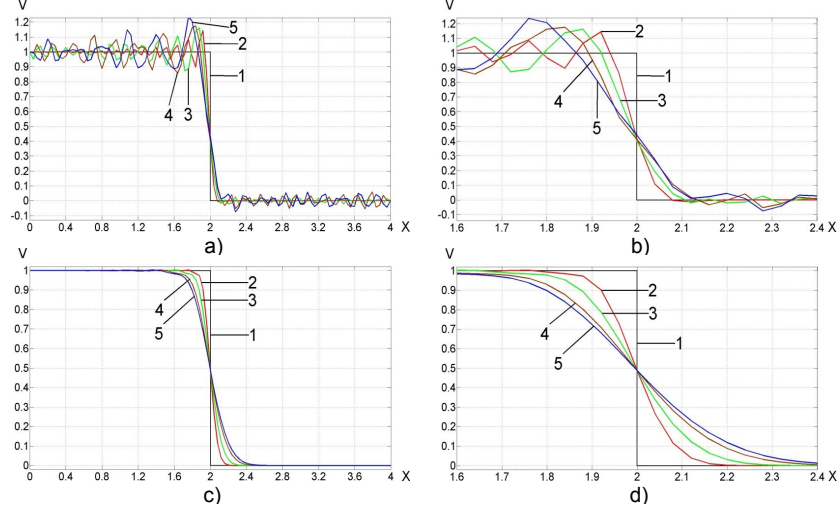


Figure 5.7: The velocity distribution along the bar after (a, b) basic computations (the non-diagonal mass matrix and small time increments) and after (c, d) post-processing. A uniform mesh with the linear elements with reduced dispersion and 101 dof is used. Curves 1 correspond to the analytical solutions. Curves 2, 3, 4 and 5 correspond to the observation times $T = 2, 18, 98$ and 194 , respectively. b) and d) show the zoomed graphs a) and c) in the range $1.6 < x < 2.4$.

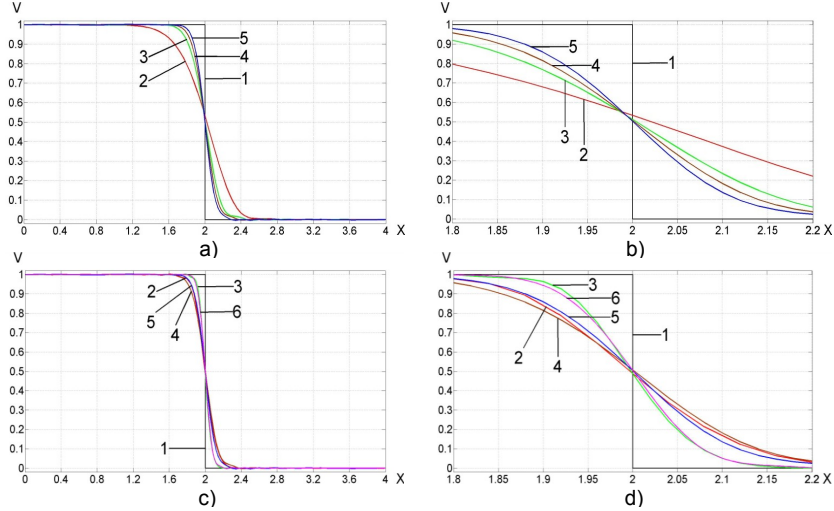


Figure 5.8: The velocity distribution along the bar at the observation time $T = 18$ after post-processing. We compare the curves from Fig. 5.1, 5.2, 5.3, 5.4, 5.6 and 5.7. Curves 1 correspond to the analytical solutions. Curves 2 in (a, b), 3 in (a, b), 4 and 5 correspond to the standard linear, quadratic, 3rd-order (100 dof) and 5th-order elements with 101 dof. Curves 2 in (c, d) and 3 in (c, d) correspond to the linear elements with reduced dispersion (the non-diagonal mass matrix) with 101 and 201 dof, respectively. Curves 6 correspond to the isogeometric 3rd-order elements with 101 dof. b) and d) show the zoomed graphs a) and c) in the range $1.8 < x < 2.2$.

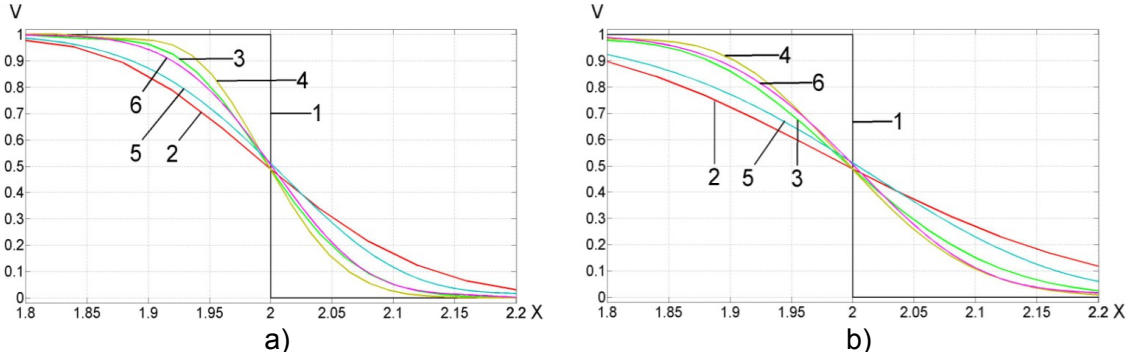


Figure 5.9: The velocity distribution along the bar in the range $1.8 < x < 2.2$ at the observation times $T = 18$ (a) and $T = 194$ (b) after post-processing. We compare the curves from Fig. 5.5 - 5.7. Curves 1 correspond to the analytical solutions. Curves 2, 3 and 4 correspond to the linear elements with reduced dispersion (the non-diagonal mass matrix) with 101, 201 and 251 dof, respectively. Curves 5 and 6 correspond to the isogeometric quadratic and 3rd-order elements with 101 dof.

5.3 Space-discretization techniques with the diagonal mass matrix

In this section we will solve the 1-D impact problem using the spectral elements (up to the 10th-order) and the linear elements with reduced dispersion. For all these space-discretization methods, the diagonal mass matrices and the explicit central-difference method with very small time increments are used. As we mentioned before, the spectral 1st- and 2nd-order elements coincide with the standard finite elements of the same orders. Uniform meshes with 101 dof are used for all types of elements (except the spectral 3rd-order elements with 100 dof); see Figs. 5.10 - 5.14. In addition to these meshes, we also use uniform meshes with 201, 301 and 401 dof for the linear elements with reduced dispersion; see Fig. 5.16. Figs. 5.10 - 5.14 show the numerical solutions for the velocity at different observation times. As can be seen, qualitatively the results for the spectral low- and high-order elements with the diagonal mass matrix are similar to those for the standard elements with the non-diagonal mass matrix (see the previous section 5.2). Similar behavior we observe for the elements with reduced dispersion used with non-diagonal (Fig. 5.7) and diagonal (Fig. 5.15) mass matrices.

Fig. 5.16a,b shows that at the same number 101 of dof, the increase in the order of the spectral elements improves the accuracy; see curves 3-7. At the same number of dof, the linear elements with reduced dispersion are slightly more accurate than the standard 2nd-order elements with the lumped mass matrix (see curves 2 and 4 in Fig. 5.16a,b). Figures 5.16c,d also shows that the linear elements with reduced dispersion and 201 dof are more accurate than the spectral 5th-order elements with 101 dof at time $T = 18$ and are slightly less accurate than the spectral 5th-order elements with 101 dof at the large observation time $T = 194$; see curves 2 and 6. Similarly, the linear elements with reduced dispersion and 301 dof are more accurate than the spectral 10th-order elements with 101 dof at time $T = 18$ and yield practically the same accuracy as the spectral 10th-order elements with 101 dof at the large observation time $T = 194$; see curves 3 and 7.

For the explicit time integration, the computations are very often implemented on the level of elements without the calculation of the global mass and stiffness matrices. Therefore, the computation cost in this case is related to the multiplication of the local effective stiffness matrix by a non-zero vector and is proportional to $n_{dof}^2 n_{el}$ where n_{dof} is the number of dof for one element and n_{el} is the number of elements. For example, $n_{dof}^2 n_{el} = 11^2 \cdot 10 = 1210$ for the spectral 10th-order elements with 101 dof and $n_{dof}^2 n_{el} = 2^2 \cdot 300 = 1200$ for the linear elements with reduced dispersion and 301 dof; i.e., the computational costs are approximately the same in this case. However, we can also reduce the computational cost for the linear elements with reduced dispersion by the use of the following procedure. Let us combine every 30 linear elements (e.g., starting from the left end of the bar) into one super-element. In this case we will obtain $n_{el} = 10$ super-elements. The computation cost for $n_{el} = 10$ super-elements is $n_{dof} b n_{el} = 31 \cdot 3 \cdot 10 = 930$ where $n_{dof} = 31$ is the number of dof of one super-element and $b = 3$ is the bandwidth of the effective stiffness matrix of one super-element consisting of 30 linear elements with reduced dispersion. This means that at the same or better accuracy (e.g, see curves 3 and 7 in Fig. 5.16c,d at the observation times $T = 18$ and $T = 194$), linear elements with reduced dispersion

and 301 dof require less computation time and are more computationally efficient compared with the spectral 10th-order elements with 101 dof at times $T = 18$ and $T = 194$.

In order to compare the accuracy of the numerical results obtained with the different space-discretization techniques as well as with the implicit and explicit time-integration methods, Fig. 5.16c,d also includes the numerical solutions obtained by the isogeometric 3rd-order elements (the non-diagonal mass matrix) with 101 dof. As can be seen, the accuracy of the isogeometric 3rd-order elements at time $T = 18$ and $T = 194$ is close to that of the spectral 10th-order elements at the same number of dof; see curves 5 and 7.

It is interesting to note that the size of time increments at the filtering stage calculated according to the formulas Eqs. (3.1) - (3.2) from Chapter III indirectly defines the range of actual frequencies used in numerical solutions (because spurious high-frequencies are damped out at the filtering stage) and can be used for the comparison of the accuracy of different space-discretization techniques; see the papers [43, 47]. If at the selected observation time T the time increment at the filtering stage for one space-discretization technique is smaller than that for another space-discretization technique then the former technique yields more accurate results at time T than the latter technique (if time increments are close to each other then the techniques include the same range of actual frequencies and yield approximately the same results). This is similar to the modal decomposition method for which the increase in the range of actual frequencies leads to the increase in the accuracy of numerical results. This also means that Eqs. (3.1) - (3.2) allow the quantitative comparison of the accuracy of different space-discretization techniques.

For example, according to Eqs. (3.1) - (3.2), we use the following time increments for the filtering stage at time $T = 18$: $\Delta t_1 = 0.0405$, $\Delta t_2 = 0.0235$, $\Delta t_3 = 0.0171$ and $\Delta t_4 = 0.0137$ for the linear elements with reduced dispersion (the diagonal mass matrix) with 101 dof, 201 dof, 301 dof and 401 dof, respectively; $\Delta t_5 = 0.0448$ for the standard quadratic elements (the diagonal mass matrix) with

101 dof; $\Delta t_6 = 0.0222$ for the spectral 10th-order elements (the diagonal mass matrix) with 101 dof; $\Delta t_7 = 0.0188$ for the isogeometric 3rd-order elements (the consistent mass matrix) with 101 dof.

At the large observation time $T = 194$, we have the following time increments for the filtering stage: $\Delta t_1 = 0.0679$, $\Delta t_2 = 0.0395$, $\Delta t_3 = 0.0288$ and $\Delta t_4 = 0.0230$ for the linear elements with reduced dispersion (the diagonal mass matrix) with 101 dof, 201 dof, 301 dof and 401 dof, respectively; $\Delta t_5 = 0.0695$ for the standard quadratic elements (the diagonal mass matrix) with 101 dof; $\Delta t_6 = 0.0266$ for the spectral 10th-order elements (the diagonal mass matrix) with 101 dof; $\Delta t_7 = 0.0269$ for the isogeometric 3rd-order elements (the consistent mass matrix) with 101 dof. Comparing these time increments at the same observation time, we can describe the accuracy of the numerical results discussed above. For example, at times $T = 18$ and $T = 194$, the time increments Δt_6 and Δt_7 are close to each other and the corresponding space-discretization techniques yield approximately the same accuracy; see curves 5 and 7 in Fig. 5.16c,d (similar results we have for the time increments Δt_1 and Δt_5 ; see curves 2 and 4 in Fig. 5.16a,b). We also have that $\Delta t_3 < \Delta t_6$ at time $T = 18$ and $\Delta t_3 > \Delta t_6$ at time $T = 194$ (see curves 3 and 7 in Fig. 5.16c,d and the comparison of the spectral elements and the elements with reduced dispersion described above in this section). It can be also seen that Δt_4 has the smallest value among all presented time increments and the corresponding linear elements with reduced dispersion and 401 dof yield the most accurate results; see curves 4 in Fig. 5.16c,d.

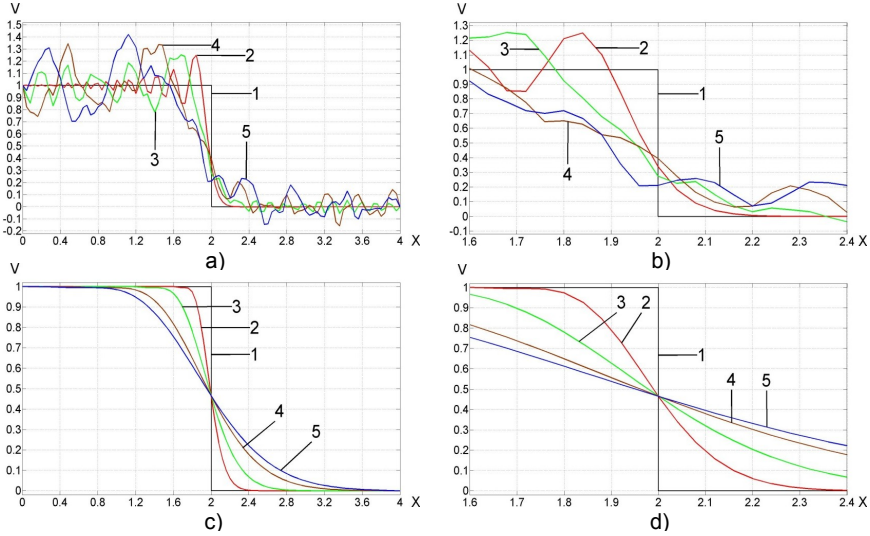


Figure 5.10: The velocity distribution along the bar after (a, b) basic computations (the lumped mass matrix and small time increments) and after (c, d) post-processing. A uniform mesh with the standard (spectral) linear elements and 101 dof is used. Curves 1 correspond to the analytical solutions. Curves 2, 3, 4 and 5 correspond to the observation times $T = 2, 18, 98$ and 194, respectively. b) and d) show the zoomed graphs a) and c) in the range $1.6 < x < 2.4$.

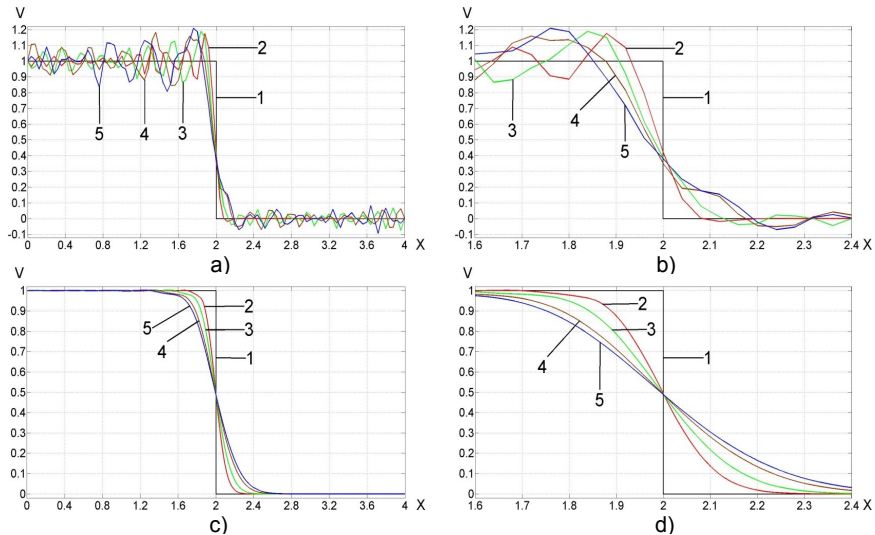


Figure 5.11: The velocity distribution along the bar after (a, b) basic computations (the lumped mass matrix and small time increments) and after (c, d) post-processing. A uniform mesh with the standard (spectral) quadratic elements and 101 dof is used. Curves 1 correspond to the analytical solutions. Curves 2, 3, 4 and 5 correspond to the observation times $T = 2, 18, 98$ and 194, respectively. b) and d) show the zoomed graphs a) and c) in the range $1.6 < x < 2.4$.

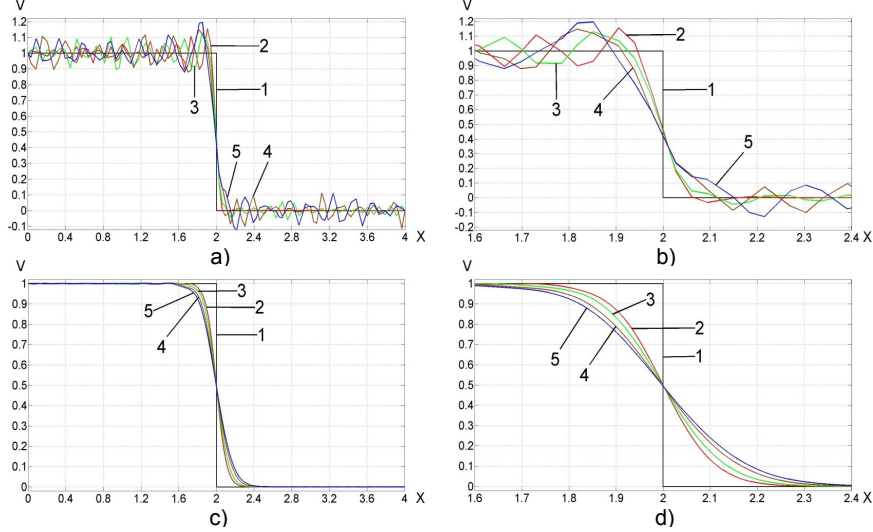


Figure 5.12: The velocity distribution along the bar after (a, b) basic computations (the lumped mass matrix and small time increments) and after (c, d) post-processing. A uniform mesh with the spectral 3rd-order elements and 100 dof is used. Curves 1 correspond to the analytical solutions. Curves 2, 3, 4 and 5 correspond to the observation times $T = 2, 18, 98$ and 194 , respectively. b) and d) show the zoomed graphs a) and c) in the range $1.6 < x < 2.4$.

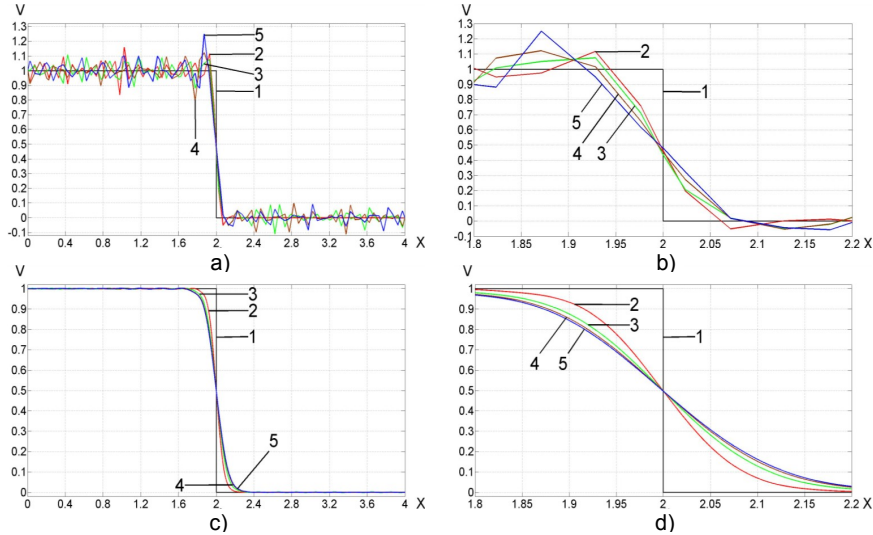


Figure 5.13: The velocity distribution along the bar after (a, b) basic computations (the lumped mass matrix and small time increments) and after (c, d) post-processing. A uniform mesh with the spectral 5th-order elements and 101 dof is used. Curves 1 correspond to the analytical solutions. Curves 2, 3, 4 and 5 correspond to the observation times $T = 2, 18, 98$ and 194 , respectively. b) and d) show the zoomed graphs a) and c) in the range $1.8 < x < 2.2$.

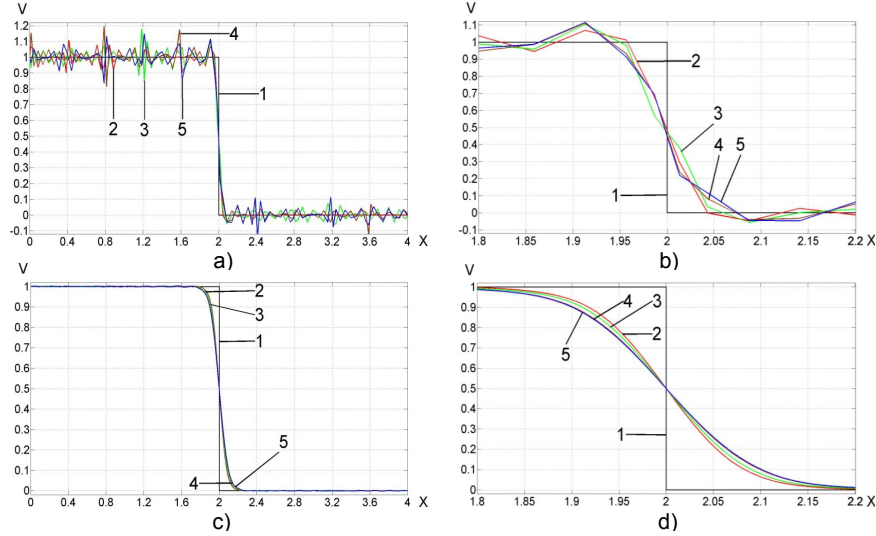


Figure 5.14: The velocity distribution along the bar after (a, b) basic computations (the lumped mass matrix and small time increments) and after (c, d) post-processing. A uniform mesh with the spectral 10th-order elements and 101 dof is used. Curves 1 correspond to the analytical solutions. Curves 2, 3, 4 and 5 correspond to the observation times $T = 2, 18, 98$ and 194 , respectively. b) and d) show the zoomed graphs a) and c) in the range $1.8 < x < 2.2$.

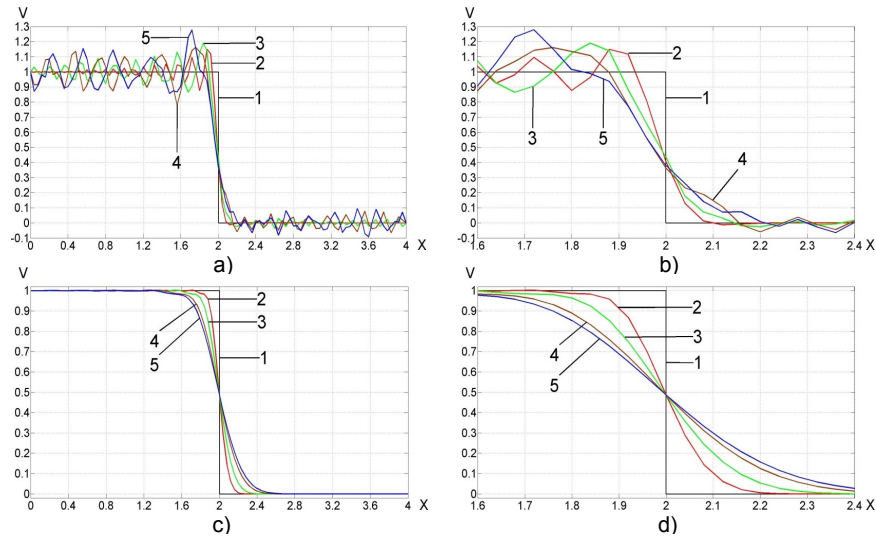


Figure 5.15: The velocity distribution along the bar after (a, b) basic computations (the lumped mass matrix and small time increments) and after (c, d) post-processing. A uniform mesh with the linear elements with reduced dispersion and 101 dof is used. Curves 1 correspond to the analytical solutions. Curves 2, 3, 4 and 5 correspond to the observation times $T = 2, 18, 98$ and 194 , respectively. b) and d) show the zoomed graphs a) and c) in the range $1.6 < x < 2.4$.

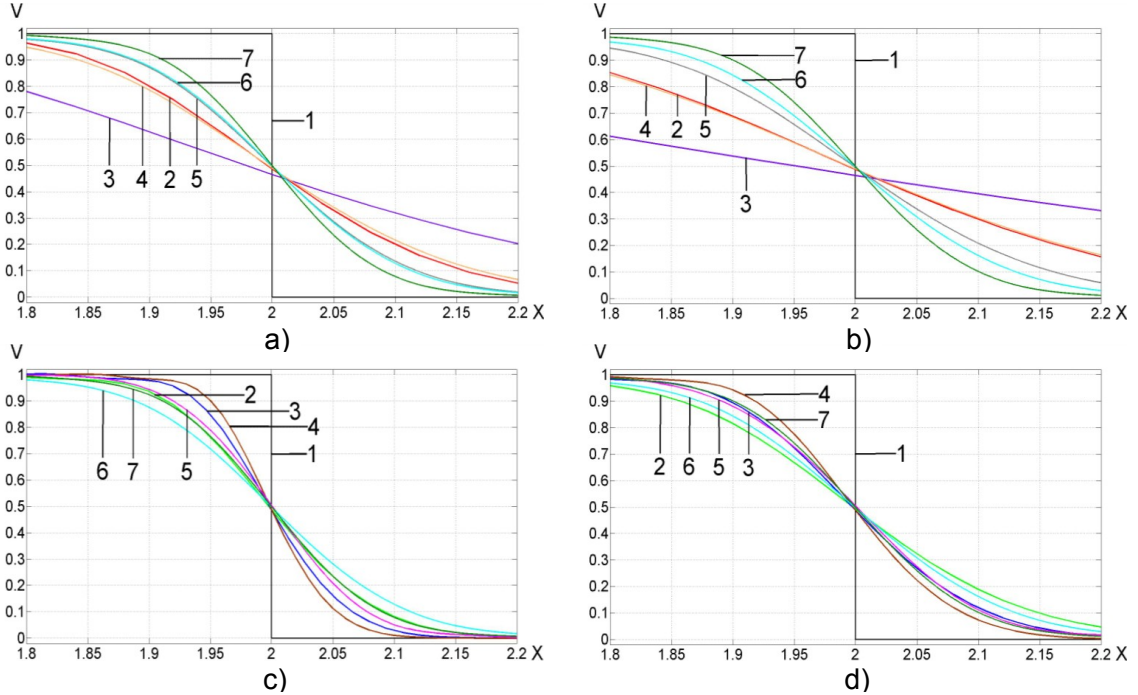


Figure 5.16: The velocity distribution along the bar in the range $1.8 < x < 2.2$ at the observation times $T = 18$ (a, c) and $T = 194$ (b, d) after post-processing. We compare the curves from Fig. 5.6, 5.10, 5.11, 5.13, 5.14 and 5.15. Curves 1 correspond to the analytical solutions. Curves 2 in (a, b), 2 in (c, d), 3 in (c, d) and 4 in (c, d) correspond to the linear elements with reduced dispersion (the lumped mass matrix) with 101, 201, 301 and 401 dof, respectively. Curves 3 in (a, b), 4 in (a, b), 5 in (a, b), 6 and 7 correspond to the spectral linear, quadratic, 4th-order, 5th-order and 10th-order elements with 101 dof. Curves 5 in (c, d) correspond to the isogeometric 3rd-order elements with 101 dof.

5.4 The effect of time increments in basic computations on the accuracy of different space-discretization techniques

In this section we will analyze the effect of a time increment in basic computations on the accuracy of the isogeometric elements (used with the implicit time-integration method) and the spectral high-order elements (used with the explicit time-integration method). We will show that very small time increments for these techniques yield more accurate results. Uniform meshes with 101 dof are used. Because implicit time-

integration methods can be used with any size of time increments, then we will use $d\bar{t} = 0.04$ as the largest time increment for the isogeometric elements. This time increment $d\bar{t} = 0.04$ corresponds to the stability limit of the standard linear finite elements with the lumped mass matrix at the same number 101 of dof. For the spectral high-order elements with the lumped mass matrix we estimate the stability limit dt^{st} from numerical experiments and then use the time increments that are close and smaller than the stability limit.

Figs. 5.17 - 5.25 show the effect of time increments on the accuracy of numerical results for the isogeometric 3rd-order elements as well for the spectral 3rd- and 10th-order elements. As can be seen, the results significantly depend on the observation time and the size of time increments in basic computations. In all cases, the decrease in the size of time increments in basic computations leads to the increase in the accuracy. We should also note that for the same elements, smaller time increments should be used at a larger observation time in order to get accurate results. However, in order to decrease the computation cost, the size of time increments should be as large as possible. As can be seen from Fig. 5.17, for the isogeometric 3rd-order elements at time $T = 2$, time increments $0.2d\bar{t}$ yield accurate results (the further time refinement does not significantly increase the accuracy). However, for the same elements, much smaller time increments $0.1d\bar{t}$ and $0.03d\bar{t}$ can be recommended at times $T = 18$ and $T = 194$; respectively (see Figs. 5.18 and 5.19).

Qualitatively, similar results are obtained for the spectral 3rd- and 10th-order elements in Figs. 5.20 - 5.25. For example, for the short observation time $T = 2$ accurate numerical results for these elements can be obtained at time increments $0.95dt^{st}$ which are close to the stability limit ($dt^{st} = 0.02817$ and $dt^{st} = 0.01130$ for the spectral 3rd-order and 10th-order elements, respectively); see Figs. 5.20 and 5.23. However, for larger observation times, the time increments should be significantly decreased; e.g., $0.1dt^{st}$ at the large observation time $T = 194$ (see Figs. 5.22 and 5.25). The results presented here show that small time increments in basic computations that yield a very small error in time should be used. In the paper [48], Dr. Idesman derived

an exact, closed-form a-priori global error estimator for 2nd-order time-integration methods and have shown that in order to have the same error in time at different observation times for each mode, the following relationships between time increments dt_1 and dt_2 used at different observation times T_1 and T_2 should be met $\frac{dt_1}{dt_2} = \sqrt{\frac{T_2}{T_1}}$. This error estimator is in a good agreement with the numerical results obtained above and can be used as follows. At a short observation time T_1 , the appropriate size dt_1 of time increments can be found from numerical experiments (e.g. using the time refinement). Then, for a large observation time T_2 , the size of time increments can be found with the formula $dt_2 = dt_1 \sqrt{\frac{T_1}{T_2}}$ for the 2nd-order time-integration methods (similar formulas have been also derived for high-order time-integration methods; see the papers [47, 48]).

Remarks:

1. For more accurate space-discretization techniques (e.g., the isogeometric 3rd-order elements or the spectral 10th-order elements) higher-frequencies are resolved more accurately compared with less accurate space-discretization techniques. It is also known that during time integration, at the same time increments the error in time is greater for higher modes. Therefore, more accurate space-discretization techniques require smaller time increments in order to have accurate results at higher modes.
2. Except the 1-D case with the standard linear finite elements and the lumped mass matrix as well as the linear finite elements with reduced dispersion and the lumped mass matrix (which are equivalent at the time increments equal to the stability limit, the decrease in the size of time increments in basic computations improves the accuracy of numerical results for all other space-discretization techniques considered in the study. In the 2-D and 3-D cases, the standard linear finite elements with the lumped mass matrix and the linear finite elements with reduced dispersion and the lumped mass matrix yield more accurate results at very small time increments. Therefore, we analyze and compare these elements

in section 5.3 at very small time increments in order to predict their accuracy in the multi-dimensional cases.

3. The examples of the application of the two-stage time-integration approach to the elastodynamics problems can be found in the papers [43, 47] for some selected space-discretization techniques in the multidimensional case. Similar to Section 4.4, they show the validity of the results obtained in Section 5.2 and 5.3 for 2-D and 3-D elastodynamics problems.

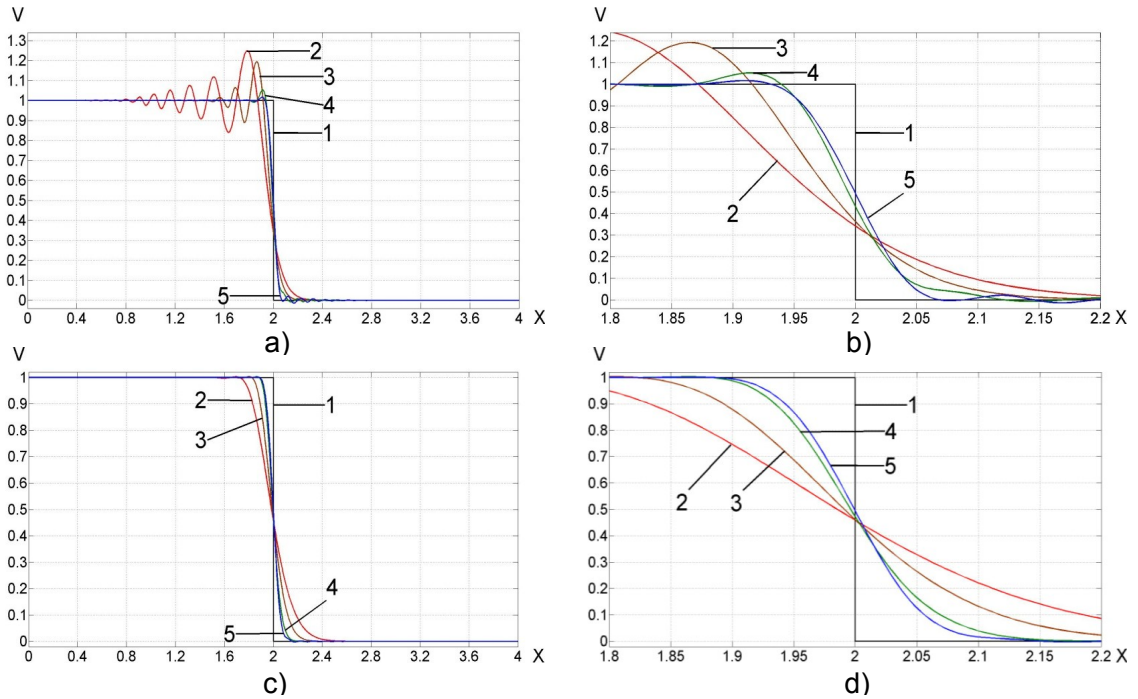


Figure 5.17: The velocity distribution along the bar at the observation time $T = 2$ after (a, b) basic computations (the consistent mass matrix and small time increments) and after (c, d) post-processing. A uniform mesh with the isogeometric 3rd-order elements and 101 dof is used. Curves 2, 3, 4 and 5 correspond to the following time increments in basic computations: $d\bar{t}$, $0.5d\bar{t}$, $0.2d\bar{t}$ and $0.1d\bar{t}$, respectively ($d\bar{t}=0.04$). b) and d) show the zoomed graphs a) and c) in the range $1.8 < x < 2.2$.

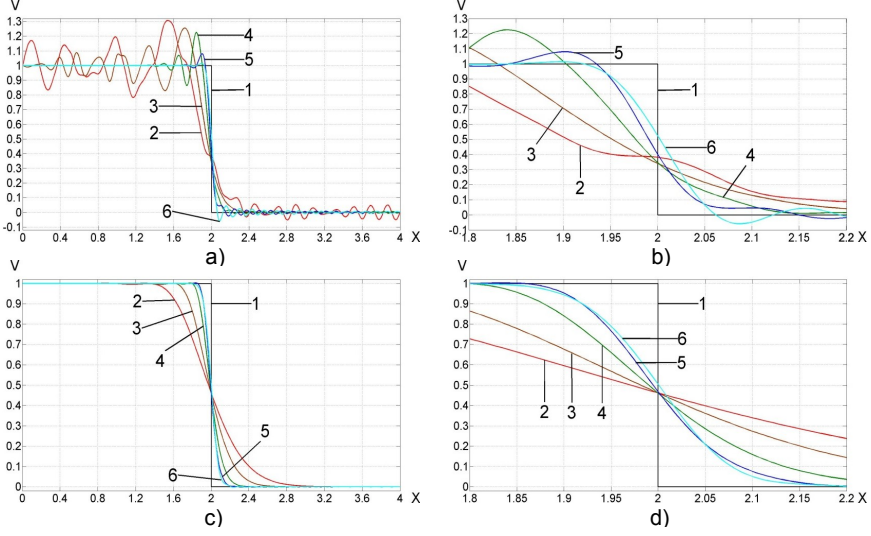


Figure 5.18: The velocity distribution along the bar at the observation time $T = 18$ after (a, b) basic computations (the consistent mass matrix and small time increments) and after (c, d) post-processing. A uniform mesh with the isogeometric 3rd-order elements and 101 dof are used. Curves 2, 3, 4, 5 and 6 correspond to the following time increments in basic computations: $d\bar{t}$, $0.5d\bar{t}$, $0.2d\bar{t}$, $0.1d\bar{t}$ and $0.01d\bar{t}$, respectively ($d\bar{t}=0.04$). b) and d) show the zoomed graphs a) and c) in the range $1.8 < x < 2.2$.

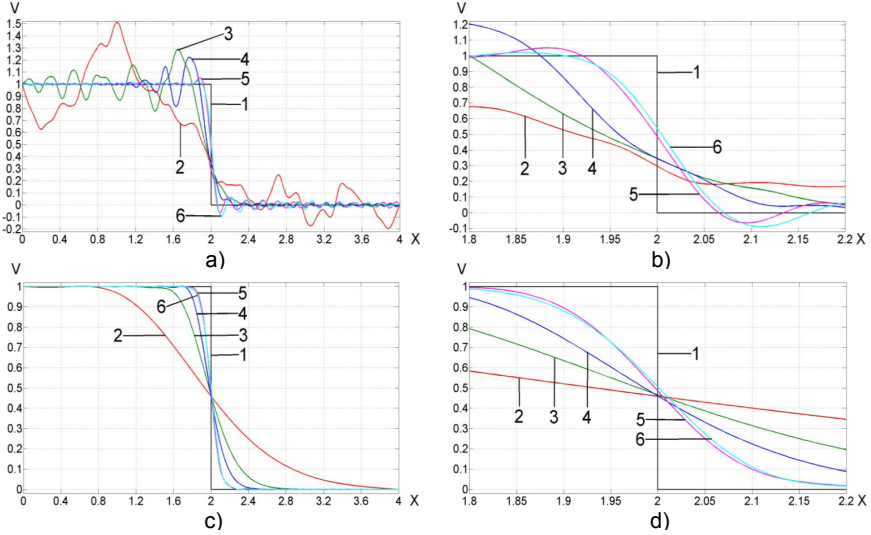


Figure 5.19: The velocity distribution along the bar at the observation time $T = 194$ after (a, b) basic computations (the consistent mass matrix and small time increments) and after (c, d) post-processing. A uniform mesh with the isogeometric 3rd-order elements and 101 dof are used. Curves 2, 3, 4, 5 and 6 correspond to the following time increments in basic computations: $d\bar{t}$, $0.2d\bar{t}$, $0.1d\bar{t}$, $0.03d\bar{t}$ and $0.01d\bar{t}$, respectively ($d\bar{t}=0.04$). b) and d) show the zoomed graphs a) and c) in the range $1.8 < x < 2.2$.

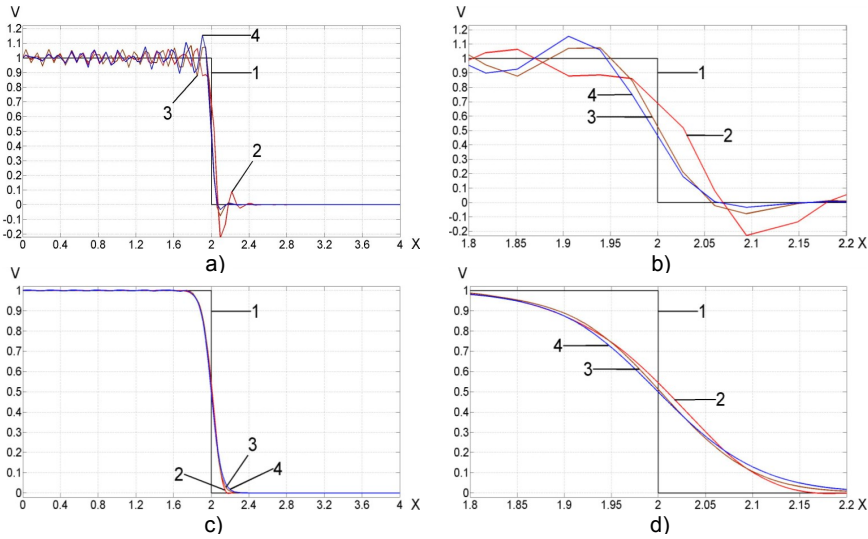


Figure 5.20: The velocity distribution along the bar at the observation time $T = 2$ after (a, b) basic computations (the lumped mass matrix and small time increments) and after (c, d) post-processing. A uniform mesh with the spectral 3rd-order elements and 100 dof is used. Curves 2, 3 and 4 correspond to the following time increments in basic computations: $0.95dt^{st}$, $0.5dt^{st}$ and $0.1dt^{st}$, respectively ($dt^{st}=0.02817$). b) and d) show the zoomed graphs a) and c) in the range $1.8 < x < 2.2$.

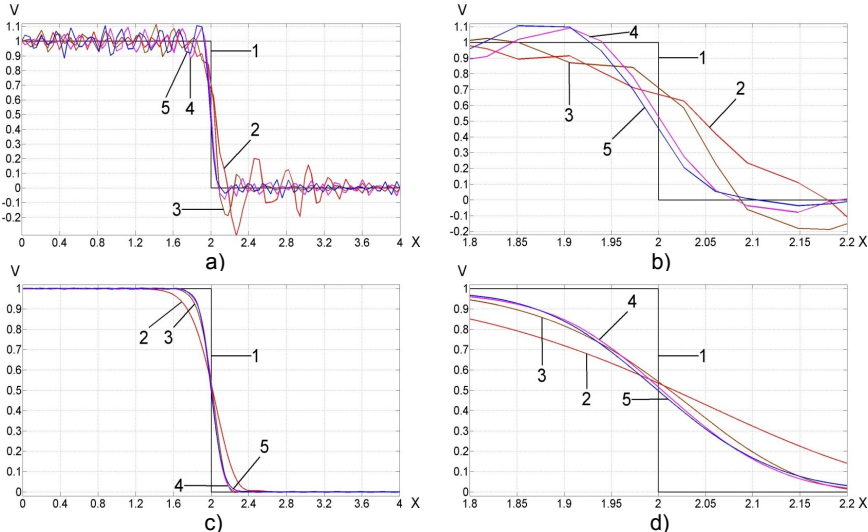


Figure 5.21: The velocity distribution along the bar at the observation time $T = 18$ after (a, b) basic computations (the lumped mass matrix and small time increments) and after (c, d) post-processing. A uniform mesh with the spectral 3rd-order elements and 100 dof is used. Curves 2, 3, 4 and 5 correspond to the following time increments in basic computations: $0.95dt^{st}$, $0.5dt^{st}$, $0.3dt^{st}$ and $0.1dt^{st}$, respectively ($dt^{st}=0.02817$). b) and d) show the zoomed graphs a) and c) in the range $1.8 < x < 2.2$.

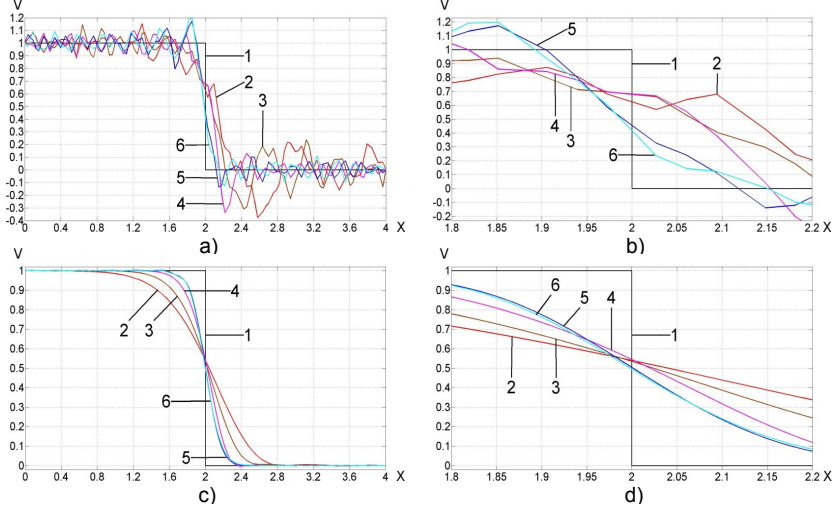


Figure 5.22: The velocity distribution along the bar at the observation time $T = 194$ after (a, b) basic computations (the lumped mass matrix and small time increments) and after (c, d) post-processing. A uniform mesh with the spectral 3rd-order elements and 100 dof is used. Curves 2, 3, 4, 5 and 6 correspond to the following time increments in basic computations: $0.95dt^{st}$, $0.5dt^{st}$, $0.3dt^{st}$, $0.1dt^{st}$ and $0.01dt^{st}$, respectively ($dt^{st}=0.02817$). b) and d) show the zoomed graphs a) and c) in the range $1.8 < x < 2.2$.

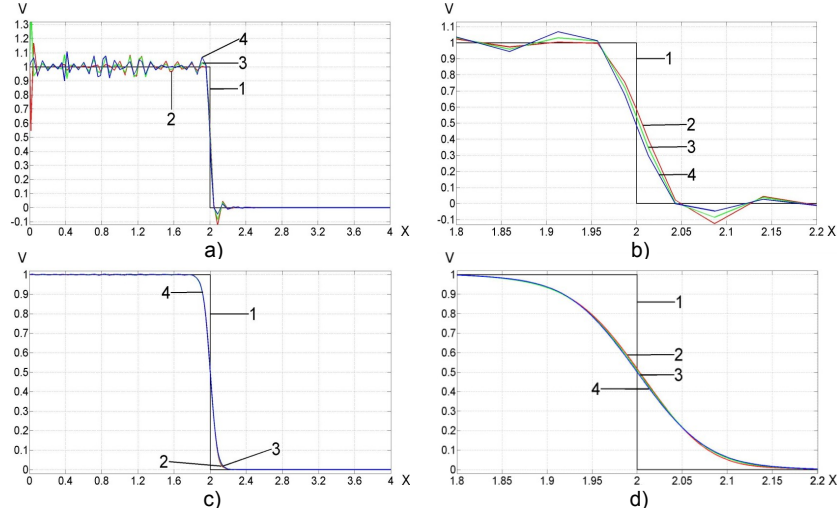


Figure 5.23: The velocity distribution along the bar at the observation time $T = 2$ after (a, b) basic computations (the lumped mass matrix and small time increments) and after (c, d) post-processing. A uniform mesh with the spectral 10th-order elements and 100 dof is used. Curves 2, 3 and 4 correspond to the following time increments in basic computations: $0.95dt^{st}$, $0.7dt^{st}$ and $0.1dt^{st}$, respectively ($dt^{st}=0.0113$). b) show the zoomed graphs a) in the range $1.8 < x < 2.2$. d) show the zoomed graphs c) in the range $1.8 < x < 2.2$.

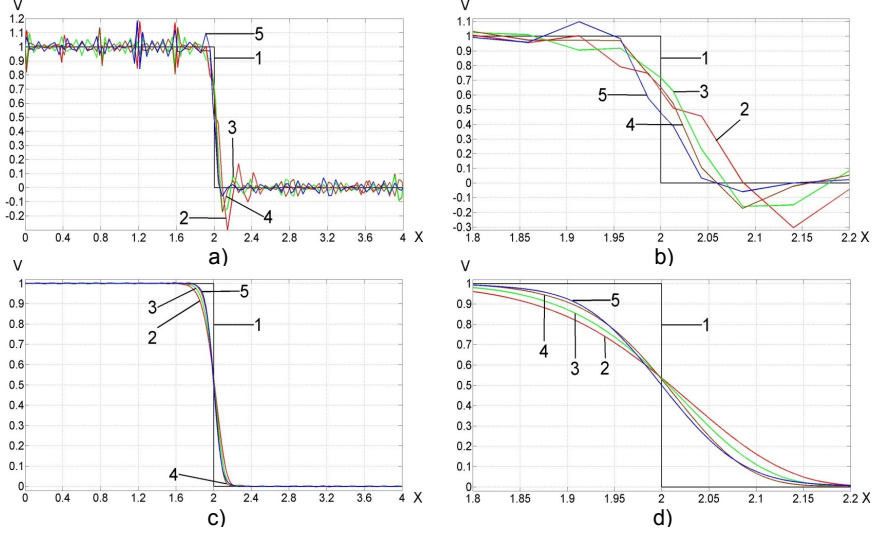


Figure 5.24: The velocity distribution along the bar at the observation time $T = 18$ after (a, b) basic computations (the lumped mass matrix and small time increments) and after (c, d) post-processing. A uniform mesh with the spectral 10th-order elements and 101 dof is used. Curves 2, 3, 4 and 5 correspond to the following time increments in basic computations: $0.95dt^{st}$, $0.7dt^{st}$, $0.5dt^{st}$ and $0.1dt^{st}$, respectively ($dt^{st}=0.0113$). b) and d) show the zoomed graphs a) and c) in the range $1.8 < x < 2.2$.

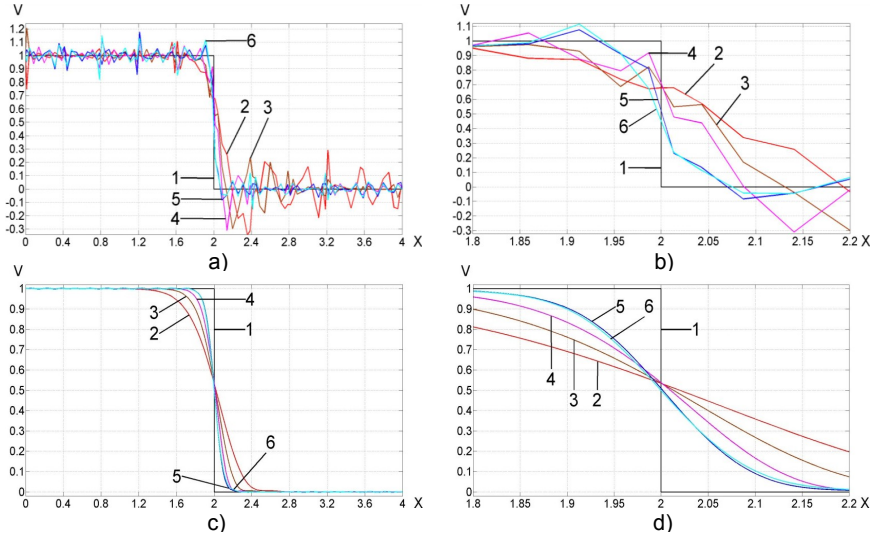


Figure 5.25: The velocity distribution along the bar at the observation time $T = 194$ after (a, b) basic computations (the lumped mass matrix and small time increments) and after (c, d) post-processing. A uniform mesh with the spectral 10th-order elements and 101 dof is used. Curves 2, 3, 4, 5 and 6 correspond to the following time increments in basic computations: $0.95dt^{st}$, $0.5dt^{st}$, $0.3dt^{st}$, $0.1dt^{st}$, and $0.01dt^{st}$, respectively ($dt^{st}=0.0113$). b) and d) show the zoomed graphs a) and c) in the range $1.8 < x < 2.2$.

Chapter VI

CONCLUSIONS

In this study we extended finite element techniques with RD based on the explicit time-integration methods for elastodynamics and acoustic wave propagation problems. For these techniques, we considered the modified integration rule approach for the mass and stiffness matrices and the averaged mass matrix approach . The analytical study of numerical dispersion for the new techniques was carried out in 1-D, 2-D, and 3-D cases for elastodynamics and 2-D case acoustic wave propagation problems. We note that the 1-D case of elastodynamics problem coincides with the 1-D case of acoustic wave propagation problem.

As the results of the effect of time increments on the accuracy of the numerical dispersion, linear elements with RD based on the explicit time-integration methods require the time increment to be closer to the stability limit for the most accurate numerical results for the 1-D case. For the 2-D and 3-D cases in elastodynamics problems, in contrast to the standard approach with the explicit time-integration methods, the linear elements with RD yield more accurate results at very small time increments (smaller than the stability limit Δt^{st}). Unlike the multi-dimensional elastodynamics problems, in contrast to the standard approach with the explicit time-integration methods, the time increments, which are close to the stability limit, are required for the most accurate numerical solutions for acoustic wave propagation problems. Moreover, the numerical examples show that the difference between the modified integration rule and the averaged mass matrix approaches is small and can be neglected.

Furthermore, the new finite element techniques with RD significantly increase the accuracy of numerical solutions for elastodynamics and acoustic wave propagation problems, but they do not remove all spurious high-frequency oscillations. We use the two-stage time-integration technique with the filtering stage to suppress the spurious oscillations. The numerical examples in Section IV show that compared to standard

linear elements at the same accuracy, the linear elements with RD based on explicit time-integration methods significantly reduce the number of dof by factors of $2 - 3$ or more, $4 - 9$ or more, and $8 - 27$ or more in the 1-D, 2-D, and 3-D cases for elastodynamics and acoustic wave propagation problems (see Sections 4.1, 4.2, 4.3, and 4.4). Furthermore, explicit time-integration methods yield an additional reduction in the computation time compared with implicit time-integration methods.

Next, we compared the accuracy of high-order, standard finite elements, isogeometric elements, spectral elements, and linear elements with RD based on the explicit and implicit time-integration methods. In order to obtain accurate results of different space-discretization methods, the two-stage time-integration technique was used to quantify and remove spurious oscillations. The amount of numerical dissipation at the filtering stage can be used as a quantitative measure to compare the accuracy of numerical solutions of these methods. One way to compare the accuracy is based on the evaluation of the numerical dispersion error. However, this error is related to a selected mode of the elastodynamics system of equations and does not prescribe the combined effect of all modes on the accuracy. Moreover, the dispersion error does not estimate the effect of the observation time and time increments on the accuracy of numerical results. Therefore, for the comparison of the accuracy of different methods, we solved the 1-D impact problem in which all modes are excited that has very simple analytical solutions at short and long observation times. Because the computational costs of different space-discretization methods at the same number of dof are different, it is necessary to compare the efficiency of these methods by estimating the computational costs at the same accuracy. This study can be summarized as follows

- At the same dof, the increase in the order of the elements improved the accuracy.
- Despite the same analytical solutions at the selected short and long observation times, the numerical results after the filtering stage are more accurate for short observation times than those for long observation times. Because the error in time is very small in these calculations and can be neglected, the difference in

the numerical results at different observation times is only due to the space-discretization error.

- Except for the known case of the linear elements with the lumped mass matrix, all other space-discretization techniques considered in this study require small time-increments for time integration at the stage of basic computations. Moreover, the time increments should be decreased with the increase in observation time. Even in cases of explicit time-integration methods, the time increments close to the stability limit may yield accurate results at a small observation time, the time increments should be significantly decreased with the increase in the observation time. For example, for the 2nd-order time-integration methods, the size of the time increments should be inversely proportional to the square root of the observation time (as predicted by the exact time error estimator developed in the paper [48]). Similar to implicit time-integration methods, comparably small time increments should be used with explicit time-integration methods for the 1-D impact problem. According to our results, the typical statement in finite element textbooks, which states that for explicit methods, a time increment should be close to the stability limit (e.g., see [9, 20]) is not true, because the size of a time increment should depend on the observation time and should be much smaller than the stability limit at long observation times.
- The comparison of the space-discretization techniques based on the non-diagonal mass matrices (used with implicit time-integration methods) show that at the same number of dof, the isogeometric elements yield more accurate results compared with the standard high-order finite elements and the linear elements with RD. However, when we compare the computational costs at the same accuracy, the numerical results show the linear elements with RD are more computationally efficient than other space-discretization techniques. We should also mention that compared with the isogeometric 3rd-order elements, the computational efficiency of the linear elements with RD decreases with the increase in

the observation time.

- The comparison of the space-discretization techniques based on the diagonal mass matrices (used with explicit time-integration methods) show that at the same number of dof, the spectral high-order elements yield more accurate results compared with standard linear and quadratic finite elements, and linear elements with RD. However, when we compare the computational costs at the same accuracy, the numerical results show that linear elements with RD are more computationally efficient than spectral high-order elements. We should also mention that compared with spectral 10th-order elements, the computational efficiency of linear elements with RD decreases with the increase in the observation time.
- It is interesting to note that the size of time increments at the filtering stage of the two-stage time-integration technique (this size is calculated according to Eqs. (3.1) - (3.3) from Chapter III) defines the range of actual frequencies used in numerical solutions and can serve as a quantitative measure for the comparison and the prediction of the accuracy and the computational efficiency of different space-discretization techniques. This is true not only for the 1-D problem (see Section V) but also for the multidimensional problems (e.g., see Section IV and [43, 47]).

The comparison of accuracy of different space-discretization techniques for 1-D impact problems for which all frequencies are excited is valid for any transient elastodynamics or acoustic problem for which only a part of frequencies is excited. For example, in the paper [47] we showed that the two-stage time-integration approach can be equally applied to wave propagation problems under impact loading as well as low- and high-frequency loading (the same range of spurious high-frequencies should be filtered independent of applied loading).

We should also mention that the formulations with RD and the explicit time-integration methods can be directly and effectively used (almost without modifica-

tions) on parallel computers because the numerical algorithm includes the matrix and vector multiplications and can be performed at the element level without the solution of a system of algebraic equations. For transient linear elastodynamics and acoustic wave propagation problems, the new two-stage time integration technique is very general and can be applied to any loading as well as for any space-discretization technique and any explicit or implicit time-integration method. Furthermore, the finite element technique with RD can be easily implemented into existing finite element codes and lead to a significant reduction in computation time at the same accuracy compared with standard finite element formulations.

Bibliography

- [1] R. Abedi, S. H. Chung, J. Erickson, Y. Fan, M. Garland, D. Guoy, R. Haber, J. M. Sullivan, S. Thite, and Y. Zhou. *Spacetime meshing with adaptive refinement and coarsening*. 2004.
- [2] J. H Argyris and D. W Scharpf. Finite elements in time and space. *Nucl. Engrg. Des.*, (10):456–464, 1969.
- [3] C. D. Baily. The method of ritz applied to the equations of hamilton. *Comput. Methods Appl. Mech. Engrg.*, (7):235–247, 1976.
- [4] C. I. Bajer. Triangular and tetrahedral space-time finite elements in vibration analysis. *International Journal for Numerical Methods in Engineering*, 23(11):2031–2048, 1986.
- [5] C. I. Bajer. Notes on the stability of non-rectangular space-time finite elements. *International Journal for Numerical Methods in Engineering*, 24(9):1721–1739, 1987.
- [6] C. I. Bajer. Adaptive mesh in dynamic problems by the space-time approach. *Computers and Structures*, 33(2):319–325, 1989.
- [7] C. I. Bajer, R. Bogacz, and C. G. Bonthoux. Adaptive space-time elements in the dynamic elastic-viscoplastic problem. *Computers and Structures*, 39, 1991.
- [8] C. I. Bajer and C. G. Bonthoux. State-of-the-art in true space-time finite element method. *Shock and Vibration Digest*, 20, 1998.
- [9] K. J. Bathe. *Finite element procedures*. Prentice-Hall Inc., Upper Saddle River, New Jersey, 1996.
- [10] D. J. Benson, Y. Bazilevs, E. De Luycker, M.-C. Hsu, M. Scott, T. J. R. Hughes, and T. Belytschko. A generalized finite element formulation for arbitrary basis functions: From isogeometric analysis to xfem. *International Journal for Numerical Methods in Engineering*, 83(6):765–785, 2010.
- [11] D.J. Benson, Y. Bazilevs, M.-C. Hsu, and T.J.R. Hughes. A large deformation, rotation-free, isogeometric shell. *Computer Methods in Applied Mechanics and Engineering*, 200(1316):1367 – 1378, 2011.
- [12] M. Borri, G. L. Ghiringhelli, M. Lanz, P. Mantegazza, and T. Merlini. Dynamic response of mechanical systems by a weak hamiltonian formulation. *Comput. and Structures*, (20):495–508, 1985.

- [13] M. Cannarozzi and M. Mancuso. Formulation and analysis of variational methods for time integration of linear elastodynamics. *Computer Methods in Applied Mechanics and Engineering*, 127(1-4):241–257, 1995.
- [14] F. Casadei, E. Gabellini, G. Fotia, F. Maggio, and A. Quarteroni. A mortar spectral/finite element method for complex 2d and 3d elastodynamic problems. *Computer Methods in Applied Mechanics and Engineering*, 191(45):5119–5148, 2002.
- [15] A. Cella, M. Lucchesi, and G. Pasquinelli. Space-time elements for the shock wave propagation problem. *International Journal for Numerical Methods in Engineering*, 15(10):1475–1488, 1980.
- [16] H. P. Cherukuri. Dispersion analysis of numerical approximations to plane wave motions in an isotropic elastic solid. *Computational Mechanics*, 25(4):317–328, 2000.
- [17] C. C. Chien and T. Y. Wu. Improved predictor/multi-corrector algorithm for a time-discontinuous galerkin finite element method in structural dynamics. *Computational Mechanics*, 25(5):430–437, 2000.
- [18] C. C. Chien, C. S. Yang, and J. H. Tang. Three-dimensional transient elastodynamic analysis by a space and time-discontinuous galerkin finite element method. *Finite Elements in Analysis and Design*, 39(7):561–580, 2003.
- [19] S.S. Cho, H. Huh, and K.C. Park. A time-discontinuous implicit variational integrator for stress wave propagation analysis in solids. *Computer Methods in Applied Mechanics and Engineering*, 200(5-8):649 – 664, 2011.
- [20] Robert D. Cook, David S. Malkus, Michael E. Plesha, and Robert J. Witt. *Concepts and Applications of Finite Element Analysis*. Wiley, 2001.
- [21] J.A. Cottrell, A. Reali, Y. Bazilevs, and T.J.R. Hughes. Isogeometric analysis of structural vibrations. *Computer Methods in Applied Mechanics and Engineering*, 195(41-43):5257 – 5296, 2006.
- [22] Kent T. Danielson, Su Hao, Wing Kam Liu, R. Aziz Uras, and Shoafan Li. Parallel computation of meshless methods for explicit dynamic analysis. *International Journal for Numerical Methods in Engineering*, 47(7):1323 – 1341, 2000.
- [23] W. Dauksher and A. F. Emery. Solution of elastostatic and elastodynamic problems with chebyshev spectral finite elements. *Computer Methods in Applied Mechanics and Engineering*, 188(1):217–233, 2000.
- [24] Eduardo Gomes Dutra Do Carmo, Cid Da Silva Garcia Monteiro, and Webe Joao Mansur. A finite element method based on capturing operator applied to wave

- propagation modeling. *Computer Methods in Applied Mechanics and Engineering*, 201-204:127 – 138, 2012.
- [25] R. S. Falk and G. R. Richter. Explicit finite element methods for symmetric hyperbolic equations. *SIAM Journal on Numerical Analysis*, 36(3):935–952, 1999.
 - [26] R. S. Falk and G. R. Richter. *Discontinuous Galerkin methods : theory, computation and applications*, volume 15. Springer, Berlin, New York, 2000.
 - [27] J. E. Flaherty, R. M. Loy, M. S. Shephard, and J. D. Teresco. *Discontinuous Galerkin Methods Theory, Computation and Applications, Lecture Notes in Computational Science and Engineering*, volume 11. Springer, Berlin, 2000.
 - [28] T. C. Fung. Construction of higher-order accurate time-step integration algorithms by equal-order polynomial projection. *Journal of Vibration and Control*, 11(1):19–49, 2005.
 - [29] D. Gabriel, J. Plesek, R. Kolman, , and F. Vales. Dispersion of elastic waves in the contact-impact problem of a long cylinder. *Journal of Computational and Applied Mathematics*, 234:1930–1936, 2010.
 - [30] M. N. Guddati and B. Yue. Modified integration rules for reducing dispersion error in finite element method. *Computer Methods in Applied Mechanics and Engineering*, 193:275–287, 2004.
 - [31] M. E. Gurtin. Variational principles for linear initial value problems. *Quart. Appl. Math.*, (22):252–256, 1964.
 - [32] Z. C. He, A. G. Cheng, G. Y. Zhang, Z. H. Zhong, and G. R. Liu. Dispersion error reduction for acoustic problems using the edge-based smoothed finite element method (es-fem). *International Journal for Numerical Methods in Engineering*, 86(11):1322–1338, 2011.
 - [33] H. M. Hilber and T. J. R. Hughes. Collocation, dissipation and 'overshoot' for time integration schemes in structural dynamics. *Earthquake Engrg. Struct. Dyn.*, (6):99–118, 1978.
 - [34] H. M. Hilber, T. J. R Hughes, and R. L Taylor. Improved numerical dissipation for time integration algorithms in structural dynamics. *Earthquake Engrg. Struct. Dyn.*, (5):283–292, 1977.
 - [35] J. C. Houboldt. A recurrence matrix solution for the dynamic response of elastic aircraft. *Computer Methods in Applied Mechanics and Engineering*, (17):540–550, 1950.
 - [36] T. J. R Hughes. *The Finite Element Method: Linear Static and Dynamic Finite Element Analysis*. Prentice- Hall, Englewood Cliffs, NJ, 1987.

- [37] T. J. R. Hughes and G. M. Hulbert. Space-time finite element methods for elastodynamics: Formulations and error estimates. *Computer Methods in Applied Mechanics and Engineering*, 66(3):339–363, 1988.
- [38] T.J.R. Hughes, A. Reali, and G. Sangalli. Duality and unified analysis of discrete approximations in structural dynamics and wave propagation: Comparison of p-method finite elements with k-method nurbs. *Computer Methods in Applied Mechanics and Engineering*, 197(49-50):4104 – 4124, 2008.
- [39] G. M. Hulbert. Discontinuity-capturing operators for elastodynamics. *Computer Methods in Applied Mechanics and Engineering*, 96(3):409–426, 1992.
- [40] G. M. Hulbert. Time finite element methods for structural dynamics. *International Journal for Numerical Methods in Engineering*, 33(2):307–331, 1992.
- [41] G. M. Hulbert and T. J. R. Hughes. Space-time finite element methods for second-order hyperbolic equations. *Computer Methods in Applied Mechanics and Engineering*, 84(3):327–348, 1990.
- [42] A. Idesman, M. Schmidt, and J. R. Foley. Accurate 3-d finite element simulation of elastic wave propagation with the combination of explicit and implicit time-integration methods. *Wave Motion*, 48(49-50):625–633, 2011.
- [43] A. Idesman, M. Schmidt, and J. R. Foley. Accurate finite element modeling of linear elastodynamics problems with the reduced dispersion error. *Computational Mechanics*, 47:555–572, 2011.
- [44] A. Idesman, K. Subramanian, M. Schmidt, J. R. Foley, Y. Tu, and R. L. Sierakowski. Finite element simulation of wave propagation in an axisymmetric bar. *Journal of Sound and Vibration*, 329:2851–2872, 2010.
- [45] A. V. Idesman. A new high-order accurate continuous galerkin method for linear elastodynamics problems. *Computational Mechanics*, 40(193):261–279, 2007.
- [46] A. V. Idesman. Solution of linear elastodynamics problems with space-time finite elements on structured and unstructured meshes. *Computer Methods in Applied Mechanics and Engineering*, 196:1787–1815, 2007.
- [47] A. V. Idesman. Accurate time integration of linear elastodynamics problems. *Computer Modeling in Engineering & Sciences*, 71(2):111–148, 2011.
- [48] A. V. Idesman. A new exact, closed-form a-priori global error estimator for second- and higher-order time integration methods for linear elastodynamics. *International Journal for Numerical Methods in Engineering*, 88(49-50):1066–1084, 2011.

- [49] A. V. Idesman and D. Pham. Finite element modeling of linear elastodynamics problems with explicit time-integration methods and linear elements with the reduced dispersion error. *Computer Methods in Applied Mechanics and Engineering*, 1–33, 2013 (submitted).
- [50] A. V. Idesman, H. Samajder, E. Aulisa, and P. Seshaiyer. Benchmark problems for wave propagation in elastic materials. *Computational Mechanics*, 43(6):797–814, 2009.
- [51] K. Jansen and L. Porkolab. Linear-time approximation schemes for scheduling malleable parallel tasks. *Algorithmica*, 32(3):507–520, 2002.
- [52] K. Jansen and L. Porkolab. General multiprocessor task scheduling: approximate solutions in linear time. *SIAM Journal on Computing*, 35(3):519–530, 2005.
- [53] R. Kanapady and K. K. Tamma. A mathematical framework towardsa unified set of state-phase time operators for computationaldynamics. *Computer Modeling in Engineering and Sciences*, 4(1):103–118, 2003.
- [54] R. Kanapady and K. K. Tamma. On a novel design of a new unified variational framework ofdiscontinuous/continuous time operators of high order and equivalence. *Finite Elements in Analysis and Design*, 39(8):727–749, 2003.
- [55] D. Komatitsch, C. Barnes, and J. Tromp. Simulation of anisotropic wave propagation based upon a spectral element method. *Geophysics*, 65(4):1251–1260, 2000.
- [56] Dimitri Komatitsch and Jean-Pierre Vilotte. Spectral element method: an efficient tool to simulate the seismic response of 2d and 3d geological structures. *Bulletin of the Seismological Society of America*, 88(2):368 – 392, 1998.
- [57] Dimitri Komatitsch, Jean-Pierre Vilotte, Rossana Vai, JOSE M. Castillo-Covarrubias, and Francisco J. Sanchez-Sesma. The spectral element method for elastic wave equations - application to 2-d and 3-d seismic problems. *International Journal for Numerical Methods in Engineering*, 45(9):1139 – 1164, 1999.
- [58] S. Krenk. Dispersion-corrected explicit integration of the wave equation. *Computer Methods in Applied Mechanics and Engineering*, 191:975–987, 2001.
- [59] P. Kunthong and L. L. Thompson. An efficient solver for the high-order accurate time-discontinuous galerkin (tdg) method for second-order hyperbolic systems. *Finite Elements in Analysis and Design*, 41(7-8):729–762, 2005.
- [60] A. Lew, J. E. Marsden, M. Ortiz, and M. West. Asynchronous variational integrators. *Archive for Rational Mechanics and Analysis*, 167(2):85–146, 2003.

- [61] H. Li. *Meshless Methods and Their Numerical Properties*. CRC Press, 2013.
- [62] Shaofan Li and Wing Kam Liu. Moving least-square reproducing kernel method part ii: Fourier analysis. *Computer Methods in Applied Mechanics and Engineering*, 139(14):159 – 193, 1996.
- [63] Shaofan Li and Wing Kam Liu. Reproducing kernel hierarchical partition of unity, part ii - applications. *International Journal for Numerical Methods in Engineering*, 45(3):289 – 317, 1999.
- [64] X. D. Li and N. E. Wiberg. Structural dynamic analysis by a time-discontinuous galerkin finite element method. *International Journal for Numerical Methods in Engineering*, 39(12):2131–2152, 1996.
- [65] X. D. Li and N. E. Wiberg. Implementation and adaptivity of a space-time finite element method for structural dynamics. *Computer Methods in Applied Mechanics and Engineering*, 156:211–229, 1998.
- [66] G. R. Liu. *Meshfree Methods: Moving Beyond the Finite Element Method*. CRC Press, New York, 2009.
- [67] G.R. Liu, K.Y. Dai, and T.T. Nguyen. A smoothed finite element method for mechanics problems. *Computational Mechanics*, 39(6):859 – 877, 2007.
- [68] G.R. Liu, T.T. Nguyen, K.Y. Dai, and K.Y. Lam. Theoretical aspects of the smoothed finite element method (sfem). *International Journal for Numerical Methods in Engineering*, 71(8):902 – 930, 2007.
- [69] Wing Kam Liu, Yijung Chen, R.Aziz Uras, and Chin Tang Chang. Generalized multiple scale reproducing kernel particle methods. *Computer Methods in Applied Mechanics and Engineering*, 139(14):91 – 157, 1996.
- [70] L. Maheo, V. Grolleau, and G. Rio. Numerical damping of spurious oscillations: A comparison between the bulk viscosity method and the explicit dissipative tchamwa-wielgosz scheme. *Computational Mechanics*, 51(1):109 – 128, 2013.
- [71] M. Mancuso and F. Ubertini. An efficient integration procedure for linear dynamics based on a time discontinuous galerkin formulation. *Computational Mechanics*, 32(3):154–168, 2003.
- [72] M. Mancuso and F. Ubertini. A methodology for the generation of low-cost higher-order methods for linear dynamics. *International Journal for Numerical Methods in Engineering*, 56(13):1883–1912, 2003.
- [73] K. J. Marfurt. Accuracy of finite difference and finite element modeling of the scalar and elastic wave equation. *Geophysics*, 49:533–549, 1984.

- [74] R. Mullen and T. Belytschko. Dispersion analysis of finite element semidiscretizations of the two-dimensional wave equation. *International Journal for Numerical Methods in Engineering*, 18, 1982.
- [75] M. O. Neal and T. Belytschko. Explicit-explicit subcycling with non-integer time step ratios for structural dynamic systems. *Computers and Structures*, 31(6):871–880, 1989.
- [76] N. M. Newmark. A method of computation for structural dynamics. *J. Eng. Mech. Div. ASCE.*, (8):67–94, 1959.
- [77] W. Nowacki. *A general theory of finite elements II. Applications*. Number 1. 1969.
- [78] J. T Oden. A general theory of finite elements ii. applications. *Internat. J. Numer. Methods in Engrg.*, (1):247–259, 1969.
- [79] K. C. Park. *Finite Element Analysis of Transient Nonlinear Behavior*. AMD 14, ASME, New York, 1975.
- [80] K.C. Park, S.J. Lim, and H. Huh. A method for computation of discontinuous wave propagation in heterogeneous solids: Basic algorithm description and application to one-dimensional problems. *International Journal for Numerical Methods in Engineering*, 91(6):622 – 643, 2012.
- [81] C. Pozrikidis. *Introduction to Finite and Spectral Element Methods Using MATLAB*. CRC Press, 2005.
- [82] G. Seriani and S. P. Oliveira. Optimal blended spectral-element operators for acoustic wave modeling. *Geophysics*, 72(5):95–106, 2007.
- [83] G. Seriani and S. P. Oliveira. Dispersion analysis of spectral element methods for elastic wave propagation. *Wave Motion*, 45(6):729–744, 2008.
- [84] P. Smolinski, S. Sleith, and T. Belytschko. Stability of an explicit multi-time step integration algorithm for linear structural dynamics equations. *Computational Mechanics*, 18(3):236–244, 1996.
- [85] P. Smolinski and Y.-S. Wu. Implicit multi-time step integration method for structural dynamics problems. *Computational Mechanics*, 22(4):337–343, 1998.
- [86] J.D. Teresco, M.W. Beall, J.E. Flaherty, and M.S. Shephard. Hierarchical partition model for adaptive finite element computation. *Computer Methods in Applied Mechanics and Engineering*, 184(2-4):269–285, 2000.
- [87] L. L. Thompson and D. He. Adaptive space-time finite element methods for the wave equation on unbounded domains. *Computer Methods in Applied Mechanics and Engineering*, 194(18-20):1947–2000, 2005.

- [88] Dalei Wang, Radek Tezaur, Jari Toivanen, and Charbel Farhat. Overview of the discontinuous enrichment method, the ultra-weak variational formulation, and the partition of unity method for acoustic scattering in the medium frequency regime and performance comparisons. *International Journal for Numerical Methods in Engineering*, 89(4):403–417, 2012.
- [89] N. E. Wiberg and X. D. Li. Adaptive finite element procedures for linear and non-linear dynamics. *International Journal for Numerical Methods in Engineering*, 46, 1999.
- [90] E. L Wilson, I. Farhoomand, and K. J. Bathe. Nonlinear dynamic analysis of complex structures. *Earthquake Eng. Struct. Dyn.*, (1):242–252, 1973.
- [91] L. C. Wrobel and M. H. Aliabadi. *The Boundary Element Method*. Wiley, 2002.
- [92] Y.S. Wu and P. Smolinski. Implicit multi-time step integration method for structural dynamics problems. *Computer Methods in Applied Mechanics and Engineering*, 187(3):641–660, 2000.
- [93] Y. Xing and C. Shu. High order well-balanced finite volume weno schemes and discontinuous galerkin methods for a class of hyperbolic systems with source terms. *Journal of Computational Physics*, 214:567–598, 2006.
- [94] L. Yin, N. S. Acharya, R. B. Haber, and D. A. Tortorelli. *A space-time discontinuous Galerkin method for elastodynamic analysis*. Springer, 2000.
- [95] B. Yue and M. N. Gudati. Dispersion-reducing finite elements for transient acoustics. *Journal of the Acoustical Society of America*, 118(4):2132–2141, 2005.
- [96] G. M. Zhang and R. C. Batra. Wave propagation in functionally graded materials by modified smoothed particle hydrodynamics (msph) method. *Journal of Computational Physics*, 222(0):374 – 390, 2007.
- [97] O. C. Zienkiewicz and R. L. Taylor. *The Finite Element Method*. Butterworth-Heinemann, Oxford, UK, 2000.
- [98] O. C. Zienkiewicz, W. L. Wood, N. W. Hines, and R. L. Taylor. Unified set of single step algorithms - part i: General formulation and applications. *International Journal for Numerical Methods in Engineering*, 20, 1984.
- [99] F. I. Zyserman and P. M. Gauzellino. Dispersion analysis of a nonconforming finite element method for the three-dimensional scalar and elastic wave equations. *Finite Elements in Analysis and Design*, 41(13):1309–1326, 2005.